INVESTIGATION ON CERTAIN ISSUES RELATED TO DEVELOPMENT OF NEXT-GENERATION BROADBAND WIRELESS NETWORKS

Arijit Bhattacharjee

INVESTIGATION ON CERTAIN ISSUES RELATED TO DEVELOPMENT OF NEXT-GENERATION BROADBAND WIRELESS NETWORKS

A

Thesis Submitted

in Partial Fulfilment of the Requirements

for the Degree of

DOCTOR OF PHILOSOPHY

By

Arijit Bhattacharjee

DEPARTMENT OF ELECTRONICS AND ELECTRICAL ENGINEERING

INDIAN INSTITUTE OF TECHNOLOGY GUWAHATI

GUWAHATI - 781 039, ASSAM, INDIA

August, 2021

Declaration

I hereby declare that the thesis entitled "**INVESTIGATION ON CERTAIN ISSUES RELATED TO DEVELOPMENT OF NEXT-GENERATION BROADBAND WIRELESS NETWORKS**", submitted in the *Department of Electronics and Electrical Engineering, Indian Institute of Technology Guwahati, Assam, India*, for the award of the degree of **Doctor of Philosophy**, has been carried out by me under the supervision and guidance of Prof. Sanjay Kumar Bose and Prof. Ratnajit Bhattacharjee. The results embodied in this thesis are original and have not been submitted to any other University or Institute for the award of any degree or diploma.

Dated:

Place: Guwahati

Arijit Bhattacharjee
Research Scholar
Dept. of Electronics and Electrical Engineering
Indian Institute of Technology Guwahati
Guwahati - 781039, Assam, India.

Certificate

This is to certify that the thesis entitled "**INVESTIGATION ON CERTAIN ISSUES RELATED TO DEVELOPMENT OF NEXT-GENERATION BROADBAND WIRELESS NETWORKS**", submitted by **Arijit Bhattacharjee** (156102012), a research scholar in the *Department of Electronics and Electrical Engineering, Indian Institute of Technology Guwahati*, for the award of the degree of **Doctor of Philosophy**, is a record of an original research work carried out by him under our supervision and guidance. The thesis has fulfilled all requirements as per the regulations of the institute and in my opinion has reached the standard needed for submission. The results embodied in this thesis have not been submitted to any other University or Institute for the award of any degree or diploma.

Dated:
Guwahati.

Prof. Sanjay Kumar Bose
Professor
Dept. of Electronics and Electrical Engg.
Indian Institute of Technology Guwahati
Guwahati - 781 039, Assam, India.

Dated:
Guwahati.

Prof. Ratnajit Bhattacharjee
Professor
Dept. of Electronics and Electrical Engg.
Indian Institute of Technology Guwahati
Guwahati - 781 039, Assam, India.

To all my family members

Acknowledgements

First and foremost, I feel it as a great privilege in expressing my deepest and most sincere gratitude to my supervisors Prof. Sanjay Kumar Bose & Prof. Ratnajit Bhattacharjee, for their excellent guidance throughout my Ph.D. tenure. Their kindness, dedication and attention to the details has been a source of great inspiration to me. My heartfelt thanks to my supervisors for their unlimited support and patience that they have shown towards me. Their emphasis on clear communication helped me a lot. They have enriched my life in many significant ways. I thank them from the bottom of my heart for always being there with me during all kinds of distress.

I would like to thank my doctoral committee members Dr. A. Rajesh, Dr. T. Venkatesh, and Dr. Kalpana Dhaka for sparing time out of their busy schedule to evaluate my progress and enrich this work with their valuable suggestions and feedback.

I would also like to thank Qualcomm Inc. for supporting my research through the Qualcomm Innovation Fellowship Grant (QIF-2019) and my Qualcomm mentors Mr. Venkatesh and Dr. Abhijit for their support and guidance.

During my Ph.D., I found really wonderful lab-mates and fellow research scholars. I had never expected such sensitive and helping people existing in highly professional research institute like IITs. My sincere thanks to my friends Shivanshu, Ripudaman and Sikandar, for some of the extremely important discussions and feedbacks during the initial days of my Ph.D. I have no words to thank my lab-mates Asim, Niladri, Sumantra, Mohit, Arijit, Prateek, and Aditya and fellow researchers Binod and Rohit. These guys made my stay at IIT Guwahati memorable. I will cherish the time spent with them. I thank them all for their friendship.

I express my deep appreciation to my wife Sanghita and my parents for their unconditional support and understanding for all these moments. This Ph.D. would not have been possible without their help and support.

Lastly, I extend my sincere thanks to all the staff members from EEE office and Academic office for helping me out in all sorts of ways during my stay at IITG.

Arijit Bhattacharjee

Abstract

The day-by-day increasing popularity of mobile phones, wearable devices, and other such personal wireless devices has resulted in a huge surge in user-generated data. This trend has been augmented further by the inclusion of new technologies, services, and applications centered on wireless systems. As a result, the expectations from the mobile networks to cater to the new services and traffic conditions are also rising at an equally concerning rate. To tackle this crisis, researchers from academia and industry are looking for ways to improve the existing network capacities by enhancing the current technologies. The challenge is not just limited to upgrading the existing network capabilities but also to ramp up their link-level capacity and augmenting them in providing reliable last-mile connectivity. For this reason, the need for high-capacity wireless links has become particularly significant owing to the prominence of high data-rate enhanced multimedia broadband (eMBB) applications like HD videos, gaming, and Internet-of-Things (IoT) in the overall share of network usage.

However, supporting these applications using the existing commercial communication spectrum seems unlikely, as these bands are already congested, and there is hardly any scope for capacity improvement. Therefore, the prospect of communication using the millimeter-wave (*mmWave*) bands ranging from 30 GHz to 300 GHz frequencies has been explored thoroughly. Due to their large bandwidths and cheap spectrum costs, these frequencies are considered ideal for supporting the eMBB services and other high data-rate applications.

Unfortunately, the adverse wave-propagation characteristics in these bands and the related medium-access-control (MAC)-layer problems of beam-blockage and poor mobility support render these systems unreliable and untenable for commercial usage. These problems also lead to several incompatibility issues with respect to the existing MAC-layer standards. Since reliable mmWave access networks are also a prerequisite for the successful roll-out of the next generation (5G) networks, this becomes a technological bottleneck.

Hence, in consideration of all these factors, this thesis identifies various issues which lead to unreliable and inefficient operation of mmWave systems and aims to provide robust solutions. To this end, the thesis focuses on three types of challenges: The first limitation concerns the issue of beam blockage that causes unreliable connectivity. For this, the thesis presents various low-cost (low CAPEX, OPEX) solutions based on the MAC layer. These solutions leverage the technique of control delegation to dynamically operate an access point from different vantage points and alleviate the blockage scenario of the network. By using this, two types of delegation approaches have been presented. The first one uses a fixed set of rules to take the delegation decisions, whereas the second approach uses a discrete-time Markov-decision-process (DT-MDP) model to dynamically determine the delegation policy.

In the second area of focus, the thesis discusses the issue of high infrastructure requirements for mmWave systems that operate using the multi-link-connectivity (MLC) architecture. To alleviate this problem, various device-centric dynamic-link-level-redundancy (DC-DLLR) approaches (and their supportive network architecture) are presented to reduce their CAPEX and OPEX requirements.

Finally, in the third area of focus, the issue of blockage-induced anomalous resource allocation is discussed for a class of mmWave networks that operate under the simultaneously-operating-piconet (SOP) configuration (a form of MLC architecture). To address this, the thesis presents a feedback-driven (reactive) approach and a portfolio-theory-based risk-sensitive approach for resource allocation that would enable network operators to allocate resources more efficiently and robustly.

Contents

List of Figures

List of Tables

Glossary

3GPP	3rd Generation Partnership Project
AP	Access Point
ABG	Alpha-Beta-Gamma Model
BSSIDs	Basic Service Set Identifiers
CAPEX	Capital Expenditure
CR	Cognitive Radio
CI	Close-In Free Space Reference Distance Model
CBR	Constant Bit Rate
CDF	Cumulative Distribution Function
CTA	Channel Time Access
DCD	Dynamic Control Delegation
DT-MDP	Discrete Time Markov Decision Process
DLLR	Dynamic Link-Level Redundancy
DC-DLLR	Device Centric - Dynamic Link-Level Redundancy
D2D	Device-to-Device
eMBB	Enhanced Multimedia Broadband
eNB	eNodeB
FCC	Federal Communications Commission
IoT	Internet-of-Things
IBFD	In-Band-Full-Duplex
IE	Information Element
JFI	Jain's Fairness Index
KED	Knife Edge Diffraction Model

LTE	Long-Term Evolution
LTE-A	LTE-Advanced
LoS	Line-of-Sight
M2M	Machine-to-Machine
MAC	Medium Access Control
MHRT	Multi-Hop Relaying Transmission
MIMO	Multiple Input Multiple Output
MLC	Multi-Link-Connectivity
mmWave	Millimeter-wave
NC-DLLR	Network Centric - Dynamic Link-Level Redundancy
NOMA	Non-Orthogonal Multiple Access
NLoS	Non-Line-of-Sight
NYUSIM	New York University mmWave Channel Simulator Tool
OPEX	Operational Expenditure
OSI	Open Systems Interconnection Model
PNC	Piconet Controller
PACTA	Portfolio Allocation based Channel Time Assignment
p-CTA	Pseudo-static Channel Time Access
p/c	Parent-Child Piconet
p/n	Parent-Neighbour Piconet
PLE	Path Loss Exponent
P2P	Point-to-Point
QoS	Quality-of-Service
RAT	Radio Access Technologies
RANs	Radio Access Networks
RMa	Rural-Macrocell
RSS	Received Signal Strength
RX	Receiver Module
SOP	Simultaneously Operating Piconet
SDN	Software-Defined Networking

SF	Superframe
SNR	Signal-to-Noise-Ratio
TX	Transmitter module
TDMA	Time-Division Multiple Access
TU	Transmission Unit
UHF	Ultra High Frequency
URLLC	Ultra-Reliable Low-Latency Communication
UMa	Urban-Macrocell
VIA	Value Iteration Algorithm
V2I	Vehicle-to-Infrastructure
WPAN	Wireless Personal Area Network

List of Symbols

A_s	The set of all actions associated with all the system states $s \in S$
a_{d_i}	A delegation action where the piconet control stays with node $d_i \in \mathcal{D}$
$a_{<src,dst>}$	Association status of a node $< src >$ with respect to PNC $< dst >$
B	Bandwidth
C	Shannon's channel capacity
C_{PNC}	Maximum throughput that can be supported by a PNC
CT^{Asy}	Asynchronous CTA Request
CT^{Iso}	Isochronous CTA Request
$CTA_{m_j}^{Norm}$	Normalized CTA demand of asset $m_j \in M$
$CT_{m_i}^{Unused}$	Magnitude of unused CTA allocation in each child piconet
e_n	Mean service duration of a node $n \in N$
$f_d(s_j\|s_i, a)$	Reward function for the set of disconnected nodes over state change $(s_j\|s_i, a)$
$f_t(s_j\|s_i, a)$	Reward function for the system's throughput over state change $(s_j\|s_i, a)$
$f_l(s_j\|s_i, a)$	Reward function for handover latency over state transition $(s_j\|s_i, a)$
κ	Rician fading parameter
$\mathcal{D}$	Set of PNC capable nodes in a piconet
$\overline{\mathcal{D}}$	Set of child PNCs
$\overline{d_i}$	An element of set $\overline{\mathcal{D}}$
$L_P(t)$	Overall Load (CTA Demand) at PNC P
$L_{\bar{d}_i}(t)$	Overall Load (CTA Demand) at PNC $\bar{d}_i$
$L(t)$	Total load on an SOP structure
$l_{src,dst}$	Link state between any source (src) and destination (dst) node
$L_{\tilde{d}_i}$	Average temporal consistency of a self-backhaul link $l_{\tilde{d}_i,P}$

N	Total number of member nodes in a piconet
N_{T1}	Number of member nodes LoS connected with PNC P
$N_{T2}(.)$	Number of tier-2 member nodes w.r.t each node in N_{T1}
P_r	Average received power
$p_z(x)$	Probability that instantaneous received envelope is greater than z
$Q_{m_i}(t_r)$	Qualitative score of an asset m_i in Superframe t_r
$Q^P(t_r)$	Qualitative score of the portfolio in Superframe t_r
$Q_{m_j}^{Hist}$	Historic values of qualitative asset scores for asset m_j
Q_{Th}^P	Threshold for qualitative score of a portfolio
$Q_{Opt}^P(t_r)$	Optimal qualitative score over an asset portfolio in Superframe t_r
$R_{\lvert\overline{\mathcal{D}}\rvert}$	Number of redundancy combinations for $\lvert\overline{\mathcal{D}}\rvert$
r_{m_i}	Asset return values (for asset m_i)
S	State-space of DT-MDP model
S_L	Set of link states
$SNR^{Th}(.)$	SNR Threshold
$\mathbb{T}$	Decision epoch (in DT-MDP model)
$T_{arr}(.)$	Time until the next node association with respect to a PNC (.)
T_{CTA}	Total CTA duration in a SF
$T_{dep}(.)$	Time until the next node dissociation with respect to a PNC (.)
t_r	Reference Superframe
T_{static}	Duration for which state of DT-MDP model remains unchanged
$T_{\tilde{d}_i}$	Average time required for a self-backhaul link $l_{\tilde{d}_i,P}$ to get blocked
w_P	Fraction of CTA duration that is reserved for PNC P
$w_{\bar{d}_i}$	Fraction of CTA duration that is reserved for PNC $\bar{d}_i$
w^*	Optimal asset weightages
$X_{i,m}$	Ratio of the cumulative p-CTA assigned and demanded at each child piconet
$\Im_{m_i}$	Set of qualitative asset parameters for an asset m_i
$\lambda_{m_j}^{arr}$	Mean rate of increase in connected nodes for asset m_j
λ_P,λ_d	Mean rate for association of DEV nodes with PNC P, d
$\mu_{m_j}^{dep}$	Mean rate of decrease in connected nodes for asset m_j

ψ_k	Weightage assigned to asset parameter k
$\Re$	Set of all asset return values
Θ	Set of mean rate-of-returns for all assets in the portfolio
Σ	Covariance matrix of $\Re$
Δ_m	p-CTA release capacity per asset
ζ_{m_j}	Ratio of normalized CTA demand and optimal p-CTA weightages
$\Gamma(.)$	Gamma Function
$\Phi(.,.)$	Channel quality score of a link
μ_{Th}	Threshold for mean number of blockages
μ_P,μ_d	Mean rate for disassociation of DEV nodes with PNC P, d
σ_{Th}	Threshold for standard deviation of blockage instances
ρ	Measure of traffic intensity
$\zeta(s_j\|s_i,a)$	Total throughput from nodes which will be disconnected due to state change $(s_j\|s_i,a)$
$Lat^{HO}(N)$	Cumulative latency incurred when all DEVs suffer a delay of one (SF) duration
π^{Opt}	Optimal policy for control delegation
π^{Fixed}	A heuristic policy where PNC control always remains with the PNC P
$\pi^{Max-Thpt}$	A heuristic policy where control is delegated to a PNC with maximum throughput
π^{Random}	A heuristic policy where PNC control is randomly assigned to an eligible node

1

Introduction

Contents

1. Introduction

In today's era of ubiquitous network access, the explosive growth of the mobile subscriber base [1], coupled with the evolution of the hardware and services ecosystem, has sharply raised the bar of expectations for the next generation of mobile networks. Today, as we look forward to the global rollout of 5G mobile networks, it is expected that these networks will play a much more pivotal role than before [2], interconnecting both people and a diverse array of devices for a broad range of services. But, to realize this goal, the existing systems will need to be improved and many new technologies will be required [3]- [7].

One of the major challenges confronting today's commercial communication systems is that of spectrum insufficiency. As the frequency bands supporting the existing systems are already congested, there is insufficient scope to accommodate the surging demands. To address this issue at the spectrum level, techniques like *spectrum re-allocation* and *spectrum sharing* have been explored for microwave bands. Spectrum re-allocation [8] involves the re-distribution of the existing microwave spectrum as per their significance. This was indeed done worldwide in the terrestrial TV spectrum for applications like rural broadband access. But, with so much congestion in the radio spectrum, the cost of re-allocation is often prohibitive. Likewise, the spectrum sharing technique [10]- [12] involves scanning for free spectrum using cognitive-radio-based communication systems and using it from time to time when the primary users/applications are not utilizing it. Although it is effective in augmenting the capacity of the existing systems, it cannot guarantee the perpetual availability of spectrum, and hence, cannot be used as a viable alternative. Moreover, the presence of multiple stakeholders operating with diverse priorities also adds to its implementation complexities.

At the same time, new technologies [5]- [9] and system architectures (e.g., Device Centric Architectures, Massive MIMO, Smart Devices, and Native support for M2M communications) have also evolved in recent years. These technologies promise to bring radical changes in the capabilities of our current networks. But, their adaptation into commercial practice would depend on a multitude of factors. Alternatively, a large amount of commercially unused radio spectrum (ranging from 30-300GHz) is available for use at the millimeter wave (mmWave) frequencies. It contains several frequency bands e.g., the E-Band (comprising of 71-76 GHz and 81-86 GHz frequencies), the license-free band (at 60GHz), and the 28-30GHz band. All these have large bandwidths and are capable of supporting high data-rate communication. Moreover, as most of these bands are unlicensed, they can also prove to be economical. Thus, mmWave based communication systems can be considered as potential enablers

for the 5G-based enhanced multimedia broadband (eMBB) applications.

1.1 Challenges in mmWave Based Systems

Despite having large bandwidths and low spectrum costs, communication using mmWave bands entails several problems. These problems mainly emanate from the physical-layer propagation characteristics of these bands. Since mmWave-band frequencies have significantly higher line-of-sight and non-line-of-sight path-loss coefficients (in comparison to that of the existing commercial communication bands) [17]- [28], they tend to attenuate much faster. As a result, for a given operating power, they have small coverage ranges. In addition, due to their low diffraction coefficients [39]- [42] and relatively higher reflection and penetration losses [35]- [38] around common building materials and indoor objects, they are difficult to operate under indoor conditions. To mitigate high propagation losses, mmWave systems use antenna arrays. It improves the link budget by increasing beam directivity and thus contributes towards enhanced coverage range. However, increased beam directivity also leads to directional communication and impacts the Omni-directional channel sensing mechanisms that are used in the existing MAC-layer protocols. As a result, mmWave communication systems face several incompatibility issues while operating on the existing MAC protocols. For instance, due to the sensitivity of mmWave beams towards obstacles and moving objects, the signal strength at the receiver node may fall abruptly and lead to *beam blockages*. Similarly, the absence of proper beam alignment between a pair of communicating nodes leads to *deafness* and can prevent a set of transceivers from exchanging data. Likewise, the process of *neighbour discovery* and *beam training* are also affected.

However, with the recent advances in the fields of MIMO technologies and smart antennas [52]- [55], many of these issues (especially those relating to beam-training, neighbour discovery, and deafness) have been addressed in the recent versions of (mmWave based) directional MAC standards (e.g., [72], [74]). However, some other issues (e.g., those relating to beam blockage, sensitivity towards indoor objects, etc.) are yet to be resolved. Beam blockage leads to unpredictable performance and may cause a mmWave system to operate unreliably. It can also cause over/under allocation of network resources like channel time and bandwidth and can lead to their wastage. Likewise, the sensitivity of mmWave beams towards common indoor objects coupled with their high path loss coefficients force mmWave systems to operate in small cell sizes. It can also cause the member nodes to undergo frequent handovers even under conditions of low mobility. Therefore, applications that need low latency will

suffer severe performance bottlenecks.

Thus, in view of the above, this thesis aims to investigate and develop different solutions to mitigate beam-blockage in mmWave networks and to address and resolve, to the extent possible, the various issues which lead to their inefficient operation.

1.2 Motivation and Research Objectives

The mmWave systems can become commercially viable only if they can provide reliable and cost-effective connectivity at high data rates. Therefore, it is essential to fix the shortcomings of these systems. Since beam-blockage is a major problem in mmWave systems, different types of blockage-mitigation solutions have been discussed in the literature. However, the proposed solutions have several shortcomings which make them unsuitable for different application scenarios. Therefore, in this thesis, we discuss various solutions to address these issues, as described briefly below:

(i) With regard to the problem of blockage-mitigation, it may be noted that Physical-layer solutions (e.g., techniques using beam switching or beam-diversity) generally require customization in the antenna module and changes in the related signal processing hardware. Additionally, the extent of such customizations (e.g., the number of simultaneous beams required) may vary from one deployment scenario to another, making them difficult to implement. On the other hand, the network-layer-based approaches (e.g., dual connectivity and multi-AP-connectivity based solutions) are infrastructure intensive and require the deployment of several additional network components. This leads to greater system complexity and higher capital (CAPEX) and operational (OPEX) expenses. This would make them economically infeasible to use in various low-cost deployment scenarios such as indoor residential or office spaces where high data-rate traffic is nevertheless required [80]. Therefore, in this thesis, we aim to develop various low CAPEX, OPEX based solutions that can help mitigate beam-blockage in indoor conditions.

(ii) Since the network-layer and MAC-layer based blockage-mitigation solutions require deployment of multiple network elements or relays, the implementation of mobility or blockage induced handover events can lead to added signalling complexity and hence increased latency. As a result, these solutions may not be suitable for many 5G applications that are based on ultra-reliable low-latency communication (URLLC). Thus, in this thesis, we aim to develop some

MAC-layer based techniques which would enable our proposed blockage mitigation approaches to accommodate low-latency handovers.

(iii) The network and the MAC-layer based blockage-mitigation solutions available in the literature are not linearly scalable. Therefore, with an increase in the system size (either due to an increase in node density at the hotspots or through an increase in overall node count) or any other changes in the mobility-state of the member nodes, the supporting network infrastructure has to be ramped up much faster at a non-linear scale. Moreover, for very large networks, the overheads (in terms of the number of network components and system complexity) can become prohibitively large enough to preclude the implementation of some of these solutions. It should also be noted that the discussed physical-layer blockage mitigation methods have generally not considered the relevant network architectures or the MAC-layer protocols through which the proposed solutions can be implemented. Therefore, in this thesis, we aim to explore some network centric frameworks which would enable our proposed blockage-mitigation solutions to operate seamlessly over different network sizes (and configurations) without requiring any additional hardware.

(iv) As discussed in the earlier section, sudden link outages due to beam-blockage may lead to misallocation of the network resources in the MAC layer. As a result, some of the blocked links are allocated channel-time and bandwidth that they cannot use whereas links that are active are deprived of network resources. All this leads to inefficient operation and wastage of network resources. Therefore, in this thesis we aim to develop effective resource allocation mechanisms, which would allow mmWave networks to optimally allocate their resources under dynamically changing network conditions.

(v) The MLC-architecture based blockage-mitigation solutions (mostly the network and MAC layer solutions) operate inefficiently in order to maintain a certain level of redundancy. However, as the blockage scenario changes from one environment to another or changes over time, a fixed amount of redundancy may not be required to achieve a given grade of blockage-reliability. Existing MLC solutions cannot adapt their redundancy levels to respond to this. This also leads to inefficient operation and wastage of network resources. Hence, in this thesis, we aim to develop mechanisms which would enable MLC solutions to regulate their redundancy levels

depending on the network conditions and operate with a given grade of reliability.

1.3 Thesis Contribution

This thesis focusses on low-cost and easy to implement solutions that mitigate beam-blockage in mmWave networks. It also addresses some of the resource allocation issues that are caused due to beam blockage and proposes techniques to improve the efficiency of existing blockage mitigation solutions, which are based on the MLC architecture. In this thesis, we have targeted the low-cost indoor deployment scenarios, as they contribute a significant share of high data-rate traffic [80], but where the existing blockage-mitigation solutions cannot be implemented due constraints of high CAPEX and OPEX. Our proposed blockage-mitigation solutions are based on the MAC-layer technique of control delegation which is supported by the popular IEEE MAC-layer standards [72], [74]. Therefore, their implementation does not require any protocol level changes. To address the resource allocation issues caused due to beam-blockage, we consider the SOP architecture of the IEEE 802.15.3c MAC-standard [72] and use a portfolio theoretic model to optimize the resource allocation process. The main contributions of this thesis are listed next.

(a) **Blockage Mitigation using Dynamic Control Delegation:** In this chapter, we have proposed different types of blockage-mitigation approaches based on the MAC-layer technique of dynamic control delegation (DCD). The technique utilizes the ***PNC Handover*** procedure [72] to dynamically reposition a piconet controller (PNC) and mitigate beam-blockage. The following are the novel features of this technique: Firstly, a static-policy based DCD methodology is presented. It uses a fixed set of delegation rules to mitigate beam-blockage under both static and dynamic network scenarios. Secondly, a dynamic policy based optimal delegation model is presented. It accounts for the blockage dynamics of the network and uses a Discrete Time Markov Decision Process (DT-MDP) based framework to derive the ideal delegation policy. The obtained results demonstrate that the proposed solution can significantly reduce beam-blockage in a piconet while fulfilling a variety of other performance objectives.

(b) **Efficient Blockage Mitigation in MLC Architectures:** In this chapter, we have proposed the DC-DLLR approaches. These correspond to the device centric (DC) methods for achieving dynamic link-level redundancy (DLLR). They are applied in the context of blockage-mitigation solutions that use the multi-link-connectivity (MLC) architecture to achieve reliable connectiv-

ity. The novel features of this approach are as follows: It incorporates the ability to regulate redundancy levels in MLC-architecture based blockage-mitigation solutions and enables them to operate more efficiently. In addition, the DC-algorithms are easier to implement and modify (through device-level driver updates), and hence, they are cost-effective and more preferable. The obtained results have shown that DLLR approaches can be used to significantly improve the resource utilization of an MLC network by minimizing its usage of redundant infrastructure.

(c) **Resource Allocation in Blockage-prone SOP Structures:** In this chapter, we have proposed two types of MAC-layer approaches (Feedback-driven and portfolio theory based (PACTA)) for distribution of network resources in mmWave SOP architectures. They enable mmWave SOPs to operate under blockage-prone conditions and allocate their channel time resources more efficiently. The following are the novel features of our discussed approaches: The Feedback driven approach obtains channel time requirement data from its dependent piconets of the SOP structure and utilizes this information to distribute the network resources using a weighted approach. The technique helps in reducing the wastage of network resources and also ensures fairness of channel time allocation. In the second approach (i.e., PACTA), a quality-of-service (QoS) aware, risk sensitive approach for channel-time allocation is presented. It considers the SOP structure as an asset portfolio and models the p-CTA allocation problem as an optimization problem involving multiple QoS parameters. The obtained results have demonstrated that this approach can be used to allocate network resources with a certain grade of efficiency while considering multiple QoS parameters over blockage-prone mmWave SOPs.

1.4 Thesis Organization

The overall structure of this thesis is given in Fig. 1.1. Under this structure, the chapters are organized as follows:

Chapter 1 discusses the limitations of existing communication systems vis-a-vis the demands of futuristic networks and evaluates the prospects of using mmWave communication to meet these requirements. It then discusses various shortcomings of mmWave systems at the MAC-layer, which arise due to their propagation characteristics and states the salient features of the contention based synchronous MAC protocols through which they are operated. Finally, the chapter summarizes the thesis contributions and provides a brief outline of the thesis structure.

Chapter 2 discusses various studies to highlight the benefits and shortcomings of mmWave band communication. It also discusses the literature on various state-of-the-art blockage mitigation techniques along with their advantages and disadvantages. Thereafter, it highlights various issues related to inefficient allocation of network resources and presents the existing literature for the available solutions. Finally, it summarizes various MAC standards, which can be used to support the available solutions.

Chapter 3 presents a MAC-layer based technique, which uses the method of control delegation to achieve blockage tolerance. The technique is ideally suited for low-cost indoor deployment scenarios with low user mobility where resource-intensive network-layer solutions cannot be implemented because of cost-constraints. This technique works by virtually relocating the AP node (through control delegation) to different vantage points from time-to-time depending on the blockage scenario in the network. Here, two different classes of delegation approaches are proposed and evaluated, the first one uses a static set of rules to regulate the delegation decisions whereas the second class of approach uses a discrete time Markov decision process (DT-MDP) model to dynamically determine the delegation policies.

In **Chapter 4**, we focus on the MLC-architecture based blockage mitigation solutions. Since, these methods use multiple redundant links (either using multiple radio access technologies (RAT) or radio access networks (RANs)) to connect the member nodes, the same amount of redundancy is not required in all scenarios and over all time. Therefore, in this chapter, we propose different types of device centric methods to regulate the extent of link-level redundancy and evaluate their performance with respect to the static redundancy method.

In **Chapter 5**, we address the issue of blockage induced mis-allocation of network resources (channel time, bandwidth, power etc.) in mmWave networks. We consider the IEEE 802.15.3c MAC standard based simultaneously operating piconet (SOP) architecture and discuss two different types of approaches for efficient allocation of network resources. In the first approach, a feedback driven mechanism is used to address the issues of over/under allocation of network resources whereas in the second approach, the SOP architecture is modelled as a portfolio of assets and a QoS aware risk sensitive approach (based on Markowitz's model) is adopted for optimal resource allocation.

Chapter 6 concludes this thesis by summarizing the research work and includes some suggestions and pointers for future research.

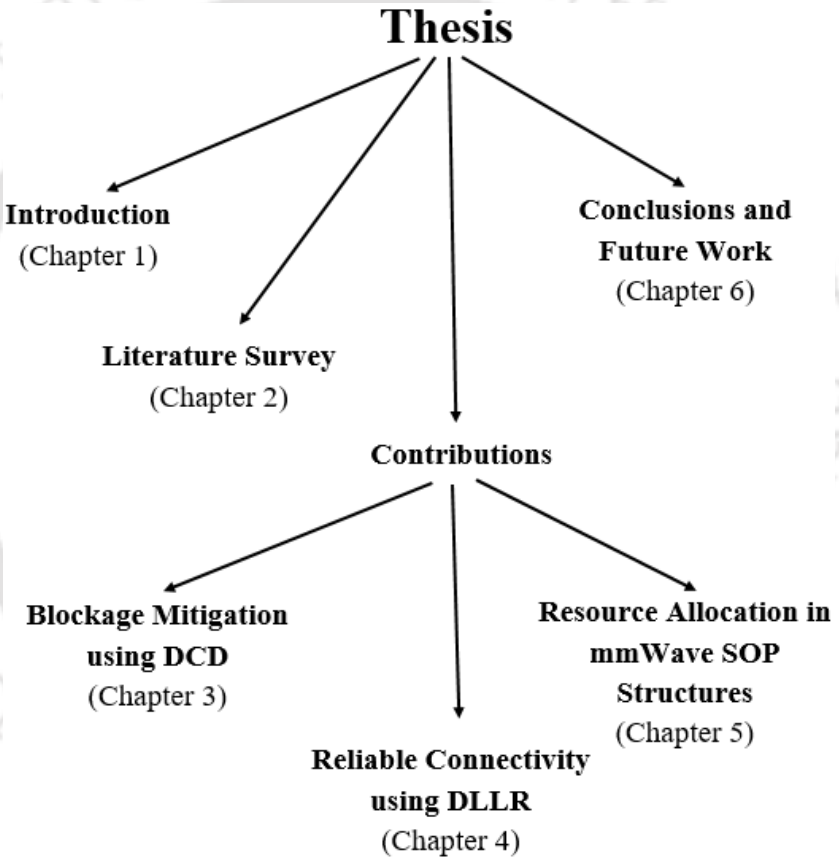

Figure 1.1: Structure of the thesis

2

Literature Survey: Review of Related Work

Contents

This chapter presents various studies to highlight the benefits and shortcomings of mmWave band communication and discusses its impact on the existing MAC-layer standards. It starts by discussing different studies which have analysed and compared the role of several key technologies in transforming the current generation of communication systems towards the 5G standards. Subsequently, it considers the mmWave based communication systems and discusses their propagation characteristics and limitations in the MAC layer. It also reviews the existing literature and discusses various state-of-the-art blockage mitigation techniques along with their advantages and disadvantages. Finally, it discusses various resource allocation issues that are caused due to beam-blockage and reviews the literature for their solutions while discussing their supported MAC standards.

2.1 Introduction

As discussed in Chapter 1, the existing commercial communication systems are ill-equipped to meet the demands of the surging subscriber base and new applications and services. In addition, the crowded nature of the currently used commercial spectrum and its inability to accommodate the new types of services leads to the problem of spectrum insufficiency. Since spectrum congestion is not uniform across all the frequency bands, the technique of spectrum restructuring (or reallocation) has been explored to accommodate the new services through the existing spectrum [8]. However, due to their prohibitive costs and their implementation complexities, such processes are not effective. As an alternative approach, the technique of spectrum-sharing has been explored in [10] - [12]. It involves sharing of the existing spectrum between multiple users to improve spectral efficiency. To evaluate this technique, the effectiveness of multiple spectrum-sharing technologies like Cognitive Radio (CR), Device-to-Device (D2D) communication, Non-Orthogonal Multiple Access (NOMA) Technologies, and In-Band-Full-Duplex (IBFD) communication has been analysed in [10]. Similarly, in [11] and [12], the scope of dynamic spectrum sharing in vehicular communications and various types of (licensed and unlicenced band) IoT technologies have been evaluated.

To identify the disruptive technologies that could possibly play a pivotal role towards the realization of 5G standards, [3], [5] - [9] have analysed various emerging technologies (viz. device-centric architectures, mmWave communication, massive MIMO, smarter devices, and native support for machine-to-machine communications, etc.) and categorized them in terms of various metrics. For instance, in [3], Boccardi *et al.* have used the Henderson-Clark model [13] to categorize these technologies in

terms of their evolutionary or disruptive nature and classified them in terms of their ability to influence the existing device-level and network-level architectures. The study suggested that mmWave communication would have a maximal impact on the legacy device and network-level architectures. Similarly, in [6], Zhuang *et al.* studied a few emerging technologies (e.g., mmWave wireless, the Internet of Things (IoT), Fog Computing, and Software-Defined Networking (SDN)) from the standpoint of whether their adoption would spur bandwidth growth at edge networks. It concluded that compared to SDN and IoT, mmWave wireless and Fog Computing are most likely to bring sweeping changes in the bandwidth usage of the end-users. However, as the 5G standards demand a broad range of service improvements (e.g., the realization of Gigabit, real-time, and ultra-reliable communications, supporting an extremely large number of wireless connections for both human and machine-type wireless applications, diverse set of mobile traffic with different characteristics, and QoS, and achieving more spectrum, energy, and cost-efficiency, etc.), any individual technology cannot be used to meet all these expectations. Thus, in [7] and [9], researchers have suggested that a number of enabling technologies and techniques must be developed and implemented in tandem to realize the goals of 5G standards.

As a niche segment of the 5G based services, the enhanced multimedia broadband (eMBB) services are given special importance due to their commercial significance. They constitute the high data-rate, bandwidth-hungry class of applications that contribute a major share of network traffic [1]. In most of the studies discussed earlier, mmWave band communication has been proposed as a technology enabler to support the eMBB applications. Moreover, due to their large bandwidths and mostly unlicensed spectrum, mmWave bands can offer a cost-effective solution to the problem of spectrum insufficiency.

To gauge the extent of link-level performance gains achievable by using this spectrum, several experimental test-bed trials have been carried out in [14] - [16]. They have demonstrated that mmWave band frequencies can indeed be used to achieve data rates in the range of tens of Gbps. Such values far exceed the ones that can be achieved using the existing commercial systems (operating on standards like the long-term evolution (LTE) and the LTE-Advanced (LTE-A)), thus underscoring the potential for this technology.

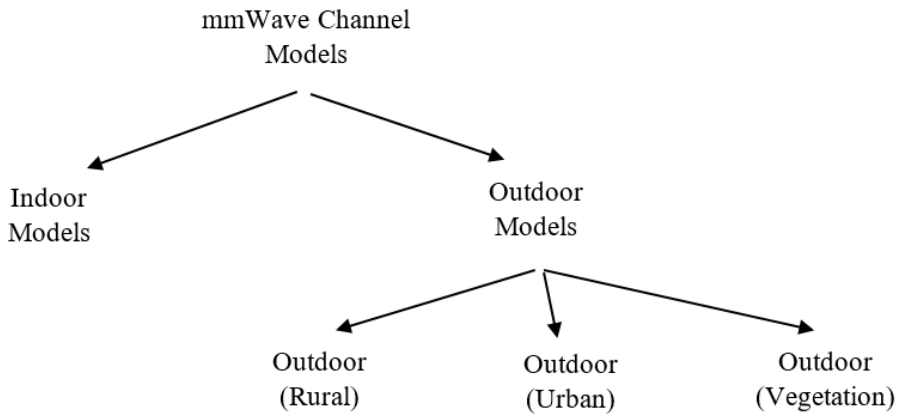

Figure 2.1: Types of channel models in mmWave communication systems

2.2 Propagation Characteristics of mmWave Bands

To implement communication systems that operate over the mmWave spectrum, it is necessary to systematically explore and characterize the wave propagation characteristics of these bands. Therefore, several experimental studies have been undertaken to characterize their propagation behaviour. These studies have focused on various aspects of mmWave propagation like variation of path-loss coefficients, diffraction properties, and signal absorption through different objects and building materials. In addition, these parameters can also be influenced by their operating environments and their frequency band of operation. Therefore, in this section, we review the literature to characterize all these aspects of mmWave propagation.

2.2.1 Path-loss Characteristics in mmWave Bands

Unlike the currently used commercial spectrum, the propagation characteristics of mmWave frequencies are sensitive to their deployment conditions and operating frequencies. Therefore, their propagation characteristics are classified into different categories as shown in Fig. 2.1. Each of these categories presents a distinct form of the propagation environment. For instance, in the outdoor scenarios, the propagation environment under rural conditions can be quite different from the urban conditions (in terms of the size of the environment, the nature of objects in its background, their densities, etc). Similarly, within the indoor scenarios, the propagation environments under residential conditions can be quite different from that of the industrial or office environments. Therefore, different channel models are derived for each of these conditions to characterize their wave-propagation

behaviour.

To analyze the outdoor environments, MacCartney *et al.* [17] - [19], have studied the lately introduced mmWave based Rural-Macrocell (RMa) model from the 3rd Generation Partnership Project (3GPP) TR 38.900 (Release 14) [20] and evaluated its accuracy with respect to various bands of mmWave spectrum. Although the RMa model [20] has been originally derived for frequencies below 6 GHz and asserted for use up to 30 GHz, the study flagged concerns about its accuracy. The researchers used 73 GHz-based measurement campaigns in rural Virginia to propose an improved RMa path loss model that is more accurate and easier to apply. It also showed that the new model is applicable over a wider range of frequencies (0.5 to 100 GHz) and for varying transmitter antenna heights.

With regard to the outdoor (urban) models, MacCartney *et al.* [21] have conducted ultra wide-band propagation measurements in downtown Manhattan and presented new Urban-Macrocell (UMa) path loss models for the 28 GHz and 73 GHz bands. The obtained results have shown that the Non-Line-of-Sight (NLOS) path loss exponents (PLE) for both the 28 GHz and 73 GHz bands are the same (i.e., 3.4). In addition, the measurements also showed that mmWave channels are more directional at both the TX and RX than conventional UHF/Microwave channels. Similar experimental trials were also conducted in Brooklyn [22]- [25] for these bands. With respect to [24], the measurements were taken for backhaul and mobile wireless communication channels using steerable antennas. It was observed that for the Line-of-Sight (LoS) conditions, the PLEs are 2.57 and 2.58 respectively for the mobile and the backhaul scenarios (without using the transmitter (TX) antenna height diversity). In addition, it was observed that, for the NLoS conditions, the PLE values get reduced while using the best link (i.e., from 5.96 to 4.29 while considering the mobile scenarios, and from 5.88 to 4.44 while considering the backhaul scenarios). Thus demonstrating their feasibility of directional communication. For characterization of the remaining mmWave bands, [26], [27] and [28] have conducted propagation measurement studies for the 38 GHz band (in Austin, US), and for the 2, 10, 18, and 28 GHz bands (in Aalborg, Denmark). The studies were focused on the characterization of key parameters like the LoS probability, large-scale path loss, and shadow fading models, etc. To investigate the other vital channel model parameters, [29] has studied the small-scale spatial fading characteristics and the autocorrelation of received signal amplitudes at the 73 GHz band, for both the omnidirectional and directional receiver antenna patterns (in the LoS and NLoS environments). Likewise, to improve upon the accuracy of the existing models or to simplify the current ones, [30] has compared two

candidate large-scale propagation path loss models viz., the alpha-beta-gamma (ABG) model and the close-in (CI) free space reference distance model and showed that the one-parameter based CI model can provide similar goodness of fit (for both LoS and NLoS conditions) while offering significant improvement in simplicity over the three-parameter based ABG model. Similarly, in [31], Samimi *et al.* have attempted to develop an accurate 3GPP-like channel model using the empirical distributions for time cluster and the spatial (lobe) channel parameters.

In the indoor scenarios, [31], [32] and [33] have conducted penetration loss measurements and analysis for the 28 and 73 GHz bands using wideband sliding correlator channel-sounder-based measurement campaigns for office environments. In [31], the indoor reflection, scattering, and transmission parameters were evaluated using some common building materials like drywall and clear glass, and the corresponding large-scale path loss model was developed. Similarly, in [32] and [34], the penetration loss measurements were carried out for many of the common indoor building materials such as glass doors, glass windows, closet doors, steel doors, and whiteboard writing walls. Likewise, [35] - [38] have also presented large-scale path loss models for different types of indoor scenarios e.g., indoor office layouts (corridor, open-plan, and closed-plan) and shopping malls using extensive measurement campaigns. The obtained results have indicated that the extent of penetration losses over these environments is largely dependent on the presence of these materials in form of obstacles. Further, the extent of these losses also tends to increase with an increase in the operating frequency. In [38], it was reported that the PLEs for LoS transmissions were identical (i.e., 1.7 and 1.8 respectively) for the 28 GHz and the 73 GHz bands, and for the NLoS transmissions, the PLE values were higher than that in the case of LoS scenarios.

2.2.2 Diffraction Properties in mmWave Bands

As the spectrum for commercial communication would eventually expand to the higher frequency bands, the characterization of diffraction properties in various mmWave bands becomes essential. Although the significance of diffraction has been thoroughly investigated in the lower frequency bands, it has not yet been properly studied at the mmWave frequencies. Moreover, as diffraction can occur from a multitude of sources in dense urban and indoor conditions, it becomes essential to incorporate their influences in the relevant propagation models. In this reference, [39] has presented the measured results from a building-corner diffraction measurement campaign over the 28 GHz band. The obtained results demonstrate that the diffraction losses have little dependence on the type of polarization and the

choice of building material. Similarly, in [40] - [42], researchers conducted measurement campaigns for a variety of outdoor conditions over different frequency bands (e.g., the 10 GHz, 20 GHz, 26 GHz, and the 60 GHz bands) using a pair of directionally steerable antennas. In this, Lu *et al.* [41] investigated the characteristics of the diffracted and the scattered waves for different types of (mobile-to-mobile, access, and backhaul) radio links over the 60 GHz band. Their study focussed on the effects of diffraction at building corners, scattering by cars, lampposts, buildings, and even human blockages. The obtained results demonstrated that the contributions from vehicular and lamppost scattered paths can be dominant compared to corner diffracted paths under dense urban scenarios. Similarly, in [42], Deng *et al.* compared the obtained results in reference to the Knife Edge Diffraction (KED) model [43]. They observed that the diffraction losses tend to increase with frequency in outdoor scenarios and that the accuracy of the KED model is higher around the rounded corners in outdoor environments.

For the indoor scenarios, [42] and [44] have conducted extensive measurement campaigns to study diffraction from various types of objects e.g., edges, wedges, and cylinders over a wide range of frequencies. The experiments considered different types of materials e.g., metals, wood, and plastic, and validated the observed results against various theoretical approaches. Furthermore, it also investigated the shadowing of rays by humans and modelled them with the help of diffraction. The observed results indicate that diffraction at edges or wedges can be neglected almost everywhere in a room. However, under the NLOS conditions (in the few cm wide region close to the incident shadow boundary), diffraction can observably influence both the path loss and the temporal channel characteristics.

2.2.3 Effect of Human Blockage and Other Factors on mmWave Propagation

As mmWave signals can also get attenuated due to the presence of humans as obstacles, it becomes essential to characterize the behaviour of rapidly fading channels caused by pedestrians in dense urban and indoor environments. In this respect, [45] has performed human blockage measurement studies at 73 GHz to analyse the shadowing effect of a moving human body while using a pair of directional antennas at the transmitter and the receiver terminals. The obtained results indicate high levels of shadowing attenuation. The study reported that an average-sized male (with a body depth of 0.28 m) could cause around 30-40 dB attenuation while using directional antennas. Similarly, in [46]- [48] has presented a novel spatial dynamic channel sounding system. It operates on the 60 GHz band and obtains the spatial dynamics of mmWave channels using phased arrays. Likewise, in [49], Sato

et al. have estimated the propagation-path visibility in office environments where mmWave links are subjected to shadowing by human bodies and suggested diversity switching as a means for retaining radio visibility.

Apart from these effects, the propagation of mmWave signals can also be influenced by a number of other factors like the atmospheric pressure, moisture content, particulate matter and composition of other gases in the propagation medium. A detailed account on the characteristic of these effects is available with the Federal Communications Commission (FCC) [50].

2.2.4 Implication of PHY Layer Characteristics in the MAC Layer

As discussed in the previous sub-sections, the high propagation-losses in mmWave frequencies coupled with their poor diffraction abilities and their relatively higher reflection and penetration losses around common building materials and indoor objects complicates their physical and medium access control (MAC) layer operations. Consequently, the networks operating on these bands perform unreliably and face a number of issues as discussed below:

Due to the high path-loss coefficients in the mmWave bands and the restrictions on the peak operating power for the wireless devices (under the Federal Communications Commission (FCC) rules [51]), these systems use antenna arrays and communicate with each other using directional beams. However, it affects the omnidirectional channel sensing mechanism that is used in the existing MAC-layer protocols and causes various problems e.g., beam blockage, deafness, beam-misalignment, and neighbour discovery issues. In addition, due to the poor diffraction abilities in the mmWave bands and their sensitivity towards common building materials and household objects, these systems suffer from abrupt beam blockages and operate unreliably. With the recent progress in the field of smart adaptive antennas [52] - [55] and the updated MAC protocols [56], most of the issues related to beam training, neighbour discovery, and deafness have been addressed. However, the problem of beam blockage remains unresolved. Although several blockage mitigation solutions have been proposed in the literature, they possess one or the other shortcomings. The details of each of these solutions have been discussed in Section 2.3. Apart from this, beam-blockage also causes misallocation of network resources in certain types of network architectures and leads to operational unreliabilities. We review the literature on all these issues and discuss the proposed solutions in the subsequent sections.

2.3 Mitigation of Beam-Blockage in mmWave Systems

This section reviews the literature on various types of blockage mitigation solutions. The solutions are categorized further into different groups based on their layer in the open systems interconnection (OSI) model. Accordingly, three types of blockage mitigation solutions viz. Physical, MAC, and Network layer solutions have been discussed. The physical layer solutions (e.g., beam-switching, beam-diversity, etc.) require customization in the antenna module and relevant changes in the related signal processing hardware, whereas the network and MAC-layer-based solutions generally involve the deployment of multiple network elements in the form of relays, routers, load balancers, etc.

2.3.1 Physical Layer Solutions for Blockage Mitigation

To mitigate beam-blockage using physical layer techniques, [57] has investigated the robustness of link connectivity over the 60 GHz band and evaluated the prospect of reliable connectivity using reflecting surfaces in the background. It considered various indoor scenarios and calculated the probability of link outages using a 3D tracing tool. It demonstrated that the probability of link outage is inversely proportional to the obstacle density and that the average reflection loss in indoor conditions is 15-20 dB. Finally, it concluded that mmWave links operating in NLoS conditions would be vulnerable to outages even under moderately populated indoor environments.

To address this problem, Zhang *et al.* [58] have evaluated the prospect of using tuneable reflectors to augment the transmission environment and enhance mmWave vehicle-to-infrastructure (V2I) communication. They have suggested the idea of deploying cheap and highly reflective metallic plates as tuneable reflectors in dynamic vehicular environments to create alternate NLoS links and support high data-rate communication in blockage-prone environments. Likewise, in [59], Yiu *et al.* have proposed the use of static reflectors in strategic locations of an indoor environment to provide alternate coverage paths for beam propagation. However, given the implementation complexities and the high values of reflection losses, these solutions are not viable. In [60] and [61], the technique of switching beams from LoS to NLoS links in case of blockage in the primary (LoS) link has been investigated for mitigation of beam blockage. [60] proposes a low-latency beam-steering algorithm (which utilizes the previously valid link knowledge) to re-establish connectivity in blocked LoS links. Similarly, in [61], An *et al.* have considered 60 GHz based indoor networks to evaluate two types of Beam-Switching (BS) mechanisms viz. instant-decision based BS and environment-learning based BS to switch over

from blocked LoS links to NLoS links. However, in practical scenarios, when a link is blocked, the delay incurred in selecting and re-aligning backup NLoS links can often become unacceptably large to sustain uninterrupted communication. Therefore, solutions involving diversification of the transmitted beam have been suggested in [62], [63]. These employ multiple beams simultaneously between a pair of transceivers to ensure that the connectivity is retained even when one of the links is blocked. In [62], Park *et al.* have used an indoor Wireless Local Area Network (WLAN) scenario operating on the 60 GHz band to demonstrate that spatial diversity technique can maintain a stable link quality under human-induced shadowing. Similarly, in [63], Xiao *et al.* have analysed two different types of spatial diversity techniques and compared their effectiveness in combating human-induced shadowing for the 60 GHz-based WLANs. Although these techniques are effective in tackling beam blockages, they consume a lot of additional network resources and lead to the underutilization of network capacity. As a cost-effective approach, [64] has proposed the technique of beam widening and optimization for mitigating beam blockages. Using a 60 GHz-band-based indoor mmWave network scenario, the researchers evaluated the effect of beam width adaptation on beam-blockage and observed that optimal beam-width adaptation can achieve up to 13 dB gain in received signal strength (RSS). However, in mobile scenarios, the delay incurred in the determination of the optimal beamwidth can pose as a bottleneck towards the maintenance of stable connectivity.

2.3.2 Network Layer Solutions for Blockage Mitigation

Considering the network-layer solutions, [65] has proposed a dual-connectivity-based framework to mitigate beam blockages. The framework consists of a heterogeneous network structure where member nodes are connected simultaneously to an LTE network and multiple mmWave small-cells. In case of abrupt link outages, the framework facilitates the member nodes to collect various network parameters (with the aid of the LTE network's eNodeB (eNB)) and perform fast switching to fall back to LTE and schedule for a fast handover among the mmWave eNBs. The obtained results demonstrate the effectiveness of this approach in improving the performance of an end-to-end network in terms of several key factors like latency, throughput, and packet loss. In [66], Gerasimenko *et al.* have proposed multi-connectivity as an alternative for the beam-switching technique and conducted a detailed evaluation to measure the impact of various system parameters (e.g., access point (AP) density and height, blocker density and speed, number of antenna array elements, array switching time, etc.) on the ergodic capacity. By using various types of multi-connectivity strategies, they

demonstrated that dual connectivity can indeed be used to deliver the desired performance. Similarly, in [67], Yang *et al.* used a multi-AP architecture and proposed joint optimization of the AP selection, bandwidth allocation, adaptive modulation, and power allocation processes to satisfy different QoS requirements of indoor devices while maximizing the network data rate. Likewise, [68] has proposed a Markov Decision Process (MDP) based framework to model the blockage dynamics in a mmWave multi-AP architecture and proposed a distributed multi-objective optimization approach to select AP nodes to mitigate beam blockages. Although most of these solutions demonstrate promising results, they are generally resource-intensive. Since maintaining simultaneous connectivity across multiple access points or through multiple radio access technologies (RATs) can substantially increase the network and device-level complexities, they can also increase the resource consumption of a network. As a result, these solutions may become unviable for many low-cost indoor application scenarios.

2.3.3 MAC Layer Solutions for Blockage Mitigation

Finally, considering the MAC-layer-based solutions, [69] has proposed a relay-assisted QoS aware scheduling approach for blockage mitigation in mmWave backhaul networks. The solution consists of a relay selection algorithm and a transmission scheduling algorithm. The relay selection algorithm selects non-repeating relay nodes (with high link rates) to bypass the blocked flows, whereas the transmission scheduling algorithm exploits the concurrent transmission opportunities to improve the network capacity. The researchers conduct extensive simulation trials to demonstrate the effectiveness of the proposed approach in mitigating beam blockages. Similarly, in [70], Niu *et al.* have also proposed a multi-hop relaying transmission (MHRT) scheme to establish multi-hop relay paths and steer blocked flows around obstacles. In [71], Singh *et al.* have proposed a cross-layer modelling methodology and a multi-hop MAC architecture to utilize the 60 GHz spectrum while mitigating beam blockages. Their proposed solution uses an elementary diffraction-based model to determine network link connectivity and uses the multi-hop MAC protocol to regulate directional transmission and reception. By using crowded indoor scenarios, the researchers demonstrate robust connectivity despite the fragile nature of individual links. Although these approaches can effectively mitigate beam blockages, they generally involve additional infrastructure and network complexity. In addition, relays can also perform poorly under bidirectional traffic conditions.

2.4 Mitigation of Unreliability and Resource Allocation Issues in mmWave Systems

As discussed in the earlier sections, beam blockage can also induce reliability and resource allocation issues in the mmWave networks. For instance, in the mmWave SOP architectures [72], beam blockage can cause misallocation of channel-time resources and lead to poor efficiency. To address these inefficiency issues at the MAC layer, [75] and [76] have suggested several changes in the IEEE 802.15.3 standard. In [75], Sindian *et al.* have proposed a fairness-centric approach for channel time allotment. It involves dynamic adjustment of the Superframe duration to accommodate the rapidly changing channel-time demands of an SOP hierarchy. Similarly, in [76], researchers have suggested a distributed approach for forming SOP hierarchies. The approach enables a piconet-controller (PNC) capable member node to check the availability of network resources in its parent Superframe and take decisions on extending the hierarchy. Likewise, in [77], Xue *et al.* have addressed the issue of interference mitigation in densely deployed mmWave SOPs. They propose an adaptive channel-time allocation mechanism to manage the inter-piconet interferences and improve the network throughput. Using simulation trials, they demonstrated that the proposed approach is effective in improving SOP throughput while maintaining a high link success probability.

To mitigate channel-time wastages that are caused due to beam blockage, [78] and [79] have proposed different resource allocation mechanisms. In [78], Shrestha *et al.* have presented a dynamic queue-length-based time-slot allocation methodology that can improve the channel utilization of a mmWave network while operating under uncertain queue length information. Likewise, in [79], Huang *et al.* have proposed a traffic prediction-based dynamic time slot allocation mechanism. It involves the coordinator node to collect the transmission queue length information from all the nodes to predict the real-time traffic arrival and take dynamic time slot allocation decisions.

Since the distribution of network resources (channel-time, power, bandwidth etc.) among the member nodes (or subsidiary PNCs) can be influenced by a number of other factors apart from beam blockage e.g., operator preferences, traffic pattern, mobility considerations etc., in Chapter 5 we have discussed various proactive and reactive approaches for ideal resource allocation. Similarly, Chapter 4 aims to develop some device centric redundancy regulation approaches that can enable a mmWave network to operate with low capital expenditure (CAPEX) and operational expenditure (OPEX) footprints.

3

Blockage Mitigation in mmWave Networks using Control Delegation

Contents

This chapter proposes a MAC-layer based methodology for mitigation of beam-blockage in mmWave networks. It utilizes the technique of control delegation (as defined in IEEE 802.15.3c MAC standard [72]) to achieve blockage tolerance. This is an inexpensive technique and does not require any dedicated customization in device hardware or any additional network components, making it ideal for deployment in low-cost indoor scenarios. The results obtained through extensive simulation trials have demonstrated that dynamic control delegation (DCD) based approaches can be used to effectively mitigate beam-blockage and achieve multiple performance objectives over different indoor environments.

3.1 Introduction

Wireless communication using mmWave spectrum offers tremendous opportunities to facilitate high data-rate communication at an affordable cost and promises to augment the existing sub-GHz band communication systems for supporting future 5G applications and services. However, the typical wave propagation characteristics in these bands may cause several complications in the MAC layer. This would lead to unreliable performance making its prospects for commercialization difficult. Since beam blockage is a major cause of these problems, different types of blockage-mitigation solutions have been proposed in literature. A detailed review of these along with their merits and demerits has been presented in Chapter 2. Each of these solutions operate either at the device level or at the network level and employ different techniques based on the Physical, MAC or the Network layers to overcome beam blockage. However, with regard to their viability under diverse deployment scenarios, there are still some unresolved issues. Since, a major share of high data-rate traffic is generated indoors [80], scenarios like residences, warehouses, offices, malls, airport, stations etc. would be the target scenario of deployment for these networks. In most of these scenarios, user and obstacle densities are high with limited user mobility and these networks are typically operated with low-cost infrastructure and resources. Unfortunately, most of the proposed blockage-mitigation solutions are either infrastructure intensive or consume substantial additional network resources. For instance, the physical layer solutions based on line-of-sight to non-line-of-sight (LoS-NLoS) beam switching (e.g., [60], [61]) are not amenable for high data-rate communications due to excessive signal-strength attenuation in NLOS conditions whereas the solutions involving beam-diversity (e.g., [62], [63]) and usage of static reflectors [59] need additional network infrastructure to support their operations. Similarly, in the network and MAC-layer solutions, the heterogeneous architecture-based LTE-mmWave dual connec-

tivity approach [65] and techniques employing redundant access points [66]- [68] and relays [69], [71] also require additional network infrastructure and resources to achieve blockage tolerance. Thus, the overheads of implementing these solutions may be prohibitively large.

In this chapter, we propose and present the DCD approach for blockage-mitigation as a more practical solution for this. It is based on the MAC-layer method of control delegation and targets low-cost indoor deployment scenarios with low infrastructure and resources. The main advantages of using this technique are:

(i) It is inexpensive and does not require any dedicated changes in the device hardware (as required in the case of the physical layer solutions) to incorporate blockage tolerance.

(ii) It also does not require any additional network infrastructure in the form of relays, access points, load balancers etc. as needed in the case of the network and MAC layer solutions.

(iii) The main tenet of the proposed methodology (i.e., control delegation) is supported by all the major IEEE standards e.g., IEEE 802.15.3c [72] and IEEE 802.11ad [74]. Therefore, the technique can be seamlessly implemented over a wide range of devices.

(iv) The objective function in the proposed approach can be easily re-configured based on operator requirements. Therefore, the system can adapt to different operating conditions and performance objectives.

3.2 DCD Approach for Blockage Mitigation

In this section, we describe our proposed DCD approach. We start by discussing the network architecture and the process for implementing DCD under the IEEE 802.15.3c MAC standard. We then discuss some static rule-based DCD approaches and present an MDP based optimization framework to determine dynamically the optimal delegation policy. Since most of the IEEE standards supporting mmWave directional MAC protocols (e.g., [72], [74]) operate using discrete time-slots which are time-synchronized and repetitive in nature, they also have more or less similar frame structures and follow an analogous mode of operation. Hence, in our subsequent discussions, we will refer to the IEEE 802.15.3c standard [72].

In reference to the network architecture of Fig. 3.1, we consider a mmWave wireless personal area network (WPAN) which is also referred as a Piconet. The piconet is controlled by a piconet controller

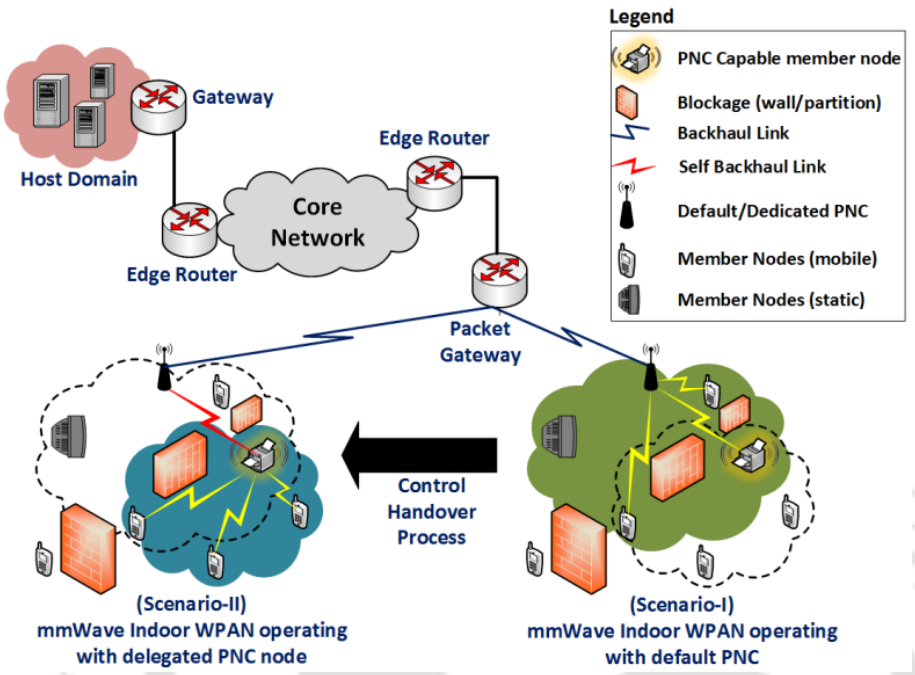

Figure 3.1: Network Architecture for a mmWave indoor WPAN;

(PNC), which is similar to an access point (AP) in WiFi networks. The PNC, as well as the other member nodes (DEVs) within the piconet, operate under blockage prone conditions and communicate using directional beams to compensate for high propagation losses. The PNC regulates various link-layer operations within the piconet in accordance with [72] and supports a variety of high data-rate indoor use-case scenarios as discussed in [82]. Under this standard, control delegation is implemented using the process of PNC Handover as explained in [72].

As shown in Fig. 3.1(Scenario-I), the default PNC controls the operations of the piconet under normal conditions. However, in blockage-prone scenarios, if the default PNC's visibility over the network nodes (DEVs) gets affected, then it may choose to relinquish its administrative controls to another PNC capable DEV having better network visibility as shown in Scenario-II(Fig. 3.1). By doing so, the PNC node virtually repositions itself to a better operating position and alleviates the impact of beam-blockage. In this scenario (Scenario-II), the link connecting the delegated and the default PNC (also known as *self-backhaul link*) plays an essential role in maintaining connectivity with the packet gateway and to the rest of the network. In our DCD technique, the default PNC is made to invoke the ***PNC Handover*** process from time-to-time (depending on the blockage scenario of the network) and relinquish its administrative controls to different PNC capable member nodes in

the system. As a result, the piconet is controlled through different delegated nodes at different points of time whereas the position of the default PNC remains unchanged. This approach of dynamically changing the PNC location is also in line with another study [57], where Genc *et al.* have shown that the positioning of the AP node can have a significant impact in reducing the outage probability of the connected member nodes. Moreover, as the ***PNC Handover*** process can be executed over a very short time span (in the order of milliseconds), the radio-visibility of the PNC node can be improved almost instantly even with dynamically changing blockages in the network.

3.2.1 Static Policy based DCD Approaches

The ability of the DCD approach to mitigate beam blockage mainly depends on the selection of the delegation node. Therefore, the task of identifying a good PNC capable node for control delegation is important. However, not all member nodes within the piconet can be considered for control delegation. To be able to operate as a delegated PNC, a member node must possess some special privileges e.g., alternate source of power, sufficient system memory, ability to generate group-keys etc. and the set of all such member nodes are known as PNC capable or *delegable nodes*. In the IEEE standard [72], a list of all such device privileges along with their respective priorities have been provided to help identify an appropriate delegable node. To evaluate the effectiveness of such parameter-based or rule-based delegation policies, we have proposed two different techniques viz. *Maximally Connected Neighbour Approach* and *Maximally Stable Neighbour Approach* for identification of a prospective delegable node.

To describe these approaches, we consider a network model as in Fig. 3.1, and assume that the piconet has N member nodes in which the individual DEVs are denoted using n where $n = 1, .., N$. The set of PNC-capable DEVs in the piconet are denoted using set $\mathcal{D}$ and the individual elements in $\mathcal{D}$ are denoted using d_i, where $i = 1, .., |\mathcal{D}|$ and $|\mathcal{D}| \leq N$. Hence, $\mathcal{D}$ denotes the collection of all DEV nodes to which the default PNC can possibly relinquish its controls. Since beam blockage can impact the quality of a mmWave link to different extents, in [14], Akdeniz *et al.* have used extensive street level measurement campaigns over urban micro-cellular environments to classify links into LoS, NLoS and Outage states and derived their transition probabilities as a function of the distance separating any two communicating nodes. Moreover, as the extent of beam-blockage in any of these links can vary with time, we use the variable t to denote the reference superframe (SF) while denoting the link-state $l_{src,dst}(t)$ between an arbitrary source node (src) and a destination node (dst). Based on this model, the proposed algorithms determine the next delegable node as described next.

3.2.1.1 Maximally Connected Neighbour Approach

This approach is mainly targeted for scenarios in which most of the DEVs in the piconet are static and the states of the node-to-node links do not change with time. Here, the default PNC (i.e., node P) uses Algorithm 1 to select a delegable node from the set $\mathcal{D}$ in such a way that it is radio-visible with respect to a maximum number of DEVs in the piconet. As a result, irrespective of the blockage scenario of the network, the piconet would always be controlled by a PNC having connectivity with a maximum number of DEVs.

The delegation approach in Algorithm 1 is executed in two different stages. In the first stage, the default PNC ascertains the link-states of all DEVs from set $\mathcal{D}$. Assuming that the number of nodes from $\mathcal{D}$ which are in LoS-state with respect to the default PNC P are denoted by $\tilde{\mathcal{D}}$ such that $\tilde{\mathcal{D}} \subset \mathcal{D}$, the default PNC probes the channel conditions for each of its tier-1 PNC capable nodes and determines the elements of set $\tilde{\mathcal{D}}$. To know the status of different nodes, their channel conditions or to get some specific information elements (IEs) from any node within the piconet, the IEEE 802.15.3c standard [72] provides provisions for a number of commands e.g., *Probe request command*, *PNC information request command*, *Remote scan request command* and *Channel status request command*. The details of these provisions are discussed in [72].

Since, the piconet is envisaged to operate in indoor coverage areas, all inter-node distances (and hence their link lengths) are assumed to span only over a small range of values. Hence, it is assumed that every LoS link has an identical capacity irrespective of its length, and a weightage of unity is assigned to all such links. Thus, if an arbitrary node n connects the default PNC P through an LoS link, the corresponding link $l_{n,P}(t)$ is assigned a utility value $U(l_{n,P}(t)) = 1$ and for any other link states, a utility value of $U(l_{n,P}(t)) = 0$ is assigned. Under this approach, since node-positions and the corresponding node-to-node links are assumed to be time invariant, we denote the utility of links $l_{n,P}$ simply using $U(l_{n,P})$. Thus, the total number of LoS connected DEVs that are present in the vicinity of the default PNC P is denoted by a score N_{T1} where $N_{T1} = \sum_{n=1}^{N} U(l_{n,P})$. Thereafter, in the second stage of the approach, the default PNC instructs each of the delegable nodes in set $\tilde{\mathcal{D}}$ to do neighbour discovery of their own (as per the provisions in [72]). In response, every PNC capable node $\tilde{d}_i \in \tilde{\mathcal{D}}$ ascertains the link-state of its peer nodes and comes up with a score $N_{T2}(\tilde{d}_i)$ which is similar to the score N_{T1} (in reference to P). Afterward, all such scores are communicated to the default PNC where they are compared with respect to N_{T1} and finally the $\tilde{d}_i$ corresponding to maximum $N_{T2}(\tilde{d}_i)$

Algorithm 1: Maximally Connected Neighbour Approach for DCD

Input: Set of DEVs N, Set of PNC capable nodes D, Link state matrix;

Initialize $N_{T1} = 0$ and $N_{T2}(\tilde{d}_i) = 0 \; \forall \tilde{d}_i \in \widetilde{D}$
procedure: UPDATE SCORE N_{T1} **AND SET** $\tilde{\mathcal{D}}$
for *each* $n \in N$ **do**
    determine link state $l_{n,P}$
    if $l_{n,P} = LoS$ **then**
        Set $U(l_{n,P}) = 1$
        Update $N_{T1} \leftarrow N_{T1} + 1$
        if $n \in \mathcal{D}$ **then**
            Update n into set $\tilde{\mathcal{D}}$
    else
        Set $U(l_{n,P}) = 0$
        go-to step-3
end procedure
procedure: UPDATE SCORE $N_{T2}(\tilde{d}_i)$
for $\tilde{d}_i \in \widetilde{D}$ **do**
    for *each* $n \in N$ **do**
        determine link state $l_{n,\tilde{d}_i}$
        if $l_{n,\tilde{d}_i} = LoS$ **then**
            Set $U(l_{n,\tilde{d}_i}) = 1$
            $N_{T2}(\tilde{d}_i) \leftarrow N_{T2}(\tilde{d}_i) + 1$
        else
            Set $U(l_{n,\tilde{d}_i}) = 0$
            go-to step-16
end procedure
Find Max$(N_{T2}(\tilde{d}_i))$
if $N_{T1} >= max(N_{T2}(\tilde{d}_i)$ **then**
    Keep piconet controls with default PNC
else
    Find $\arg\max_{\tilde{d}_i} \left[\left(N_{T2}(\tilde{d}_i)\right)\right]$
    Delegate piconet control to $\tilde{d}_i$

is selected for delegation.

3.2.1.2 Maximally Stable Neighbour Approach

This type of approach is mainly intended for scenarios with mobile users. Since user mobility within indoor conditions can significantly impact the outage probability of the connected nodes, the static-scenario based blockage mitigation approaches are not effective where the some or all the nodes have significant mobility. In this case, the default PNC uses Algorithm 2 to ensure that the delegated PNC is connected by a reliable self-backhaul link and also has improved visibility over the network nodes.

Using this approach (Algorithm 2), the default PNC first evaluates the blockage scenario in its vicinity and calculates the average number of LoS connected tier-1 nodes $Avg(N_{T1}(t))$ in its neighbourhood over an observation period of T msec (chosen heuristically). Thereafter, it updates the set of all delegable nodes which are connected to it through LoS links into the set $\tilde{\mathcal{D}}$ and instructs them to undertake neighbourhood discovery of their own.

Remark: Since nodes are assumed to be mobile under this approach, the state of the corresponding node-to-node links are considered to vary with time. Therefore, we use a variable (t) to denote the SF of reference [72].

In the next stage of the approach, each of the delegable nodes $\tilde{d}_i \in \tilde{\mathcal{D}}$ evaluates the link state of its peer nodes (i.e., tier-2 DEVs w.r.t node P) over the duration of T msec to determine the average number of connected neighbours $Avg(N_{T2}(\tilde{d}_i, t))$. Thereafter, depending on the co-ordinates of each of these nodes $\tilde{d}_i$, the default PNC evaluates its angular separation $\theta_{\tilde{d}_i}$ with respect to its nearest obstacle. For this, we assume the following:

(i) The default PNC operates using highly directional beams and is aware of the sector in which the delegable nodes are located

(ii) The obstacles are static objects of rectangular shape having random dimensions (length, breadth) ranging from 0-2 meters to denote indoor articles.

(iii) The default PNC is aware of the sectors in which the obstacle edges are positioned.

In case the delegable node $\tilde{d}_i$ is mobile, then the default PNC also calculates the expected change in its angular location $E[\Delta\theta_{\tilde{d}_i}]$ over the observation period T. Then, based on the values of parameters

Algorithm 2: Maximally Stable Neighbour Approach for DCD

Input: Set of DEVs N, Set of PNC capable nodes D, Training period T

Initialize $N_{T1} = 0$ and $N_{T2}(\tilde{d}_i) = 0 \ \forall \tilde{d}_i \in \widetilde{D}$
procedure: FIND SCORE $Avg(N_{T1}(t))$ **AND SET** $\tilde{\mathcal{D}}$
for *each* $n \in N$ **do**
    for *each SF* t *in training period* T **do**
        Calculate $N_{T1}(t)$ (as in Algorithm-1)
    Calculate $Avg(N_{T1}(t))$ over T samples
    if $n \in \mathcal{D}$ **then**
        Update n into set $\tilde{\mathcal{D}}$
end procedure
procedure: FIND SCORE $Avg(N_{T2}(\tilde{d}_i, t))$
for *each* $\tilde{d}_i \in \widetilde{D}$ **do**
    for *each SF* t *in training period* T **do**
        Calculate $N_{T2}(\tilde{d}_i, t)$ (as in Algorithm-1)
    Evaluate $Avg(N_{T2}(\tilde{d}_i, t))$ over T samples
    Calculate $(T_{\tilde{d}_i})$ w.r.t link $l_{\tilde{d}_i,P}$
    Calculate $(L_{\tilde{d}_i})$ w.r.t link $l_{\tilde{d}_i,P}$
    Evaluate parameter $Score(\tilde{d}_i) = T_{\tilde{d}_i} * L_{\tilde{d}_i}$
end procedure
Find $max[Avg(N_{T2}(\tilde{d}_i, t))]$
if $Avg(N_{T1}(t)) >= max[Avg(N_{T2}(\tilde{d}_i, t))]$ **then**
    Keep piconet controls with default PNC
else
    Find $\arg\max_{\tilde{d}_i} \Big(Score(\tilde{d}_i) \Big)$
    Delegate piconet control to $\tilde{d}_i$

$E[\Delta\theta_{\tilde{d}_i}]$ and $(\theta_{\tilde{d}_i})$, the average time required for a self-backhaul link $l_{\tilde{d}_i,P}$ to get blocked is evaluated for each of the delegable nodes and denoted using a parameter $T_{\tilde{d}_i}$ where

$$T_{\tilde{d}_i} = \frac{\theta_{\tilde{d}_i}}{E[\Delta\theta_{\tilde{d}_i}]} \tag{3.1}$$

Since, the self-backhaul link $l_{\tilde{d}_i,P}$ can also be blocked due to the mobility of the other nodes within the piconet, the default PNC calculates the average temporal consistency $(L_{\tilde{d}_i})$ of each of the self-backhaul links $l_{\tilde{d}_i,P}$ over the training duration T. Here, $(L_{\tilde{d}_i})$ is defined as

$$L_{\tilde{d}_i} = \frac{\sum_t \mathbb{1}_{\tilde{d}_i,P}(t)}{T} \tag{3.2}$$

where $\mathbb{1}_{\tilde{d}_i,P}(t)$ is an indicator function defined by:

$$\mathbb{1}_{\tilde{d}_i,P}(t) = \begin{cases} 1, & \text{if link } l_{\tilde{d}_i,P} \text{ is in LoS state in SF (t)} \\ 0, & \text{otherwise} \end{cases} \tag{3.3}$$

Based on the values of the average time to blockage $(T_{\tilde{d}_i})$ and average link consistency $(L_{\tilde{d}_i})$ obtained, a score $Score(\tilde{d}_i)$ is generated in (3.4) to denote the stability of the self-backhaul link $\mathbb{1}_{\tilde{d}_i,P}$

$$Score(\tilde{d}_i) = T_{\tilde{d}_i} * L_{\tilde{d}_i} \tag{3.4}$$

Finally, to identify a prospective delegable node, the default PNC compares its network visibility score (i.e., $Avg(N_{T1}(t))$ with respect to the scores $Avg(N_{T2}(\tilde{d}_i, t))$ in each of the delegable nodes $\tilde{d}_i$. If any of the delegable node(s) $\tilde{d}_i$ offers better network visibility than that of the default PNC, then the piconet's control is delegated to the node with the most stable self-backhaul link (i.e., corresponding to node $\tilde{d}_i$ having maximum $(Score(\tilde{d}_i))$. Otherwise, in all other scenarios, the default PNC retains control of the piconet.

3.2.1.3 Limitations of Static Policy based DCD Approaches

Although, the static policy-based DCD approaches allow mmWave piconets to operate more effectively under blockage-prone environments, they fail to operate optimally under practical conditions as network conditions can change continuously under real-world scenarios. Such changes may arise because of beam-blockage as discussed below:

(i) The association of DEV nodes with respect to the PNC may change with time. This may be caused, either due to node mobility (in which case, the DEV will eventually undergo connection

handover) or due to blockage of the corresponding PNC-DEV link. In either case, the visibility of the piconet with respect to the default PNC and the other delegable nodes may get changed

(ii) The traffic associated with each of the DEV nodes may vary with time. It may either be due to inherent changes in the transmission requirements of the DEV nodes or due to sudden changes in the quality of the relevant DEV-PNC link. As a result, the total load associated with the default PNC and the delegable nodes may vary with time.

(iii) If the piconet is controlled by a delegated PNC, then sudden outages or deterioration in the state of a self-backhaul link can also block or restrict traffic from the whole piconet.

In these cases, any delegation policy based on a fixed set of rules will eventually perform sub-optimally. Hence, to address these issues and to enable the default PNC take optimal delegation decisions, a dynamic decision-making framework would be required. Since, the IEEE 802.15.3c standard [72] operates through periodically repeated discrete-time slots where all piconet operations are time-synchronized, we use a discrete-time Markov decision process (DT-MDP) model to formulate a control delegation process to tackle this issue.

3.2.2 DT-MDP Framework for Determination of Optimal Delegation Policy

To be able to effectively employ the DCD technique under dynamically evolving network scenarios, we use a DT-MDP framework and build an optimization model around it. This allows the default PNC to determine the optimal delegation policy under a given network scenario and enables it to identify the ideal node for delegating its controls. To describe this model, we have used the notations and nomenclature as in [83]. The generalized representation for the MDP model is given using parameters $\{\mathbb{T}, S, A_s, p(.|s,a), r(.|s,a)\}$ where, $\mathbb{T}$ denotes the set of decision epochs; S, the set of system states; A_s, the action-set as applicable over the set of states; $p(.|s,a)$, the set of state-transition probabilities which is a function of the system state s and the corresponding action a; and $r(.|s,a)$ the set of rewards. For the problem of control delegation, these parameters are formulated as follows:

Decision Epoch ($\mathbb{T}$): These refer to intervals in the default PNC's life-span in which it has to take control delegation decisions. Due to the slotted mode of operation within a piconet, the default PNC can take delegation decisions only at the end of each SF. Therefore, the collection of all such decision epochs is denoted using a discrete time variable $\mathbb{T}$, where individual elements in $\mathbb{T}$ are denoted using t to signify the reference SF. Depending on the life-time of PNC operation, the set

$\mathbb{T}$ can span over a finite or infinite horizon. Accordingly, in conformance with [83], $\mathbb{T}$ is defined as $\mathbb{T} = \{1, .., M\}\, \forall M \leq \infty$.

Although, every SF can act as a decision epoch for the PNC, the actual delegation decisions are taken much less frequently. This is due to the fact that the state of the network changes relatively slowly in comparison to the duration of a typical SF. Moreover, as long as the piconet is controlled by a delegated PNC, the default PNC behaves as an ordinary DEV node and does not need to take delegation decisions.

State space (S): During each decision epoch, the piconet operates in a particular state and the collection of all such system states forms the state-space (S) of the network. For the problem of control delegation, a piconet can be operated either by the default PNC (P) or by any of the delegable nodes (from set $\mathcal{D}$). Therefore, the selection of a PNC node to control the piconet will depend mainly on its visibility with respect to the member DEVs. As the default PNC continues to delegate its controls and operate through the delegable nodes, a different set of DEVs may get serviced in each epoch.

Referring to the network structure in Fig. 3.1, we assume that each DEV is associated with up to K types of data-traffic. Additionally, let $n_{d_i}^k$ denote the number of DEVs with traffic-type k (where $k = 1, .., K$), which can be serviced by a delegable node $d_i \in \mathcal{D}$ in such a way that their transmission requirements can be satisfied by the available link quality. In a similar way, let n_P^k denote the number of DEVs of traffic type k which can be serviced by the default PNC. Thus, an arbitrary system comprising of a delegable node d_i and the set of all its serviceable DEVs can be expressed using $(n_{d_i}^1, n_{d_i}^2, ..., n_{d_i}^k, l_{d_i,P})$. Here, $l_{d_i,P}$ denotes the state of the self-backhaul link connecting the default and the delegated PNC d_i. However, when we consider a system of DEVs which can be serviced by the default PNC P, the link $l_{d_i,P}$ is no longer required and can be considered to be unity by default. Therefore, the corresponding state of the system can be represented simply using $(n_{d_i}^1, n_{d_i}^2, ..., n_{d_i}^k, 1)$. Considering the overall state of the piconet (comprising of all the PNC capable nodes and their corresponding sets of serviceable DEVs), the relevant expression for system state s_i is given by

$$s_i = \left\{ \left(n_P^1, n_P^2, ..., n_P^k, 1 \right), .., \left(n_{d_i}^1, n_{d_i}^2, ..., n_{d_i}^k, l_{d_i,P} \right) \right\} \tag{3.5}$$

Finally, the state-space (S) of the system, which is the collection of all possible system states $s_i \in S$, is denoted as

$$S = \bigcup\nolimits_{i \in |S|} s_i \tag{3.6}$$

Set of actions A_s: This is defined as the set of all permissible actions among all the system states. In our control delegation model, each state of the piconet is controlled by a PNC where it has to select a specific delegation action from a collection of feasible actions. If the piconet is operating in an arbitrary system state s_i and is being controlled by the default PNC (P) then the PNC may either choose to retain its controls in the next decision epoch or may delegate its controls to any of the nodes $d_i \in \mathcal{D}$. Accordingly, the set of actions is defined as -

$$A_s = \begin{cases} a_P & \text{Retain control at default PNC P} \\ a_{d_1} & \text{Shift control to 1}^{\text{st}} \text{ delegation node (d}_1\text{)} \\ .. & .. \\ a_{d_i} & \text{Shift control to i}^{\text{th}} \text{ delegation node (d}_\text{i}\text{)} \end{cases} \tag{3.7}$$

Considering the above definition with respect to the specific network model of Fig. 3.1, where there is only one delegable node other than the default PNC, we can drop the sub-script i from d_i and denote the corresponding action set as $A_s = \{a_P, a_d\}$.

State transition dynamics: To model the dynamics of state-transitions in our system, we refer to Fig. 3.2. This shows a simplified scenario within a piconet where there is only one delegable node (d) other than the default PNC (P). In addition, we assume that all the DEVs within the piconet generate only one type of traffic. This can also be considered analogous to a Constant Bit Rate (CBR) traffic, which can be representative of a file download process from a remote server. Using the state definition nomenclature as discussed earlier, we define the state of the piconet using $\{(n_P, 1), (n_d, l_{d,P})\}$ or simply $\{(n_P), (n_d, l_{d,P})\}$. Here n_P and n_d denote the number of DEV nodes that can be serviced by the PNC P and d respectively. By following this convention, a piconet will undergo state-transitions under any of the following conditions.

(i) The state of the self-backhaul link $l_{d,P}$ connecting the delegation node d and the default PNC P gets changed.

(ii) The number of transmitting DEVs which can be serviced by the PNC (i.e., $\{n_P, n_d\}$) gets changed.

Since these two factors are independent of each another, we develop separate models to analyze the influence of each of them on the overall state-transition behavior of the piconet. Moreover, with regard to the second factor, the parameter $\{n_P, n_d\}$ is also indicative of the total traffic attached to the PNCs.

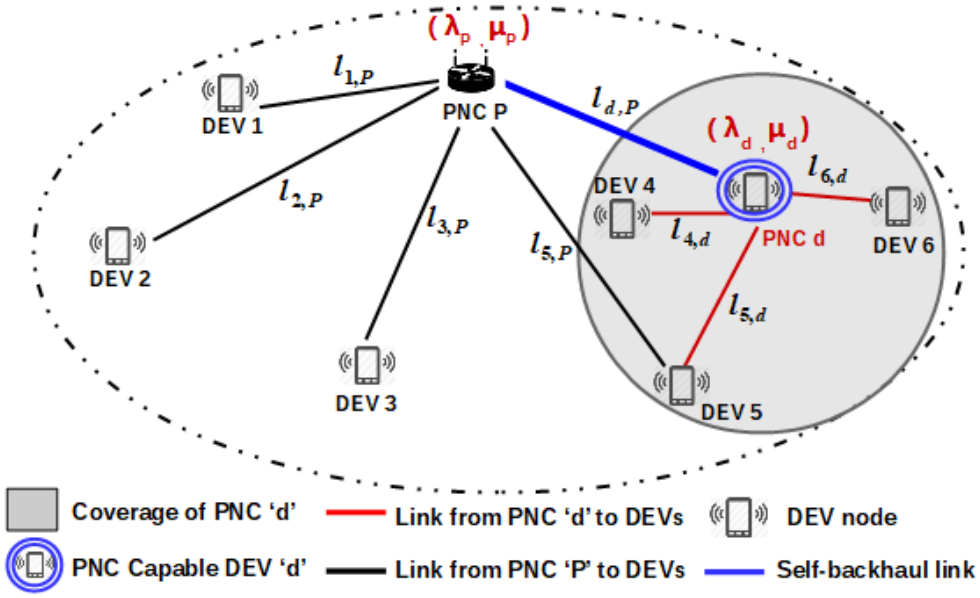

Figure 3.2: Network structure within a piconet, depicting links that connect the DEV nodes with the default and delegated PNCs

3.2.2.1 State Transitions Due to Changes in the State of the Self-Backhaul Link

As self-backhaul links are generally used to connect outdoor and the indoor environments, the dynamics of their state transitions are mostly influenced by their deployment scenario (e.g., indoor residential, industrial, airports etc.). In addition, the extent of changes in these links are also influenced by other factors like the density and the type of obstacles within the deployment scenario. Therefore, to build a realistic channel model while considering all these factors, we refer to the statistical model in [14]. It is based on extensive trials in urban-microcellular environments and categorizes links into LoS, NLoS and Outage states, respectively. As discussed earlier (in Section 3.2.1), this model depends on the probabilities of state-transitions between the three link-states as a function of the distance of separation (x) between pairs of communicating nodes. For example, if a DEV is located at a distance of x meters from the PNC node, its corresponding link-state probabilities are -

$$\left.\begin{aligned} p_{out}(x) &= \max(0, 1 - e^{-a_{out}x + b_{out}}) \\ p_{LoS}(x) &= (1 - p_{out}(x))e^{-a_{LoS}x} \\ p_{NLoS}(x) &= 1 - p_{LoS}(x) - p_{out}(x) \end{aligned}\right\} \tag{3.8}$$

In the above, the variables a_{out}, b_{out} and a_{LoS} are system design parameters and are dependent on the operating environment of the piconet. For a network using this channel model with random node deployments over a coverage range of 200 meters, Mezzavilla *et al.* [68] calculated the steady-state probabilities of each of these states and derived their corresponding transition probabilities. In our further analysis, we refer to these values and denote the corresponding set of state-transition probabilities using $\mathbf{P^{CH}}$ where the individual elements in $\mathbf{P^{CH}}$ are expressed as:

$$\mathbf{P^{CH}} = \begin{bmatrix} p^{CH}(L \to L) & p^{CH}(L \to N) & p^{CH}(L \to O) \\ p^{CH}(N \to L) & p^{CH}(N \to N) & p^{CH}(N \to O) \\ p^{CH}(O \to L) & p^{CH}(O \to N) & p^{CH}(O \to O) \end{bmatrix} \tag{3.9}$$

In (3.9), the notation *'CH'* is used to indicate the dynamics of channel-state variation in the self-backhaul link (i.e., the link $l_{d,P}$ as in Fig. 3.2). Since, the self-backhaul link is required to carry the overall traffic from all the connected DEVs to the packet gateway, it should always be able to support high data-rates. However, in our referenced channel model of [14], the NLoS state may not have sufficient SNR to support high traffic intensities. Therefore, we introduce a simplified bi-state channel model consisting of only the LoS state (L) and a newly defined Outage state (O') as shown in Fig. 3.3. The state-transition probabilities of this model are denoted using the matrix $\widetilde{\mathbf{P}}^{\mathbf{CH}}$ of (3.10).

$$\tilde{\mathbf{P}}^{\mathbf{CH}} = \begin{bmatrix} \tilde{p}^{CH}(L \to L) & \tilde{p}^{CH}(L \to O') \\ \tilde{p}^{CH}(O' \to L) & \tilde{p}^{CH}(O' \to O') \end{bmatrix} \tag{3.10}$$

Based on the values of state-transition probabilities in (3.9), the relation between the elements of matrices $\mathbf{P^{CH}}$ and $\widetilde{\mathbf{P}}^{\mathbf{CH}}$ are expressed as:

$$\begin{aligned} \tilde{p}^{CH}(L \to L) &= p^{CH}(L \to L) \\ \tilde{p}^{CH}(L \to O') &= p^{CH}(L \to O) + p^{CH}(L \to N) \\ \tilde{p}^{CH}(O' \to L) &= p^{CH}(O \to L) + p^{CH}(N \to L) \\ \tilde{p}^{CH}(O' \to O') &= 1 - \tilde{p}^{CH}(O' \to L) \end{aligned} \tag{3.11}$$

Thus, for any arbitrary self-backhaul link $l_{d,P}$ connecting a delegated PNC d and the default PNC P, the variations of its link-states follow an IID process with the common transition probabilities given in $\widetilde{\mathbf{P}}^{\mathbf{CH}}$.

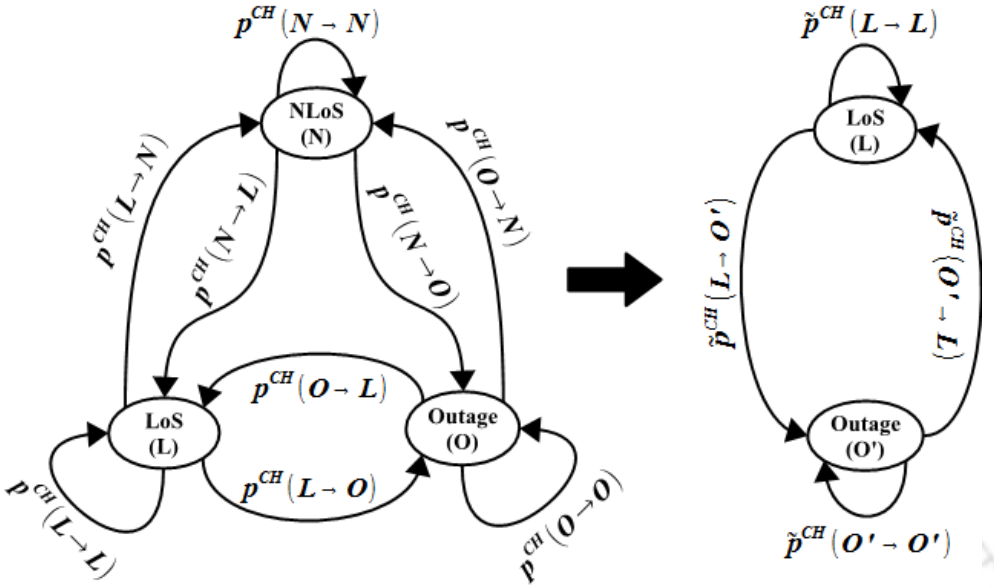

Figure 3.3: Relationship between the state-transition probabilities of the statistical model in [14] and the derived bi-state channel model for the self-backhaul links.

3.2.2.2 State Transitions Due to Changes in PNC Load

To model the dynamics of state-changes that are caused due to changes in the PNC load, we refer to a simplified piconet model (as in Fig. 3.2) and consider the various factors that may influence load-level changes at the two PNCs i.e., $\{n_P, n_d\}$. Accordingly, the piconet's load-state may change due to any of the following factors:

(i) Due to the movement of DEVs or obstacles within a piconet, the visibility of nodes with respect to a PNC may change and nodes blocked earlier due to beam blockage may become visible to the PNC and vice-versa. This will then cause a net addition or reduction in the total number of DEVs that can be serviced by a PNC.

(ii) Due to node mobility, a DEV may move away from the coverage of its existing PNC and come under the coverage range of another PNC. In this case, the DEV node gets eventually dissociated from the PNC to which it was previously attached and gets associated to a new PNC.

It may be noted that both the above effects arise from node mobility. The first one leads to either an association or a disassociation of a DEV node with respect to a PNC. However, the state changes triggered due to the second factor, lead to pairs of association-dissociation events taking place at the same time. For this reason, the state-transitions caused due to the first factor are referred to as

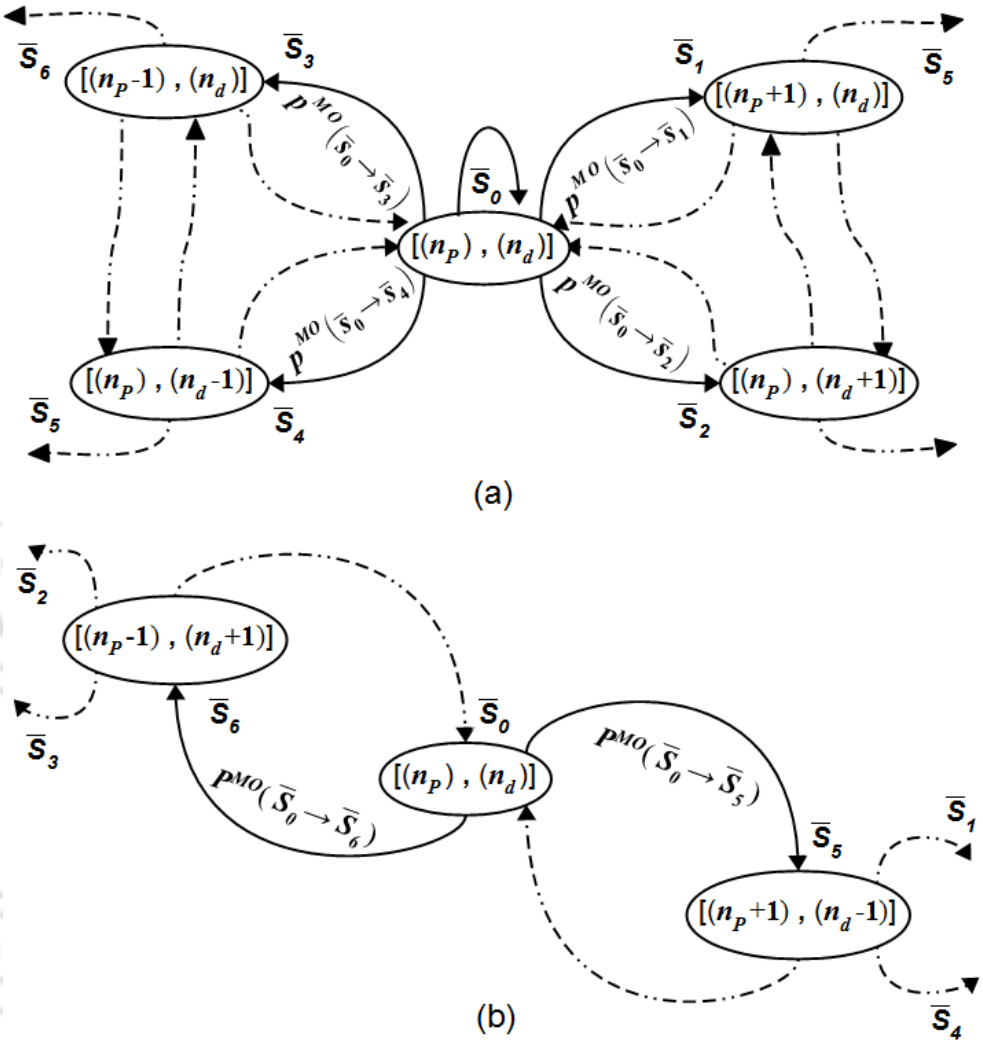

Figure 3.4: Dynamics of mobility induced state transitions in a piconet where the system state is defined only using n_P and n_d. (a) Dynamics of elementary state transitions. (b) Dynamics of combined state transitions.

elementary state-transitions and while those caused by the second factor are called *combined state-transitions*.

With reference to a piconet's current load-state $\{n_P, n_d\}$ (which is denoted using $\bar{s}_0$) and any subsequent load-state $\bar{s}_i$, we depict the set of all possible mobility-induced state-transitions along with their corresponding probabilities $p^{MO}(\bar{s}_0 \to \bar{s}_i)$ in Fig. 3.4. Here, Fig. 3.4(a) depicts the set of all elementary state-transitions in which any of the PNC loads (i.e., n_P or n_d) can increment or decrement by one in a given SF. In this case, with respect to the piconet's current load-state $\bar{s}_0$, the system can transition to any of the following states: (a) load-state $\{(n_P + 1), (n_d)\}$ corresponding to the state-transition $(\bar{s}_0 \to \bar{s}_1)$; (b) load-state $\{(n_P - 1), (n_d)\}$ corresponding to the state-transition

$(\bar{s}_0 \rightarrow \bar{s}_3)$; (c) load state $\{(n_P), (n_d + 1)\}$ corresponding to the state transition $(\bar{s}_0 \rightarrow \bar{s}_2)$; and (d) load-state $\{(n_P), (n_d - 1)\}$ corresponding to the state transition $(\bar{s}_0 \rightarrow \bar{s}_4)$. Similarly, for the set of all combined state-transitions (Fig. 3.4(b)), the reference state $(\bar{s}_0)$ of the piconet can transition to any of the following load-states: (a) state $\{(n_P + 1), (n_d - 1)\}$ corresponding to the state transition $(\bar{s}_0 \rightarrow \bar{s}_5)$; or (b) state $\{(n_P - 1), (n_d + 1)\}$ corresponding to the state transition $(\bar{s}_0 \rightarrow \bar{s}_6)$.

The process whereby previously blocked DEVs become visible with respect to a PNC and get associated to it, can be considered as similar to the process for arrival of new nodes in a piconet. Therefore, we model this as a Poisson process in which the inter-arrival times are exponentially distributed with parameter λ. In a similar way, the process for disassociation of DEVs with respect to a PNC due to beam-blockage can be considered as analogous to the process of node departure from a piconet. Therefore, here as well, we model it as another Poisson process in which the inter-departure times are exponentially distributed with parameter μ. Hence, considering all the DEVs in the piconet that are serviceable either by node P or d, we introduce parameters (λ_P, λ_d) and (μ_P, μ_d) to indicate their mean rate of association and dissociation with respect to the PNCs. Additionally, for the DEVs that can be serviced by the PNC P, we denote the time required for the next association or disassociation event using the parameters $T_{arr}(P)$ and $T_{dep}(P)$ respectively. Similarly, for the DEVs that are serviceable by the PNC d, we introduce parameters $T_{arr}(d)$ and $T_{dep}(d)$. The duration for which the load-state of the system remains unchanged (i.e., no DEV association or disassociation event occurs in either of the PNCs) is given by the random variable T_{static}

$$T_{static} = \min\left(T_{arr}(P), T_{dep}(P), T_{arr}(d), T_{dep}(d)\right) \tag{3.12}$$

with the distribution

$$\begin{aligned} &P\left(T_{static} > t\right) \\ &\quad = P(\min\left(T_{arr}(P), T_{dep}(P), T_{arr}(d), T_{dep}(d)\right) > t) \\ &\quad = e^{-\lambda_P t} * e^{-\mu_P t} * e^{-\lambda_d t} * e^{-\mu_d t} \\ &\quad = e^{-(\lambda_P + \mu_P + \lambda_d + \mu_d)t} \end{aligned} \tag{3.13}$$

Here T_{static} is a function of the variables λ_P, μ_P, λ_d and μ_d and is exponentially distributed with mean $(\lambda_P + \mu_P + \lambda_d + \mu_d)$. This is then also the mean duration for which the default PNC can delegate its controls.

With reference to the load-state $\bar{s}_0$ in Fig. 3.4, if a blocked DEV node becomes visible to the PNC

P, the number of its serviceable DEVs will change from $n_P \rightarrow (n_P + 1)$. This can either lead to the state-transition $(\bar{s}_0 \rightarrow \bar{s}_1)$ in Fig. 3.4(a) (i.e., from load-state $\{(n_P), (n_d)\}$ to $\{(n_P + 1), (n_d)\}$), or can contribute towards a combined state transition $(\bar{s}_0 \rightarrow \bar{s}_5)$ as in Fig. 3.4(b) (i.e., from load-state $\{(n_P), (n_d)\}$ to $\{(n_P + 1), (n_d - 1)\}$). Hence, using (3.13), the probability that a DEV node will get associated to PNC P is given as $P(T_{arr}(P) < T_{static}) = \frac{\lambda_P}{(\lambda_P+\mu_P+\lambda_d+\mu_d)}$. However, as these node association events can contribute equally towards the state transitions $(\bar{s}_0 \rightarrow \bar{s}_1)$ and $(\bar{s}_0 \rightarrow \bar{s}_5)$, the probability of the mobility induced elementary state-transition $(\bar{s}_0 \rightarrow \bar{s}_1)$ is given by $p^{MO}(\bar{s}_0 \rightarrow \bar{s}_1) = \frac{\lambda_P}{2(\lambda_P+\mu_P+\lambda_d+\mu_d)}$. Similarly, for the PNC d, the probability of the load-state transition $(\bar{s}_0 \rightarrow \bar{s}_2)$ is given by $p^{MO}(\bar{s}_0 \rightarrow \bar{s}_2) = \frac{\lambda_d}{2(\lambda_P+\mu_P+\lambda_d+\mu_d)}$.

Similarly, for the process of node disassociations, the probability that an associated DEV gets blocked and loses its visibility with respect to the PNC P, can be derived using (3.13) and expressed as $P(T_{dep}(P) < T_{static}) = \frac{\mu_P}{(\lambda_P+\mu_P+\lambda_d+\mu_d)}$. With reference to Fig. 3.4, such disassociation events (i.e., $n_P \rightarrow (n_P - 1)$) can either lead to a state transition $(\bar{s}_0 \rightarrow \bar{s}_3)$ (i.e., from load-state $\{(n_P), (n_d)\}$ to $\{(n_P - 1), (n_d)\}$) as in Fig. 3.4(a), or can contribute towards a combined state transition $(\bar{s}_0 \rightarrow \bar{s}_6)$ as in Fig. 3.4(b) (i.e., from load-state $\{(n_P), (n_d)\}$ to $\{(n_P - 1), (n_d + 1)\}$). Since, both these types of state-transitions can contribute equally towards the node disassociation event, the probability of the state transition $(\bar{s}_0 \rightarrow \bar{s}_3)$ is $p^{MO}(\bar{s}_0 \rightarrow \bar{s}_3) = \frac{\mu_P}{2(\lambda_P+\mu_P+\lambda_d+\mu_d)}$. Similarly, the probability of node disassociation with respect to PNC d (i.e., state change $(\bar{s}_0 \rightarrow \bar{s}_4)$) will be given by $p^{MO}(\bar{s}_0 \rightarrow \bar{s}_4) = \frac{\mu_d}{2(\lambda_P+\mu_P+\lambda_d+\mu_d)}$.

It may be noted that the combined state-transitions i.e., $(\bar{s}_0 \rightarrow \bar{s}_5)$ and $(\bar{s}_0 \rightarrow \bar{s}_6)$ happen because of the simultaneous occurrence of elementary transitions $\{(\bar{s}_0 \rightarrow \bar{s}_1), (\bar{s}_0 \rightarrow \bar{s}_4)\}$ and $\{(\bar{s}_0 \rightarrow \bar{s}_2), (\bar{s}_0 \rightarrow \bar{s}_3)\}$ respectively. However, since all elementary state-transition events can be considered to be independent of each other, the probability of a combined state-transition event is calculated using the product of the constituent elementary state-transitions. Therefore, we calculate the probabilities of the combined state-transition events $(\bar{s}_0 \rightarrow \bar{s}_5)$ and $(\bar{s}_0 \rightarrow \bar{s}_6)$ using expressions $p^{MO}(\bar{s}_0 \rightarrow \bar{s}_5) = p^{MO}(\bar{s}_0 \rightarrow \bar{s}_1).p^{MO}(\bar{s}_0 \rightarrow \bar{s}_4)$ and $p^{MO}(\bar{s}_0 \rightarrow \bar{s}_6) = p^{MO}(\bar{s}_0 \rightarrow \bar{s}_2).p^{MO}(\bar{s}_0 \rightarrow \bar{s}_3)$ respectively. Finally, on obtaining the probabilities of all the elementary and combined state-transition events, the probability that the system remains in its original state is obtained by applying the normalization rule. Thus, the probabilities of various mobility induced state transition events $p^{MO}(j|i)$ are expressed as:

$$p^{MO}(j|i) = \begin{cases} 1 - \sum_{j=1}^{6} p^{MO}\left(\bar{s}_0 \rightarrow \bar{s}_j\right); & \mathrm{j} = \bar{\mathrm{s}}_0; \mathrm{i} = \bar{\mathrm{s}}_0; \\ \frac{\lambda_P}{2(\lambda_P+\mu_P+\lambda_d+\mu_d)}; & \mathrm{j} = \bar{\mathrm{s}}_1; \mathrm{i} = \bar{\mathrm{s}}_0; \\ \frac{\lambda_d}{2(\lambda_P+\mu_P+\lambda_d+\mu_d)}; & \mathrm{j} = \bar{\mathrm{s}}_2; \mathrm{i} = \bar{\mathrm{s}}_0; \\ \frac{\mu_P}{2(\lambda_P+\mu_P+\lambda_d+\mu_d)}; & \mathrm{j} = \bar{\mathrm{s}}_3; \mathrm{i} = \bar{\mathrm{s}}_0; \\ \frac{\mu_d}{2(\lambda_P+\mu_P+\lambda_d+\mu_d)}; & \mathrm{j} = \bar{\mathrm{s}}_4; \mathrm{i} = \bar{\mathrm{s}}_0; \\ \frac{\lambda_P\mu_d}{4(\lambda_P+\mu_P+\lambda_d+\mu_d)^2}; & \mathrm{j} = \bar{\mathrm{s}}_5; \mathrm{i} = \bar{\mathrm{s}}_0; \\ \frac{\lambda_d\mu_P}{4(\lambda_P+\mu_P+\lambda_d+\mu_d)^2}; & \mathrm{j} = \bar{\mathrm{s}}_6; \mathrm{i} = \bar{\mathrm{s}}_0; \end{cases} \tag{3.14}$$

3.2.2.3 State Transitions Model for the Combined System

In the previous subsections, we discussed models to capture the dynamics of state-transitions in the self-backhaul link $l_{d,P}$ (using (3.10), (3.11)) and obtained the behaviour of load-level changes due to mobility induced factors (in (3.14)). Subsequently, by using these models, we determined the parameters $\widetilde{\mathbf{P}}^{\mathbf{CH}}$ and $p^{MO}(\bar{s}_i|\bar{s}_0)$ respectively. On combining the two models, the collection of all state-changes for the overall system (in reference to an arbitrary system-state s_0 i.e., $\{(n_P), (n_d, l_{d,P} = L)\}$ are shown in Fig. 3.5. Here, since the two models are independent of each other, the state-transition probability matrix for the combined system model is given by the product of the individual transition probabilities of the constituent models. Thus, we represent the state-transition probabilities for the combined model (with reference to state s_0) and in the presence of various delegation actions) as in (3.15).

With regard to (3.15), the action set comprises of two permissible actions i.e., $\{a_P, a_d\}$. If the self-backhaul link $l_{d,P}$ gets under outage i.e., $(L \rightarrow O')$ then the PNC node cannot relinquish its controls to the delegation node d. Therefore, $\tilde{p}^{CH}(L \rightarrow O')$ is zero for all cases where $a = a_d$. In the remaining cases, the state-transition probability of the combined model is given by the product of the transition probabilities of the two constituent models.

With reference to a more generalized model of the piconet, where there are two delegation nodes $\{d_1, d_2\}$ and k traffic types, we can denote an arbitrary system state as $\left\{\left(n_P^1, .., n_P^k\right), \left(n_{d_1}^1, .., n_{d_1}^k, l_{d_1,P}\right), \left(n_{d_2}^1, .., n_{d_2}^k, l_{d_2,P}\right)\right\}$. To formulate such a system along the same lines of our earlier model, we proceed as follows. With respect to each PNC, the total traffic contributed by its serviceable nodes are summed up and represented in terms of an equivalent number of nodes of the base traffic class i.e., $k = 1$. In this way, the above generalized state-representation can be expressed as $\left\{\left(\tilde{n}_P^1\right), \left(\tilde{n}_{d_1}^1, l_{d_1,P}\right), \left(\tilde{n}_{d_2}^1, l_{d_2,P}\right)\right\}$

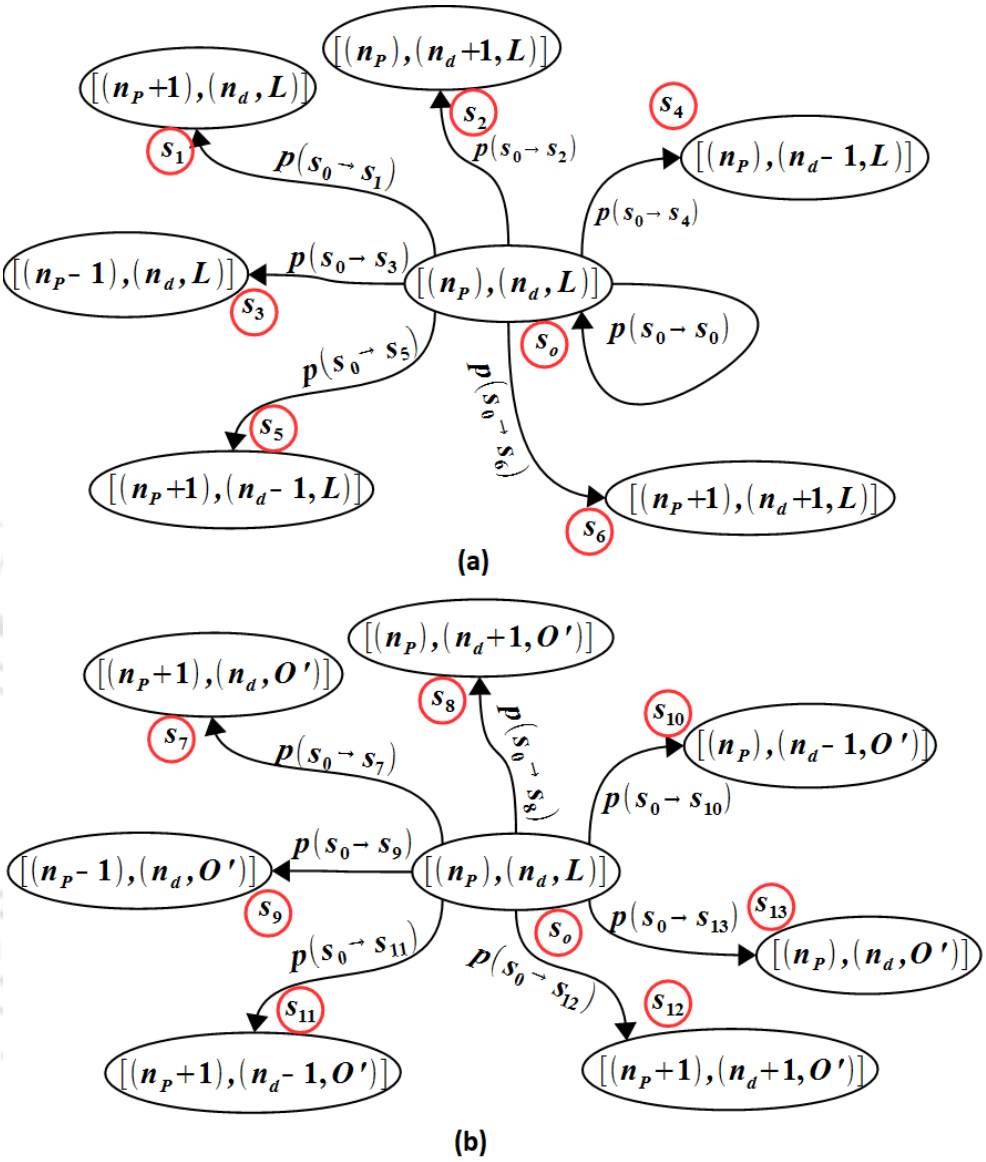

Figure 3.5: State transition dynamics for the combined system model with respect to a reference state $\{(n_P), (n_d, l_{dP} = L)\}$ (a) When state of the self-backhaul link remains the same (i.e., $l_{d,P} = L$) whereas n_P and n_d values are changed. (b) When all three state variables i.e., n_P,n_d and $l_{d,P}$ are changed

where $\tilde{n}_P^1$, $\tilde{n}_{d_1}^1$ denote the number of nodes of traffic type $k = 1$ which can generate the same amount of traffic as that generated by the set of nodes $(n_P^1, .., n_P^k)$, $(n_{d_1}^1, .., n_{d_1}^k)$ and $(n_{d_2}^1, .., n_{d_2}^k)$. We can then adopt the same approach as that followed by the simplified system model to derive the state transition probabilities.

$$p(j|i=s_0,a) = \begin{cases} p^{MO}(i\to j).\tilde{p}^{CH}(L\to L); & \mathrm{j}=\mathrm{s_0};\mathrm{a}=\{\mathrm{a_d},\mathrm{a_P}\}; \\ p^{MO}(i\to j).\tilde{p}^{CH}(L\to L); & \mathrm{j}=\mathrm{s_1};\mathrm{a}=\{\mathrm{a_d},\mathrm{a_P}\}; \\ p^{MO}(i\to j).\tilde{p}^{CH}(L\to L); & \mathrm{j}=\mathrm{s_2};\mathrm{a}=\{\mathrm{a_d},\mathrm{a_P}\}; \\ p^{MO}(i\to j).\tilde{p}^{CH}(L\to L); & \mathrm{j}=\mathrm{s_3};\mathrm{a}=\{\mathrm{a_d},\mathrm{a_P}\}; \\ p^{MO}(i\to j).\tilde{p}^{CH}(L\to L); & \mathrm{j}=\mathrm{s_4};\mathrm{a}=\{\mathrm{a_d},\mathrm{a_P}\}; \\ p^{MO}(i\to j).\tilde{p}^{CH}(L\to L); & \mathrm{j}=\mathrm{s_5};\mathrm{a}=\{\mathrm{a_d},\mathrm{a_P}\}; \\ p^{MO}(i\to j).\tilde{p}^{CH}(L\to L); & \mathrm{j}=\mathrm{s_6};\mathrm{a}=\{\mathrm{a_d},\mathrm{a_P}\}; \\ p^{MO}(i\to j).\tilde{p}^{CH}(L\to L); & \mathrm{j}=\mathrm{s_7},..,\mathrm{s_{13}};\mathrm{a}=\{\mathrm{a_P}\}; \\ 0 & \text{Otherwise} \end{cases} \tag{3.15}$$

3.2.2.4 Determination of State Transition Reward and Optimal Decision Policy

In any decision epoch when an action is taken based on the delegation policy (π), the decision-making entity (default PNC) receives a reward and the system transitions to the next state. For a state-transition between piconet states s_i and s_j in which an action $a \in A_s$ has been selected, the corresponding state-transition reward is denoted using a real valued function $r(s_j|s_i,a)$ and its expected value for the reference state s_i is given by -

$$r\left(s_i,a\right) = \sum_{s_j\in S} r(s_j|s_i,a).p(s_j|s_i,a) \tag{3.16}$$

In our delegation model, the reward function $r(.|.,a)$ is defined as follows:

$$r(s_j|s_i,a) = w_d f_d(s_j|s_i,a) + w_t f_t(s_j|s_i,a) + w_l f_l(s_j|s_i,a) \tag{3.17}$$

Here $f_d(s_j|s_i,a)$ is the reward component for the set of DEVs which become unserviceable because of the state transition. Similarly, $f_t(s_j|s_i,a)$ and $f_l(s_j|s_i,a)$ are the throughput and latency reward components for the state transition $(s_j|s_i,a)$. Each of these are linear in nature and their magnitudes are represented as percentages. The parameters, w_d, w_t and w_l are the weightages of the reward components $f_d(.)$, $f_t(.)$ and $f_l(.)$ respectively and their values are constrained by:

$$w_d + w_t + w_l = 1 \quad \forall 0 \le w_d \le 1; 0 \le w_t \le 1; 0 \le w_l \le 1; \tag{3.18}$$

In (3.18), the network operator assigns their values based on the relative importance of each of the reward components. By adjusting these parameters, the optimization policy can then be adapted to meet a variety of operational requirements. In (3.17), the reward component $f_d(.)$ is evaluated as-

$$f_d(s_j|s_i,a) = \left(1 - \frac{\zeta(s_j|s_i,a)}{\gamma(s_j)}\right) 100\% \tag{3.19}$$

Here, $\gamma(s_j)$ is the total throughput associated with the current system-state (s_i) and $\zeta(s_j|s_i,a)$ is the total throughput contributed by all such serviceable DEVs which will become unserviceable as a result of the state-transition $(s_j|s_i,a)$. Similarly, the reward component $f_t(s_j|s_i,a)$ is defined as-

$$f_t(s_j|s_i,a) = \left(\frac{\gamma(s_j|s_i,a)}{C_{PNC}}\right) 100\% \tag{3.20}$$

In (3.20), the parameter C_{PNC} is the maximum throughput that can be supported by the PNC and $\gamma(s_j|s_i,a)$ is the total throughput associated with the piconet when its current state s_i undergoes a transition to state s_j in the presence of action $a \in A_s$. Finally, the latency reward function $f_l(s_j|s_i,a)$ is defined as:

$$f_l(s_j|s_i,a) = \left(1 - \frac{Lat^{HO}(s_j|s_i,a)}{Lat^{HO}(N)}\right) 100\% \tag{3.21}$$

Here, $Lat^{HO}(N)$ is the overall latency that will be incurred when all DEVs in the piconet suffer a delay equivalent of one SF and $Lat^{HO}(s_j|s_i,a)$ denotes the cumulative latency of implementing the ***PNC Handover*** process. This is calculated by summing the handover latency over all the DEVs that will be affected due to the state-transition $(s_j|s_i,a)$. As discussed in [72], the process of ***PNC Handover*** causes a minimum latency of duration (*HandoverTimeout+SuperframeDuration*) and all DEVs which become serviceable as a result of the state transition $(s_j|s_i,a)$ are affected by this factor. As per [72], both the parameters *HandoverTimeout* and *SuperframeDuration* can extend up to a maximum duration of 6.5 msec. Therefore, in our calculations, we use these values for evaluating the parameter $Lat^{HO}(s_j|s_i,a)$.

Optimal Delegation Policy: To find out the ideal delegation policy $\pi = (\delta(s_1), \delta(s_2), .., \delta(s_j), ..)$ for this framework, we use the value iteration algorithm (VIA) shown in Algorithm 3. This is a dynamic optimization technique which is commonly used in the context of communication networks [68], [84]. With reference to any arbitrary state allocation, the algorithm uses the state-transition probabilities $p(.|.)$ and the corresponding rewards $r(.|.,a)$ to find the convergence of the value function over a threshold ε using multiple iterations η.

Algorithm 3: Value Iteration Algorithm (VIA)

Input: State transition probabilities and rewards $p(s_j|s_i)$, $r(s_j|s_i,a)\ \forall s_j, s_i \in S$, discount factor (ω) and convergence threshold (ε); Set iteration cursor $\eta = 0$;

Select $v^0 \in V$

for *each state* $s_i \in S$ **do**

calculate $v^{\eta+1}(s_i)$ using :

$$v^{\eta+1}(s_i) = \max_{a \in A_s} \left\{ r(s_i,a) + \sum_{s_j \in S} \omega p(s_j|s_i,a)\, v^{\eta}(j) \right\}$$

if $\left\| v^{\eta+1} - v^{\eta} \right\| < \varepsilon(1-\omega)/2\omega$ **then**

goto step-9

else

$\eta \leftarrow \eta + 1$

goto step-2

for *each* s_i **do**

choose decision $\delta(s_i)$ using :

$$\delta(s_i) = arg\max_{a \in A_s} \left\{ r(s_i,a) + \sum_{s_j \in S} \omega p(s_j|s_i,a)\, v^{\eta}(j) \right\}$$

3.2.2.5 Analysis of Complexity

Complexity of MDP Model: To analyze the complexity of our proposed MDP framework, we represent the total number of states in the MDP model as a function of the state-variables n_P, n_{d_i} and $l_{d_i,P}$ respectively. Considering practical deployment scenarios, we assume that each piconet operates with a maximum of up to three delegable nodes (in addition to the default PNC P) and derive the corresponding expressions for the total number of system states. In a generalized MDP model, the total number of state combination in the system is denoted using the Cartisian product of the constituting variables. However, for our MDP model, the symmetry of the system-states simplifies the overall state-count and the state complexity expressions for the simplified MDP model are derived as follows.

For a scenario with only one delegable node (i.e., $|\mathcal{D}| = 1$), the default PNC can occupy up to N load-levels corresponding to $n_P = 1, .., N$ and in each of these load levels the delegable node can have up to $Nl_{d_i,P}$ combinations. Depending on the number of link-states considered for the self-backhaul link $l_{d_i,P}$, the complexity of the system $C_{(|\mathcal{D}|=1)}$ will then be -

$$C_{(|\mathcal{D}|=1)} = N^2 l_{d_i,P} \tag{3.22}$$

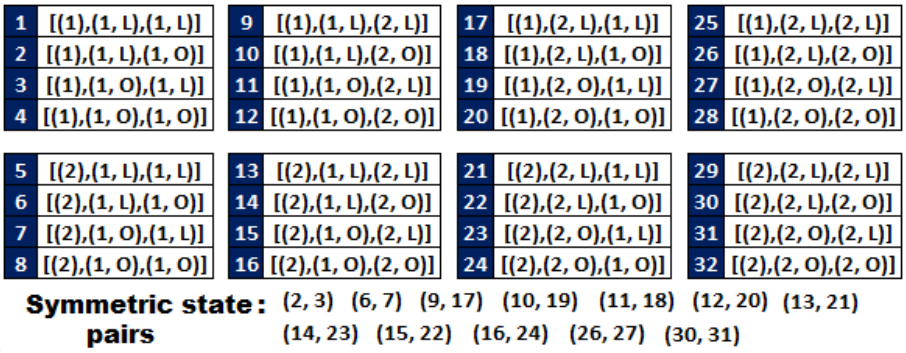

Figure 3.6: Complexity analysis of MDP model: State combinations for $\{(n_P), (n_{d_1}, l_{d_1,P}), (n_{d_2}, l_{d_2,P})\}$ with $N = 2$, $|\mathcal{D}| = 2$ and two link states $l_{d_i,P}$

Table 3.1: Comparison of state complexity in the MDP model under different system configurations

MDP Model Parameters	**Parameter Values**																	
$\|\mathcal{D}\|$	1						2						3					
$l_{d_i,P}$ States	2			3			2			3			2			3		
N	1	2	3	1	2	3	1	2	3	1	2	3	1	2	3	1	2	3
State Count (Simplified Model)	2	8	18	3	12	27	3	20	63	6	42	135	4	48	144	15	96	297
State Count (Theoretical Model)	2	8	18	3	12	27	4	32	108	9	72	243	8	128	648	27	432	2187

For piconets with two delegable nodes, Fig. 3.6 shows different system states along with the set of all symmetric state-pairs (corresponding to $N = 2$ and for a bi-state self-backhaul link $l_{d_i,P}$). Due to this state-symmetry, the complexity of the actual state-space is much lower than that of the theoretical state-space. To clarify this point, TABLE-3.1 shows the simplified and theoretical state complexity of different system configurations. Based on these simplifications, the expression for state complexity of a system with $|\mathcal{D}| = 2$ and $|\mathcal{D}| = 3$ are expressed as $C_{(|\mathcal{D}|=2)} = N^2 l_{d_i,P} \frac{(Nl_{d_i,P}+1)}{2}$ and $C_{(|\mathcal{D}|=3)} = 2N^2 l_{d_i,P} \left(\frac{Nl_{d_i,P}}{2} + 1\right)$ respectively. Generalizing the above, the state-complexity of our system model will be -

$$C_{(|\mathcal{D}|\in\{2,3\})} = C_{(|\mathcal{D}|=1)} \frac{(Nl_{d_i,P} + (|\mathcal{D}| - 1))(|\mathcal{D}| - 1)}{2} \tag{3.23}$$

As shown by (3.23), the complexity of theMDP model increases both with an increase in the piconet's size as well as with increasing number of delegable nodes. However, as mmWave piconets operate over a much smaller coverage area and system size, the overhead of state complexity due to the delegation model will not adversely affect the performance of the system.

Complexity of Optimization Model: Since our MDP framework uses the VIA methodology to determine the optimal delegation policy, the complexity of our optimization model will be determined

by complexity of the underlying VIA model. The VIA is a form of successive approximation algorithm which operates by optimizing the value-function over a convergence threshold ε using multiple iterations. The complexity of each iteration in VIA is denoted using $O(|A||S|^2)$ where, $(|S|)$ and $(|A|)$ represent the cardinality of the set of states and that of the permissible actions. In VIA, the number of iterations required to arrive at the optimal value is dependent on the nature and magnitude of the discount factor (ω). For a fixed value of ω, VIA can be solved in polynomial time where total number of iterations under the worst-case scenario is proportional to $1/(1-\omega)log(1/(1-\omega))$ [85].

3.3 Simulation and Results

In this section, we evaluate the performance of our proposed blockage mitigation approaches using a MATLAB-based simulation environment and discuss the obtained results. The simulation model discusses the network layout and its configuration with respect to different system parameters. It also discusses the details of the NYUSIM tool which has been used for the calculation of the PNC load. To analyse the result, we first evaluate the performance of static-policy-based approaches with respect to the default mode of piconet operation and subsequently evaluate the performance of different approaches based on the DT-MDP model.

3.3.1 Simulation Setup

The simulation setup consists of an indoor WPAN scenario which is representative of a typical mmWave based IOT network [82] . The network comprises of several DEVs which are uniformly distributed over a 2D-space. The space also includes rectangular shaped obstacles of varying sizes interspersed in between the DEVs. To incorporate node mobility under indoor conditions, a certain number of these DEVs are made to change their location every second by following a random-walk model. The model uses a stride length of 1 meter and a refresh rate of 1 second corresponding to an average pedestrian speed of 4 Km/h. The values of all these system parameters are given in TABLE-3.2

In the simulation setup for static-policy based approaches, a DEV is considered to be associated to a PNC, only if the corresponding link is in LoS state, whereas, in case of the DT-MDP approaches, DEVs are considered to be (associated or) serviceable by a PNC, only if the available SNR is sufficient to support their applied data-rates. Since beam blockage and signal attenuation cause DEVs to see a wide range of SNR values, we need to determine the SNR at each of the DEVs to calculate the overall

Table 3.2: System Parameters

Parameter Name	Description
Room Dimension (scaled)	10 meter x 10 meter
Number of DEV Nodes	10
Distribution of DEV Position	Uniformly distributed in 2D plane
Number of Obstacles	4
Obstacle Length: 0 meter (Min.) - 2 meter (Max.) Obstacle Breadth: 0 meter (Min.) - 2 meter (Max.)	
Mobility Model Parameters	
DEV Mobility Pattern	Random-walk Model
Stride Length	1 meter
Rate of Steps	1 step/sec
Number of Steps	10

PNC load. For this, we use the NYUSIM tool [86] which is a popular open-source channel simulator developed for mmWave frequencies. It maps various PNC-DEV separation distances and distance within foliage (in case of obstacles) with respect to their SNR values. For this, the NYUSIM tool uses various standard parameters as shown in TABLE-3.3. On obtaining the SNR at each DEV location, the load at PNCs P and d are calculated using Algorithm 4. Based on the changes in PNC load levels and the state of the self-backhaul link(s), the state-transition probabilities and their corresponding rewards are then calculated. Finally, the optimal policy corresponding to a given deployment scenario is calculated based on the MATLAB implementation of Algorithm 3.

In practical scenarios, the pattern of traffic generation among the DEVs would vary with time and would influence the selection of delegable nodes and their frequency of delegation. However, in our simulation setup, we have considered the worst-case scenario where all DEVs generate CBR traffic. As a result, all the delegation decisions would be influenced only by the change in the blockage scenario of the piconet.

3.3.2 Result Analysis

We first evaluate the performance of the static-policy-based DCD approaches with respect to the default mode of PNC operation. We compare the effectiveness of the Maximally Connected and the Maximally Stable Neighbour Approaches using performance metrics like DEV visibility with respect to the PNC, distribution of DEV-DEV link costs, etc. Subsequently, we introduce some DCD approaches based on the DT-MDP framework and evaluate their performance with respect to the factors like percentage of serviceable DEVs, the share of disconnected and latency affected DEVs, etc.

Algorithm 4: Evaluate PNC loads (n_P, n_d) using NYUSIM

Input: IEEE 802.15.3c ref. superframe (t), Mean applied data-rate at DEV n $(Thpt_n)$, SNR Threshold (SNR_{Th}), Number of DEVs connected to PNC nodes (n_P, n_d);

for *each* $PNC \in \{P \cup \mathcal{D}\}$ **do**
  for *each* $n \in N$ **do**
    Find $d_{(n,PNC)}(t)$ i.e. distance from n to PNC
    if $l_{n,PNC}(t) \neq L$ **then**
      Find distance within foliage $d''_{(n,PNC)}(t)$
    Get $SNR_n(t)$ using $d_{(n,PNC)}, d''_{(n,PNC)}$
    if $(SNR_n < SNR_{Th})$ & $\left(n \in \text{DEV}^{List}_{(PNC)}\right)$ **then**
      $Thpt_{PNC} = Thpt_{PNC} + Thpt_n$
      if $PNC = P$ **then**
        $n_P \leftarrow n_P + 1$ // Update n_P load
      else
        $n_d \leftarrow n_d + 1$ // Update n_d load

Table 3.3: NYUSIM Parameter settings

Antenna Properties	
Parameter Name	**Description**
Antenna Azimuth HPBW	28.8 degrees
Antenna Elevation HPBW	30 degrees
Physical Layer Properties	
Channel Model	Statistical Model
Operating Frequency	28 GHz
RF Bandwidth	800 MHz
Tx-Rx Polarization	Co-polar
PNC Height	2.5m
Tx Power	17 dBm
Foliage Attenuation	0.4 dB/m

3.3.2.1 Evaluation of Static Policy based DCD

PNC Visibility: Fig. 3.7 shows the visibility of the DEVs with respect to the PNC for different configurations of node and obstacle densities. It compares the Maximally connected neighbour approach with respect to the default mode of piconet operation in terms of the percentage of DEVs that are connected to the PNC. It can be observed that the average number of PNC connected DEVs is always higher under the DCD approach. It can also be observed that the percentage of PNC connected nodes tend to decrease with an increase in the number of obstacles. Similarly, for a given obstacle

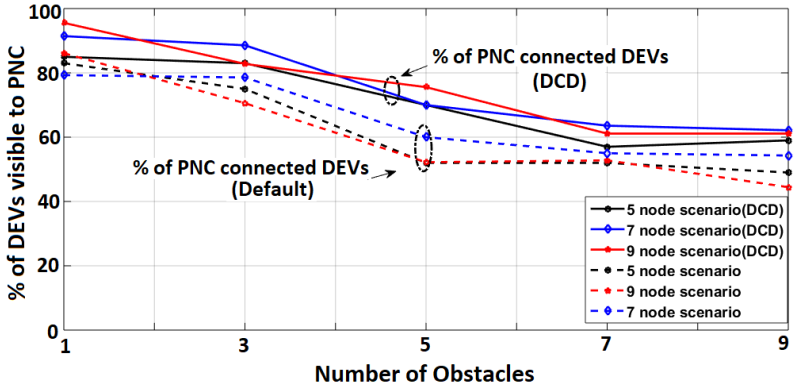

Figure 3.7: Percentage of DEVs visible with respect to PNC under different system configurations.

density, the percentage of PNC connected DEVs tends to decrease with an increase in node density under the default mode of operation. These observations can be attributed to the fact that for a given system size, an increase in obstacle density leads to a corresponding increase in the outage probability.

Node-to-Node Packet Transmission Costs: As discussed in Section 3.2.1, the assignment of link utility values $U(l_{src,dst}(t))$ between any pair of arbitrary source and destination nodes (src,dst), provides a qualitative score of the link $l_{src,dst}(t)$. However, due to beam blockage, many such links may go under outage and data-packets may have to be routed through multiple alternate hops to reach the destination node. Therefore, in Fig. 3.8, we plot the distribution (CDF) of node-to-node packet transmission costs in terms of the number of hops required to reach a destination node from a given source node and compare the two static-policy based DCD approaches (maximally connected and maximally stable neighbour approaches) with respect to the default mode of piconet operation.

In Figs. 3.8(a), (b) and (c), we plot the CDFs for various piconet configurations (e.g., 9 DEV-9 Obstacle, 7 DEV-7 Obstacle and 5 DEV-5 Obstacle scenarios) to compare the performance of Algorithm 1 (i.e., maximally connected neighbour approach) with respect to the default mode of PNC operation. In each of these configurations, we assume that the DEVs are static and the simulations are performed for 20 different seed values. From the CDF plots, it can be observed that, a larger share of node-to-node paths have lower packet transmission costs (number of hops) with the DCD approach compared to the default approach of PNC operation and this trend increases as the size of the piconet is increased. Since, the DCD approaches operate by improving the PNC node's visibility with respect to the DEVs, a greater number of DEVs become serviceable by the PNC under Algorithm 1. This leads to more LoS links becoming available between the member nodes and simplifies the network

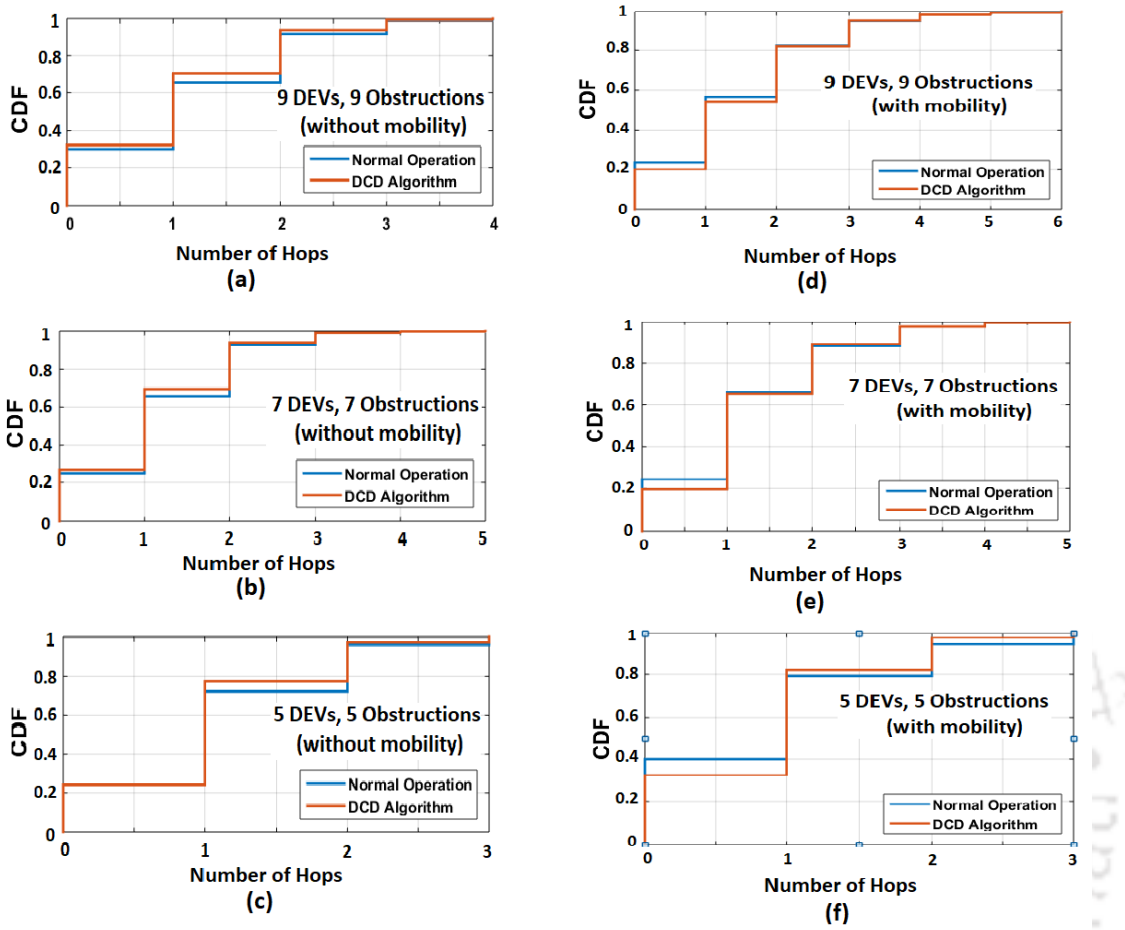

Figure 3.8: Distribution of packet transmission costs in terms of number of hops for different network configurations; (a)-(c) piconet without node mobility; (d)-(f) piconet with node mobility

topology with lower packet transmission costs.

In a similar manner, we plot the CDFs in Figs. 3.8(d), (e) and (f) for the case when the DEVs are mobile (with mobility parameters as in TABLE-3.2). In this case, we apply Algorithm 2 of DCD (i.e., the maximally stable neighbour approach) and compare its performance to the default mode of piconet operation. The results obtained show that a major share of node-to-node links have lower packet transmission costs in comparison to that of the default mode of PNC operation. However, in this case, the improvement in performance is not as pronounced as in the earlier cases of Figs. 3.8(a), (b) and (c). This may be attributed to the fact that Algorithm 2 emphasises the stability of the self-backhaul link more than better node visibility.

3.3.2.2 Evaluation of DT-MDP Framework based DCD

As discussed in Section 3.2.2.4, our proposed DT-MDP framework permits customization of the objective function to adapt its performance to different operating conditions. To illustrate this, we introduce some alternate heuristic policies and compare their performance to that of the optimal policy π^{opt}. For this, the following policies were considered.

(i) A policy π^{Fixed} in which the piconet's control always stays with the default PNC. This may also be considered as the default policy for piconet control.

(ii) A policy $\pi^{Max-Thpt}$ in which the piconet's control is delegated to a PNC offering maximum throughput. This is similar to the maximally connected neighbour approach of DCD (Algorithm 1).

(iii) A delegation policy π^{Random} where the piconet control is randomly assigned to any of the available delegable nodes following a uniform distribution.

We implement each of these policies within our MATLAB environment and evaluate their performance for various different application scenarios. For this, we introduce three distinct heuristic application profiles (i.e., Residential, Industrial and Urban-Micro) by adjusting the weights w_d, w_t and w_l of the reward components. TABLE-3.4 shows the values of these heuristically chosen weightages for the three application profiles.

Table 3.4: Reward Component Weights For Different Application Profiles

Weightage	Residential	Industrial	Urban-Micro
w_d	40%	20%	33.33%
w_t	40%	20%	33.33%
w_l	20%	60%	33.33%

In the residential profile, a greater significance is placed on the maximization of system throughput and minimization of node disconnections. Therefore, weightages w_d, w_t assigned values of 40% each, and the remaining 20% weightage remains for the latency reward component (i.e., w_l). In the industrial profile, multiple PNCs are generally deployed to provide redundant coverage, therefore minimization of the handover latency is the main objective. For this, we assign 60% weightage to the w_l component, and the remaining weightage is equally distributed between w_d, w_t. Finally, in the urban-micro scenario, a very diverse range of user requirements may be present. For this, since we cannot quantify

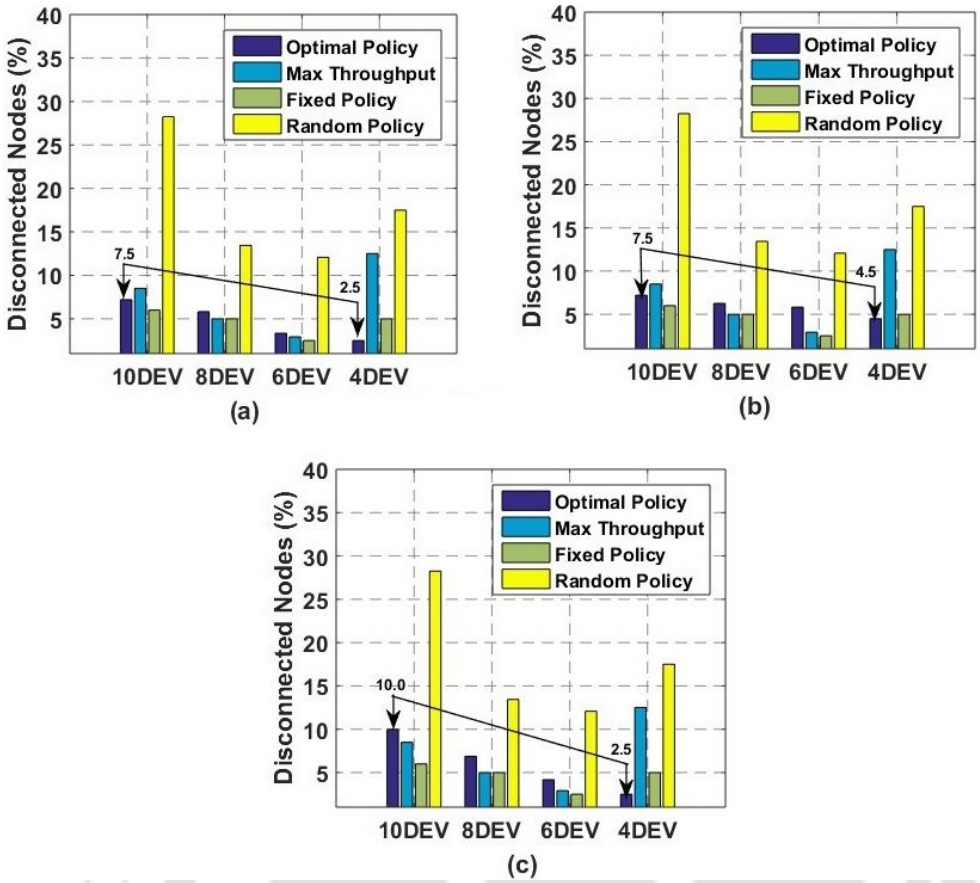

Figure 3.9: Variation in percentage of node disconnection for different configurations of system size (user count) and application profiles. (a) Residential profile. (b) Urban-micro profile. (c) Industrial profile

one objective to be better than another, an identical weightage of 33.33% is assigned for each of them. Based on these application profiles, we examine the performance of the optimal delegation policy π^{opt} with respect to the alternative policies (π^{Fixed},$\pi^{Max-Thpt}$ and π^{Random}) for performance measures like the number of disconnected nodes, the number of serviced nodes and the latency of control delegation.

Number of Disconnected Nodes: When the process of ***PNC Handover*** is executed, a subset of the currently serviceable DEVs can no longer be serviced by the new PNC. This leads to the disconnection of some DEVs from the piconet. In Figs. 3.9(a),(b) and (c), we compare the performances of different delegation policies with respect to the number of such node disconnections when the reward functions are calibrated for the residential, urban-micro and industrial profiles respectively. In each case, the results are further categorized with respect to different system sizes (user counts). From Figs. 3.9(a)-(c), it can be observed that the percentage of node disconnections under the π^{opt} policy decreases with a reduction in system size for all the application profiles. Moreover, for a given network

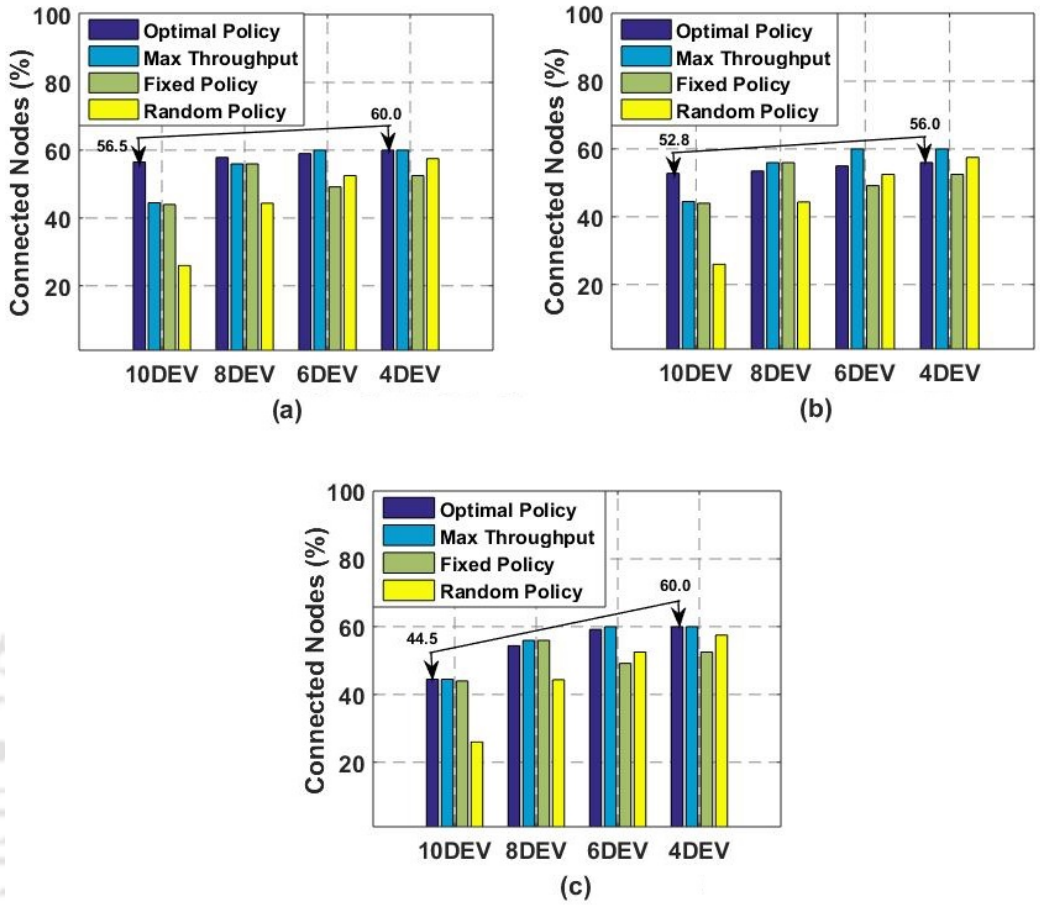

Figure 3.10: Distribution of connected (serviceable) DEVs as function of multiple delegation policies under different system configurations (user counts) and application profiles. (a) Residential profile. (b) Urban-micro profile. (c) Industrial profile

size, the percentage of node disconnections under the π^{opt} policy is higher for the industrial profile than that for the residential or the urban-micro profiles. Between the three profiles, the percentage of node disconnections increases most steeply with increasing system size for the industrial profile. These differences in the percentages of node disconnections may be attributed to the relative differences between the node disconnection weightages w_d of 40%, 33.33% and 20%, respectively, for the residential, urban-micro and the industrial profile. Among these three policies, π^{Random} appears to give the poorest performance.

Number of Serviced Nodes: Figs. 3.10(a),(b) and (c) show the distribution of the total number of serviced DEVs for different system configurations under the residential, urban-micro and industrial profiles respectively. For all the application profiles, we observe that the percentage of serviced nodes gradually decreases with increasing system size. For the residential and the urban-micro profiles (Figs.

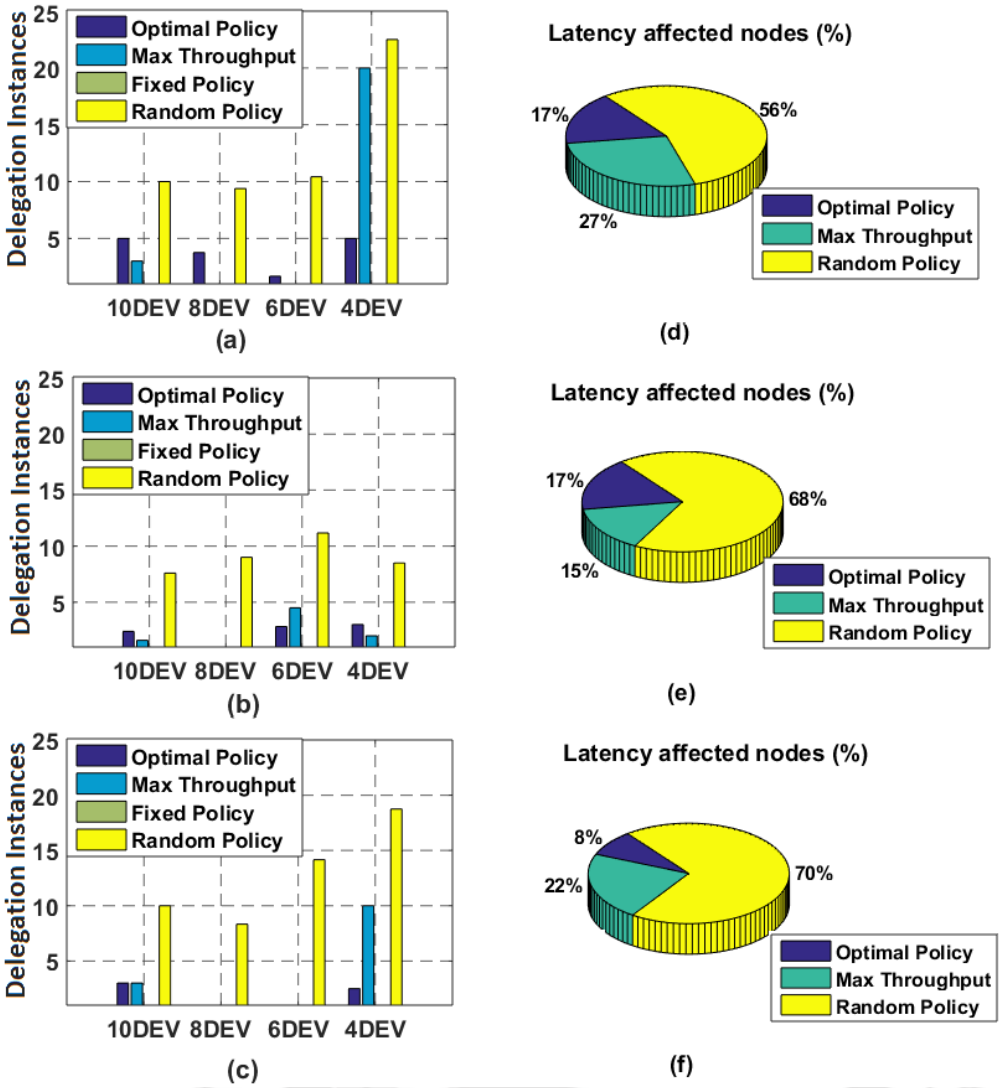

Figure 3.11: Distribution of control delegation instances and percentage of latency affected nodes for different configurations of system load and application profiles. (a) Residential profile. (b) Urban-micro profile. (c) Industrial profile. (d) Latency affected nodes (%) residential profile. (e) Latency affected nodes (%) urban-micro profile. (f) Latency affected (%) industrial profile

3.10(a) and (b)), the percentage of connected (serviced) DEVs for the π^{opt} policy decreases by about 4% with an increase in piconet size from the 4DEV to the 10DEV scenario, whereas, for the industrial profile (Fig. 3.10(c)), it decreases more steeply (by about 15%) when the piconet size increases from the 4DEV to the 10DEV scenario. Under the residential profile, the π^{opt} policy provides connectivity to maximum number of DEVs. Considering these results in relation to the throughput reward weightage w_t, it can be observed that the above results correlate with the values of w_t weightages viz. 40%, 33.33% and 20% respectively for the residential, urban-micro and industrial profiles (as shown in TABLE-3.4). We can then infer that a higher share of w_t component corresponds to the delegation

model which selects a better-connected PNC. Moreover, by suitably adjusting the relative share of w_t in the reward function, a network operator can regulate the number of serviceable DEVs and influence the piconet's traffic.

Latency of Control Delegation: As discussed earlier, the execution of ***PNC Handover*** process may cause additional latency in some of the member nodes. It would therefore be important to study the handover induced latency as a performance metric for the evaluation of these policies. In Figs. 3.11(a),(b) and (c), we show the distribution of control delegation instances as a function of different system sizes for the three application profiles. It can be observed that the number of delegation instances under the π^{opt} policy is much higher for the residential and urban-micro profiles than under the industrial profile. In the industrial profile (Fig. 3.11(c)), the π^{opt} policy has significantly fewer delegation instances in comparison to the $\pi^{Max-Thpt}$ and π^{Random} policies.

Similarly, from Figs. 3.11(d),(e) and (f), it can be observed that the percentage of latency affected DEVs under π^{opt} is much less for the industrial profile (at 8%) than under the residential (at 17%) and the urban-micro profiles (at 17%). This may be attributed to the fact that the industrial profile assigns 60% weightage towards latency minimization whereas the residential (at 17%) and the urban-micro profile (at 33.33%) have much lower weightages for w_l. From this it may be concluded that though the π^{opt} profile does create some extra latency when control is delegated from one PNC to another, these are far lower than those created by the $\pi^{Max-Thpt}$ and π^{Random} profiles. It is then important to observe that depending on the application requirements, the network operator can adjust the value of w_l to regulate the delegation induced latency.

Total Expected Discounted Rewards: To see the overall efficacy of the π^{opt} policy, we calculate and compare the average values of the total discounted rewards for over 500 simulation trials for each of the delegation policies π^{opt},π^{Fixed},$\pi^{Max-Thpt}$ and π^{Random}. Similarly, trials were also conducted for each of the application profiles. The total expected discounted rewards for each of the policies under each of the three application profiles are given in Fig. 3.12. It can be observed that the optimal policy consistently outperforms all other delegation policies in all the application profiles confirming the effectiveness of our proposed approach.

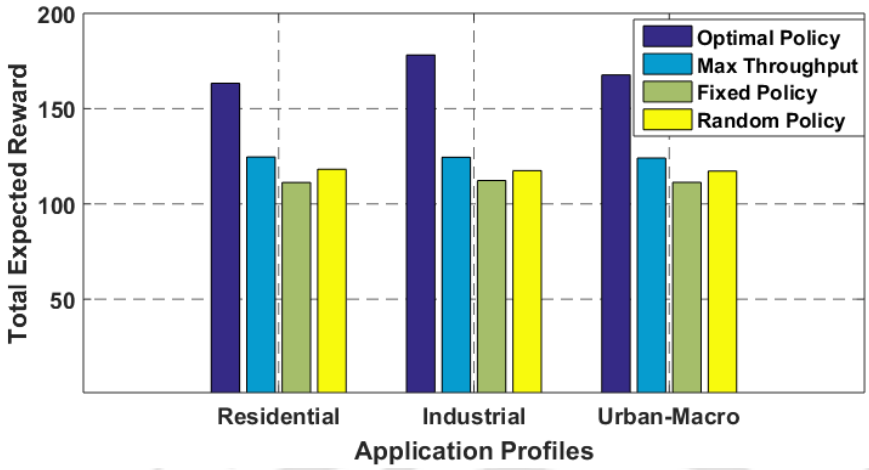

Figure 3.12: Value of total expected discounted reward for various policies.

3.4 Conclusion

In this Chapter, we have proposed a MAC-layer based methodology to address the problem of beam blockage in mmWave indoor networks. This uses the process of ***PNC Handover*** as defined in the IEEE 802.15.3c MAC standard [72], to achieve blockage tolerance by allowing a PNC node to dynamically relinquish its administrative controls to other PNC capable member nodes. These delegated PNC nodes may be operating from different vantage points and may therefore be able to mitigate beam blockages. Based on the process for dynamic control delegation (DCD), we have evaluated two categories of approaches. Under the first category, a fixed set of rules (or static-rule based policies) are used to take delegation decisions. Here, we have proposed and evaluated two types of approaches (i.e. the maximally connected and the maximally stable neighbour approach). The first approach aims to maximize node visibility under a static piconet scenario whereas the second one aims to delegate to a node with a stable self-backhaul link under a mobile scenario. Under the second category of DCD, we use a DT-MDP framework to model the dynamic behaviour of a piconet with respect to its changing blockage scenario and the effects of mobility induced changes and use a dynamic optimization methodology to identify a delegable node. The delegation model is operated using multiple performance metrics like latency, throughput and node disconnections and can be reconfigured based on operator requirements. By using statistical beam blockage models derived from field trials, the efficacy of the proposed solution is evaluated with respect to three different application profiles (viz. Residential, Urban-Micro and Industrial) for multiple system configurations.

The obtained results indicate that the DT-MDP framework based approaches are better suited for operations where the network conditions are dynamically evolving. Their performance depends upon the values of component weightages in the reward function. By using the heuristic reward component weightages as in TABLE-3.4, the system demonstrated 12% improvement in node connectivity under the Residential profile while keeping node disconnections at levels comparable to the default approach. Under the Industrial profile, the system demonstrated minimal delegation latency but at the expense of lower node connectivity and higher node disconnections, whereas, under the Urban-Micro profile, the system delivered an intermediate performance. These results indicate that our proposed methodology can be used to mitigate beam blockage in mmWave networks without incurring any additional hardware costs and would allow the networks to operate over a wide range of indoor IoT scenarios.

4

MAC Layer Methods for Efficient Blockage Mitigation in MLC Architectures

Contents

This chapter presents different MAC-layer techniques for improving the efficiency of blockage mitigation solutions that are based on the multi-link connectivity (MLC) architecture. The proposed techniques employ different device-centric approaches to reduce the infrastructure and resource consumption footprint of an MLC architecture, thus making the underlying blockage mitigation solutions more viable for deployment in low-cost indoor scenarios. The device-centric approaches are simple to implement and easy to reconfigure, and can therefore adapt to a wide variety of deployment conditions. The results obtained from extensive simulation trials have shown that the dynamic link level redundancy (DLLR) approaches can be used to effectively reduce the requirement of redundant infrastructure in MLC-based blockage mitigation solutions for efficient utilization of network resources.

4.1 Introduction

In mmWave systems, a broad variety of blockage mitigation solutions use the MLC architectures to address the problem of link outages. These architectures involve deployment of multiple redundant links through the use of multiple radio access technologies (RATs) or radio access networks (RANs) to achieve blockage tolerance and rely upon spatial diversity to provide robust connectivity. As discussed in Chapters 2 and 3, most of the prominent network and MAC-layer based blockage mitigation approaches e.g., [65]- [68], [69]- [71] and some of the physical layer approaches (e.g., the beam-diversity based techniques in [62], [63]) use MLC architectures to achieve blockage tolerance. Although, these approaches can be quite effective in mitigating beam blockages, they require a lot of additional network infrastructure and resources to support their operations. Since these architectures deploy a fixed amount of redundant infrastructure (e.g., in terms of a standby network or backup links) to achieve blockage tolerance, they cannot readily adapt to the changing blockage conditions and, under normal operating conditions, a lot of network capacity and other vital network resources remain unutilized. This motivated us to explore ways of dynamically adjusting the extent of link-level redundancy so as to enable mmWave networks to operate more efficiently while providing reliable connectivity.

With the above goal in mind, we propose in this chapter, some MAC-layer based device-centric approaches for dynamically controlling the extent of link redundancy in mmWave MLC architectures. These approaches help member nodes to dynamically determine a subset of the redundant links which would be used to maintain a certain grade of blockage reliability while minimizing the usage of this redundant infrastructure. These techniques are also aligned with the concept of cloud-based RANs

where network resources are allocated on demand based on the prevailing conditions. The main advantages of using these approaches are-

(i) They can be implemented using device-level software updates which are easy to implement and re-configure.

(ii) Since member nodes act as the source or sink for a data-stream, they are best suited to evaluate their surrounding blockage scenario and take decisions on redundancy control.

(iii) They can be applied over different MLC architectures without any significant change in the network infrastructure.

4.2 MLC Configuration using IEEE 802.15.3c based SOP Architecture

In this section, we discuss the implementation of a mmWave MLC architecture using the IEEE 802.15.3c MAC-standard [72] based simultaneously operated piconet (SOP) configuration. Although, MLC architectures can be implemented using many other network configurations, some of the commonly used configurations have been depicted in Fig. 4.1(a) and (b). It can be observed that in both of these configurations, the extent of redundancy (in terms of the standby network or the back-up links) is fixed and that it cannot be regulated based on the network conditions. In Fig. 4.1(c), the implementation of an MLC architecture using the IEEE 802.15.3c standard based SOP configuration is shown. It consists of a family of parent and dependent piconet controllers (PNCs) operating together simultaneously in the form of a hierarchy to provide redundant network coverage to the set of member nodes (DEVs). In our work, we have used this form of MLC architecture as a reference for implementing our proposed DLLR algorithms. The main advantages of this configuration are as follows:

(i) The hierarchy of PNCs in an SOP structure can be rapidly reconfigured based on changing traffic conditions or blockage scenarios within a piconet.

(ii) It does not require any dedicated network entity for implementing the MLC architecture. So, the piconet can be scaled as per operator's requirements and can be operated with minimal cost and infrastructure overheads.

(iii) Since, the resource allocation mechanisms in these architectures are regulated by the parent PNC using various algorithms, they can be further customized to incorporate the DLLR algorithms.

(iv) Since dependent piconets within an SOP structure operate using mutually exclusive pseudo-static channel time access slots (p-CTAs), where each DEV gets to operate in a dedicated time-division multiple access (TDMA) distributed slot, the communicating nodes do not cause interference for each other even when node density is high.

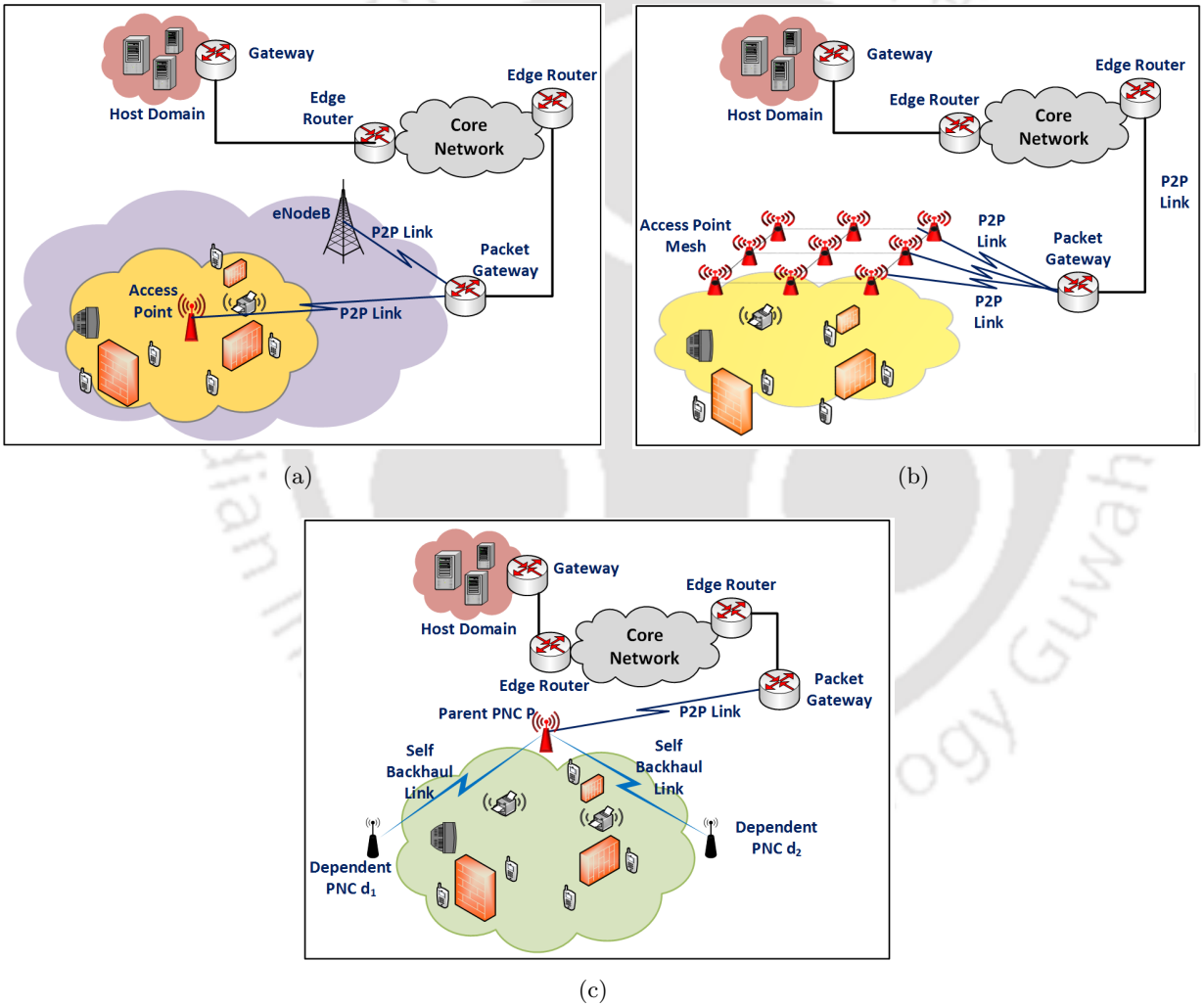

Figure 4.1: Different MLC configurations of mmWave access networks: (a) LTE-mmWave WLAN based MLC approach for indoor network; (b) mmWave based MLC approach for indoor network using access point mesh configuration; (c) mmWave based MLC approach for indoor network under SOP configuration

4.2.1 Frame Structure for Multiple Simultaneous Connectivity

In mmWave networks, the SOP architecture (as in [72]) is mainly envisaged to extend connectivity inside coverage holes, to provide preferential service to a specific class of serviced DEVs, or to scale up the size of a piconet. It assumes that each member node is associated with only one PNC from which it gets serviced. Hence, to enable multiple PNC connectivity (as under the MLC architecture), the DEVs in SOP configuration will require the following modifications in their MAC-layer frame structure:

In case of the member nodes, each DEV will be required to keep multiple MAC addresses using which it can get associated to multiple PNCs. To manage the transmission and reception of data-packets using each of these MAC addresses, a DEV node also has to maintain a separate set of packet buffers. At the PNC's level, since any PNC capable member node can be selected to operate as a PNC, the changes applicable at the DEV level are also applicable for the PNC nodes. To establish redundant connectivity, a DEV node associates with multiple PNCs as per the process shown in Fig. 4.2. For each of the redundant PNCs that are radio-visible with respect to a DEV (DEV#2 in this case), the node looking to establish a new association with a PNC, first synchronizes its clock using the beacon signals of the PNC. It then sends an *Association Request Command* to the relevant PNC using a specific frame format as in [72]. A PNC receiving this request can either accept or reject it by sending an appropriate *Association Response Command*. If the PNC accepts the association request, it generates the DEV id for the associating node (with its corresponding group key) and conveys it to the associating device. On receiving the response command, the requesting DEV sends a second *Association Request Command* with the DEV Id as shared by the PNC. This time, the PNC responds with an immediate acknowledgement and adds the DEV Id (and its MAC address) in its list of associated devices. It also broadcasts this information to the other DEVs in the piconet using appropriate information element (IE) in the subsequent beacon signal. The DEV completes the above process for each of the redundant PNCs using separate MAC addresses to establish the MLC. If a PNC is unable to accommodate an association request, it simply sends the corresponding response command without the DEV Id or the group keys. The DEV node reads the response message and understands that its request has been turned down. Similarly, if the node association request does not reach a PNC due to beam blockage and the statutory time for DEV association gets over, the requesting node understands that its request has been turned down.

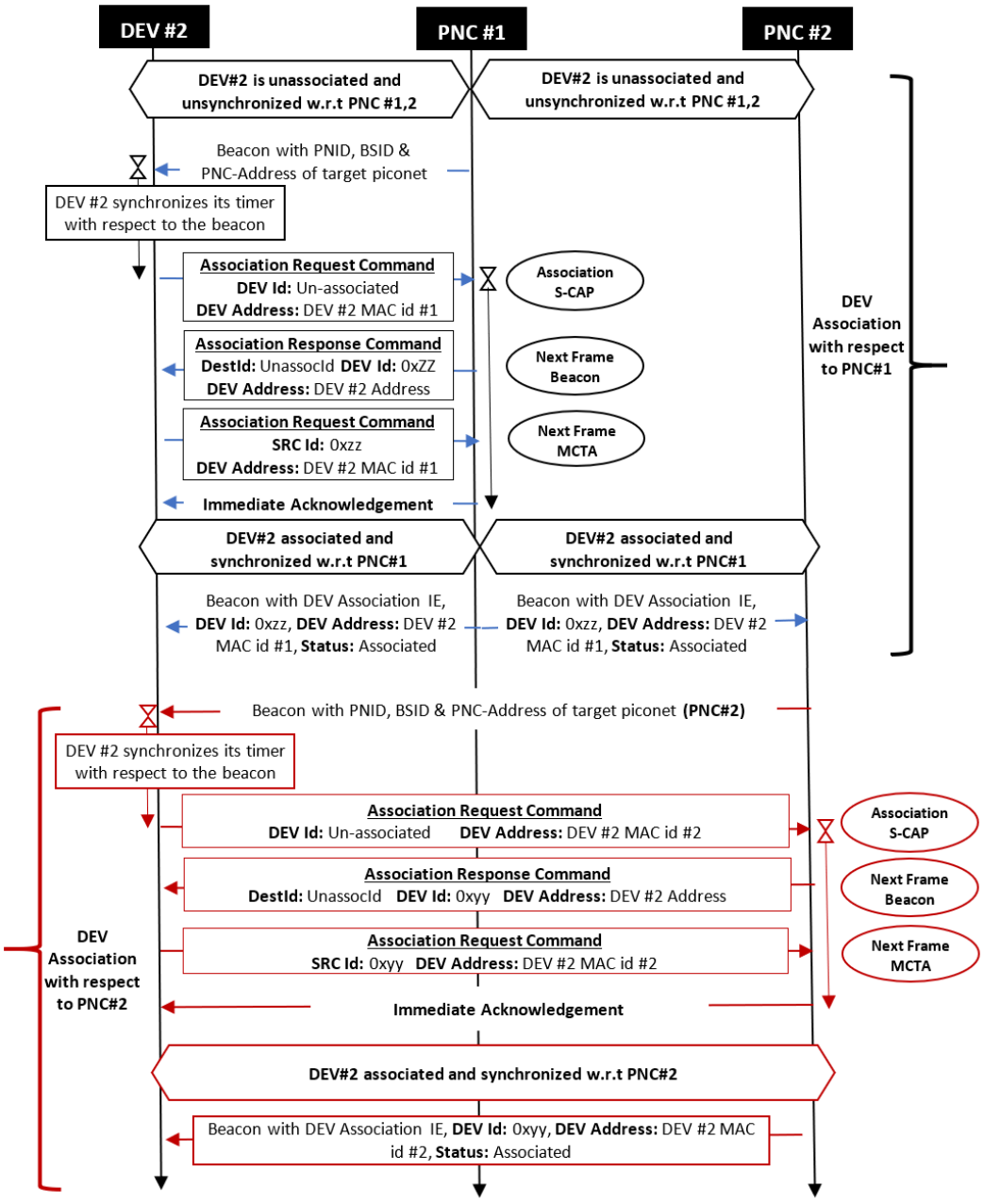

Figure 4.2: Process of DEV association with respect to multiple PNCs under IEEE 802.15.3c SOP based MLC architecture

4.2.2 Transceiver Design to Support MLC Operation

To incorporate the above MAC-layer operations and to communicate using a redundantly connected PNC architecture, the communicating nodes in the piconet should have an appropriate transceiver design. In Fig. 4.3(a), we show the general structure of an MLC based transceiver unit. It consists of multiple MAC layer interfaces to facilitate macro-diversity and redundantly send or receive data-

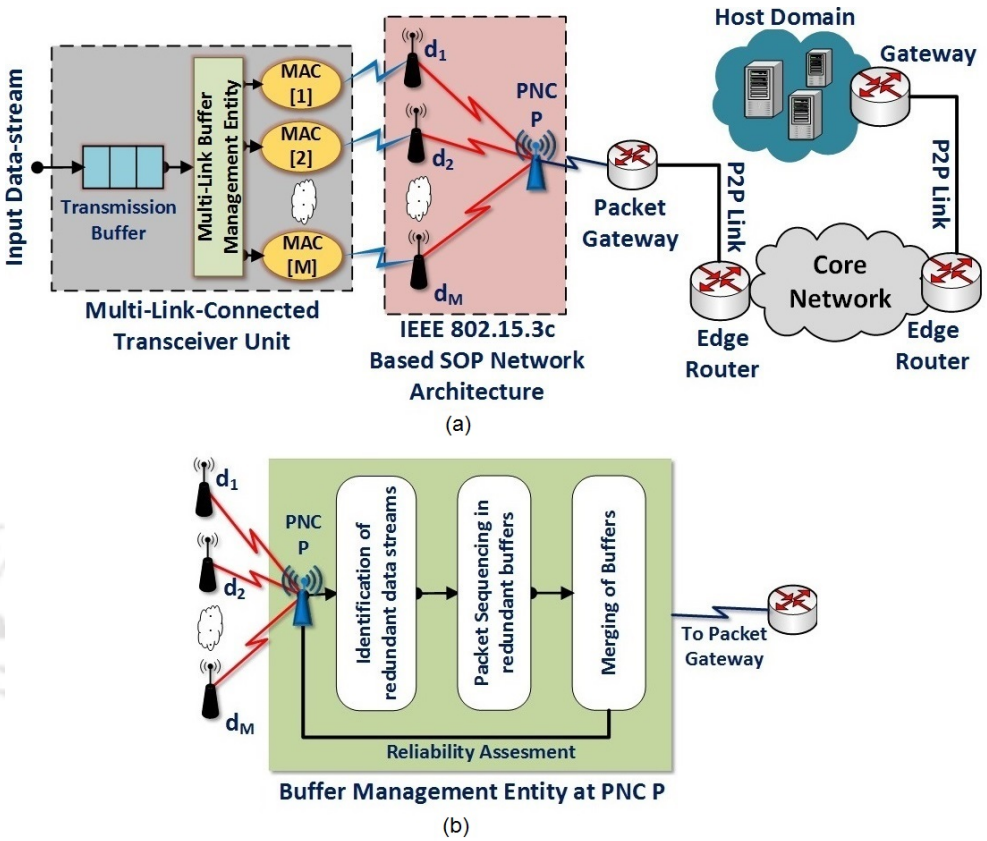

Figure 4.3: Architecture of an IEEE 802.15.3c based SOP structure in MLC configuration (a) MLC enabled transceiver design along with its interfacing with the core network; (b) Management of packet buffers at the parent PNC P

packets using different Basic Service Set Identifiers (BSSIDs). To manage the queue of packets in these interfaces, a multi-link buffer management entity is used. The data-packets originating from these interfaces are routed through the redundant PNCs to the node P (Parent PNC) and ultimately to the packet gateway.

As discussed in Appendix A.1, the dependent PNCs in an SOP structure rely upon the parent PNC for a share of its channel time resources. Therefore, data-streams from all the redundant PNCs converge at node P where they are analysed using the PNC's buffer management entity and the reliability of different redundant link combinations is determined. The main steps in the process of buffer analysis at node P are shown in Fig. 4.3(b). During uplink, the process begins with the identification of redundant data-streams originating from each DEV and sequencing them in separate buffers for their reliability analysis. Following this, a link-reliability score corresponding to each of the redundant links and their various combinations are calculated using user-defined metrics and their

corresponding values are communicated back to the relevant DEV for regulating its redundancy levels. In the case of downlink transmissions, the same set of processes is undertaken at the buffer management entity of respective DEVs. Thus, based on the requirement for overall transmission reliability of a DEV, it selects a subset of the available redundant links for data-transmission.

To incorporate such architectures in real-life scenarios, the currently available mmWave transceiver modules operating on multi-element phased arrays can be used to communicate in the physical layer using multiple simultaneous beams, and the higher-layer tasks (e.g., buffer management, etc.) can be handled using appropriate driver-level upgrades (or using software-defined-radios). Indeed, the hardware prototyping platform for mmWave systems [73] offers multiple reconfigurable options to explore and evaluate new techniques and architectures.

To demonstrate the influence of link redundancy on transmission reliability, we consider Figs. 4.4(a) and (b). They show the percentage of successfully transmitted packets over blockage-prone links as a function of link redundancy for different transmission instances. From Fig. 4.4(a), it can be observed that, with an increase in redundancy levels, the percentage of successfully transmitted packets increases significantly. Similarly, from Fig. 4.4(b) it can be observed that with an increase in the number of redundant links, the reliability of the equivalent link, which is defined in terms of the mean percentage of successfully transferred packets improves at a linear rate.

4.3 DLLR Approaches for Controlling Link Redundancy

In this section, we discuss a framework for our system model and compare the effectiveness of our proposed approaches with respect to an unregulated form of MLC solution. Depending on their mode of implementation, DLLR solutions can be broadly classified as network centric or device centric methods. The details of each of these methods along with their merits and demerits are discussed below:

(i) **Device Centric methods of redundancy regulation (DC-DLLR)**: In this method, the member nodes within a piconet use the information available with them to regulate the extent of link redundancy. Since, data-packets either originate or terminate at the member nodes, this enables nodes to adapt their redundancy levels based on the reliability requirements of the underlying application.

(ii) **Network Centric methods of redundancy regulation (NC-DLLR)**: In this method, the

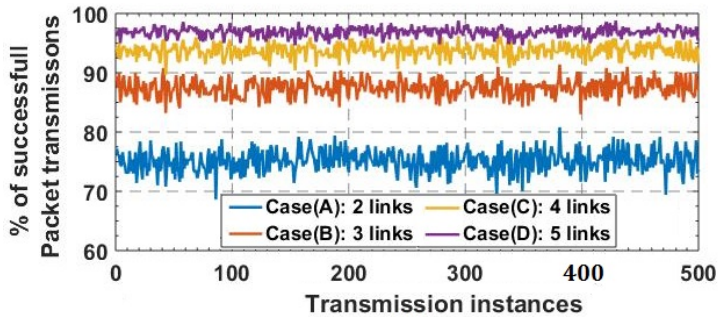

(a)

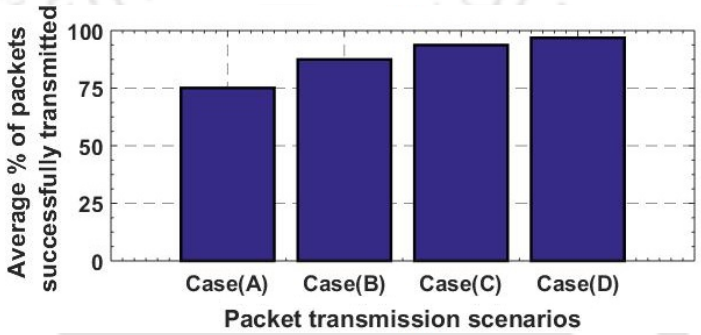

(b)

Figure 4.4: Effectiveness of link redundancy on transmission reliability over error prone channel

higher level network entities like the access point (AP) or the PNC determine the extent of link redundancy. Since they would typically be able to see more of the network and may also have access to various network-wide information, they are better suited to take decisions on redundancy control. In addition, these approaches are also more scalable in comparison to the device centric approaches. However, due to their distributed nature and various compatibility and security related constraints, these may be difficult to implement in practice.

In this thesis, we have focused only on the device centric approaches due to their ease of implementation.

4.3.1 System Model

We refer to the network model of Fig. 4.1(c), where an MLC architecture based on the IEEE 802.15.3c [72] supported SOP configuration is implemented. We assume that the access network is comprised of N member nodes (DEVs) where the individual nodes are denoted using n. The SOP configuration contains a set of $\overline{\mathcal{D}}$ child-PNCs where the individual PNC nodes are denoted using $\overline{\mathcal{D}} = \{\bar{d}_1, .., \bar{d}_i\}$. The child PNCs along with the parent PNC P operate together to provide network

coverage. The links connecting the parent and the dependent PNCs (i.e., the *self-backhaul links*), are denoted as $l_{\bar{d}_i,P}$. We assume that these are not affected by beam-blockage (and other such channel impediments) and suffer negligible packet losses. Similarly, considering an arbitrary member node n, the set of all links that connect the DEV with the redundant child PNCs is denoted using $l_{n,\bar{d}_i}$. Unlike the self-backhaul links, these links may get affected by beam blockage and other such channel impediments. To quantify the effect of beam-blockage in these links, a two-state channel model comprising of only the Line-of-sight and the outage states is generally used. Although, researchers have traditionally classified the state of the mmWave links as Line-of-Sight (LoS), Non-Line-of-Sight (NLoS) and Outage (Out) states respectively, the applicability of different fading models in each of these channel states (e.g., Rician Fading for LoS channel and Rayleigh Fading for NLoS channel) makes it difficult to have a unified model. Therefore, to have an integrated channel model which provides provisions for a more generalised form of channel-state representation, we use the Nakagami channel model of (4.1)

$$p_{z^2} = \left(\frac{m}{P_r}\right)^m \frac{x^{m-1}}{\Gamma(m)} \left(\frac{mx}{P_r}\right) \tag{4.1}$$

Here, P_r represents the average received power, $\Gamma(.)$ the Gamma function and (m), the fading parameter. Over a certain value for P_r, a fading parameter m (as defined in (4.2)) and the value of $p_z(x)$, (4.1) gives the probability that the instantaneous received envelope is greater than a given threshold z. Thus, by choosing an appropriate value for the parameter m, a channel model involving an arbitrary number of link states can be introduced.

$$m = \begin{cases} 1 & \text{Rayleigh Fading model} \\ \frac{(\kappa+1)^2}{(2\kappa+1)} & \text{Rician fading with parameter } \kappa \\ \infty & \text{No fading} \end{cases} \tag{4.2}$$

Here, depending on the choice of the model parameters (P_r,m and $p_z(x)$), different link-states are introduced and denoted using a set S_L where $S_L = \{s_{l_1}, s_{l_2}, .., s_{l_i}\}$. We similarly discretize the traffic associated with each of the DEV nodes into K different types and represent the individual traffic-types using $k = 1, .., K$ different intensities. For a mmWave channel having an SNR γ, with distribution $p(\gamma)$ and operating over a bandwidth B, the theoretical limit for the maximum data-rate C that can be sustained by the channel is given by *Shannon's Channel Capacity* equation of (4.3).

$$C = \int_0^\infty B \log_2(1+\gamma) p(\gamma) \partial\gamma \tag{4.3}$$

A member node n that intends to communicate at a traffic intensity k Mbps would require a certain signal-to-noise-ratio (SNR) threshold ($SNR^{Th}(k)$) to sustain that communication. Based on the values of different traffic intensities (k) and their respective SNR thresholds, the DEV maintains a mapping function as shown in TABLE-4.1. Similarly, for a given noise threshold (in dBm), each of the link

Table 4.1: Mapping Traffic types and SNR Threshold

Traffic Type	SNR Threshold
$k = 1$	$SNR^{Th}(1)$
..	..
$k = K$	$SNR^{Th}(K)$

states defined in S_L can also be mapped to an SNR threshold. Here, for a given link-state $s_{l_i} \in S_L$, its corresponding SNR threshold is denoted using $SNR^{Th}(s_{l_i})$. Then, based on the above mapping and the mapping between the SNR threshold and the traffic states (TABLE- 4.1), a quantitative score for each channel state is derived using (4.4).

$$\Phi\left(k, s_{l_i}\right) = \frac{\sum_{k=1}^{K} \mathbb{1}_k\left(s_{l_i}\right)}{K}.100\% \tag{4.4}$$

Here, $\Phi\left(k, s_{l_i}\right)$ denotes the channel quality score of the link and $\mathbb{1}_k\left(s_{l_i}\right)$, an identity function which is defined by:

$$\mathbb{1}_k\left(s_{l_i}\right) = \begin{cases} 1 & \text{if } SNR^{Th}\left(s_{l_i}\right) => SNR^{Th}\left(k\right) \\ 0 & \text{otherwise} \end{cases} \tag{4.5}$$

Thus, based on a time series of the varying link conditions, each of the redundant links $l_{n,\bar{d}_i}$ are quantified using their channel quality scores $\Phi\left(k, s_{l_i}\right)$. The DC-DLLR algorithms can then evaluate various combinations of redundant links under the SOP to select a subset PNC $\hat{\mathcal{D}} \subseteq \overline{\mathcal{D}}$ such that a desired grade of blockage reliability can be achieved. To measure the reliability statistics of different redundant link combinations, the parameters like mean number of blockage instances (μ) and their standard deviation (σ) are used. These parameters are evaluated and compared with respect to the corresponding system level performance thresholds $\{\mu_{Th}, \sigma_{Th}\}$.

4.3.2 Simulation Model

In our simulation model, we have used a MATLAB based simulator to replicate an indoor blockage environment. The setup consists of a rectangular 2D-space (resembling a room/hall) with a number of randomly placed rectangular objects (representing obstacles) of random length and breadth. A set

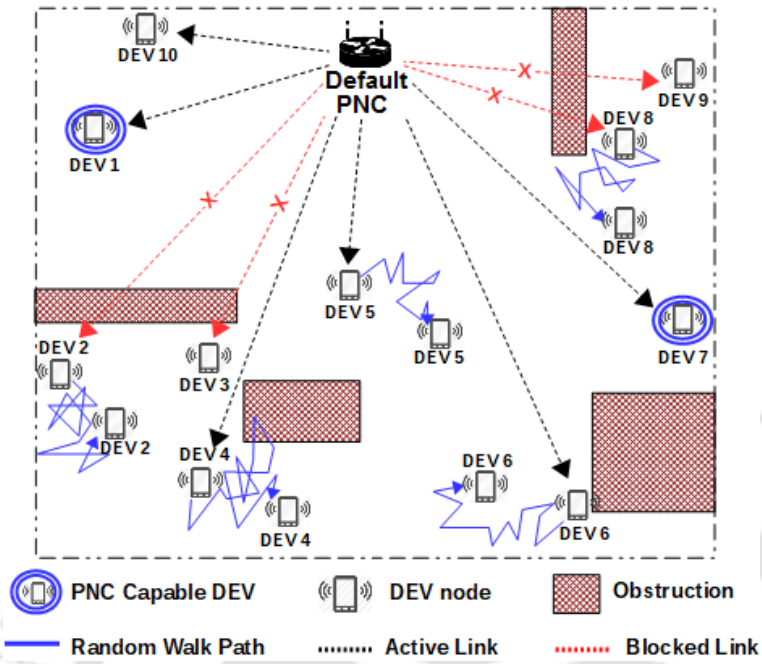

Figure 4.5: Simulation setup for a mmWave indoor blockage environment

Table 4.2: System Parameters

Parameter Name	Description
Room Dimension (scaled)	10 meter x 10 meter
Number of DEV Nodes	10
Distribution of DEV Position	Uniformly distributed in 2D plane
Number of Obstacles	4
Obstacle Length: 0 meter (Min.) - 2 meter (Max.) Obstacle Breadth: 0 meter (Min.) - 2 meter (Max.)	
Mobility Model Parameters	
DEV Mobility Pattern	Random-walk Model
Stride Length	1 meter
Rate of Steps	1 step/sec
Number of Steps	10

of DEVs are dropped in this space as shown in Fig. 4.5. Some of these nodes are static while the other nodes are made to change their location every second using a random walk model to replicate pedestrian mobility under indoor conditions. The details of all these user deployment and user mobility parameters are given in TABLE- 4.2.

With reference to Fig. 4.5, the parent PNC (i.e., default PNC) along with the set of PNC capable member nodes (i.e., DEV 1 and DEV 7) together provide SOP coverage. To evaluate beam blockages, we have used the NYUSIM tool [86] which is an open-source channel simulator for mmWave systems. It uses the distance between a pair of transceivers and that between the obstacles to calculate the

effective directional SNR at the receiver terminal. For an applied data-rate of k Mbps, if the received SNR falls below the corresponding SNR threshold (i.e., $SNR^{Th}(k)$), then the link is considered to be under outage. With the link states and their granularity as discussed in (4.1) and (4.2), we consider a simplified model which consists of only the LoS and the Outage states. Here, the set of link states i.e., S_L, is denoted as $S_L = \{s_{l_1}, s_{l_2}\}$. If a link is under outage, then none of the K traffic types will be supported (i.e., $\Phi(k, s_{l_i}) = 0$) whereas, if the link is under LoS condition then all the K traffic types will be supported (i.e., $\Phi(k, s_{l_i}) = 100$). To determine the ideal link combinations which can meet the desired reliability thresholds $\{\mu_{Th}, \sigma_{Th}\}$, we consider the following approaches:

(i) **Iterative Approach**: Here all the redundant link combinations are considered and evaluated sequentially and the one which first meets the desired performance threshold is selected. Following this, the total number of redundancy combinations (R) is a function of the number of PNCs in the SOP system and its value is expressed as:

$$R_{|\overline{\mathcal{D}}|} = \mathrm{C}_2^{|\overline{\mathcal{D}}|} + \mathrm{C}_3^{|\overline{\mathcal{D}}|} + .. + \mathrm{C}_{|\overline{\mathcal{D}}|}^{|\overline{\mathcal{D}}|} \tag{4.6}$$

In (4.6), the notation $\left|\overline{\mathcal{D}}\right|$ denotes the cardinality of the set $\overline{\mathcal{D}}$ and signifies the number of child PNCs in the SOP structure.

(ii) **Random Approach**: In this approach, different redundant link-combinations are tested randomly (following a uniform distribution) and the first combination to meet the desired performance threshold is selected.

(iii) **Conservative Approach**: In this approach, the initial redundant link-combination is the one with maximum number of redundant links. Subsequently, the algorithm evaluates lower link redundancy combinations by removing one link at-a-time and analyzing the performance with respect to the desired performance threshold.

(iv) **Heuristic Driven Approach**: Here, a combination of redundant links is selected using the heuristic driven approach of Algorithm 5. Compared to the other approaches, this can determine a redundant link combination for a given reliability threshold with fewer trials.

Algorithm 5: Heuristic approach for selecting redundant links

Input: Member nodes (n), Reliability threshold (μ_{Th}), Mean reliability scores ($\mu(l_{n,\bar{d}_i})$) of redundant links;

for *each member node* n **do**
  Process for Link Determination
  Fetch $\mu(l_{n,\bar{d}_i}) \; \forall \; l_{n,\bar{d}_i}$
  Find $l_{n,\bar{d}_i}^{Pivot} = \arg\underset{l_{n,\bar{d}_i}}{max} \left\{\mu\left(l_{n,\bar{d}_i}\right)\right\}$
  End Process
  if $\mu(l_{n,\bar{d}_i}^{Pivot}) > 0.75\mu_{Th}$ **then**
    Evaluate all 2-link redundancies including $l_{n,\bar{d}_i}^{Pivot}$
    Select 1^{st} configuration s.t. reliability score $> \mu_{Th}$
  else if $0.5\mu_{Th} < \mu(l_{n,\bar{d}_i}^{Pivot}) <= 0.75\mu_{Th}$ **then**
    Evaluate all 3-link redundancies including $l_{n,\bar{d}_i}^{Pivot}$
    Select 1^{st} configuration s.t. reliability score $> \mu_{Th}$
  else if $\mu(l_{n,\bar{d}_i}^{Pivot}) <= 0.5\mu_{Th}$ **then**
    Evaluate all 4-link redundancies including $l_{n,\bar{d}_i}^{Pivot}$
    Select 1^{st} configuration s.t. reliability score $> \mu_{Th}$

4.4 Result and Analysis

We evaluate the performance of each of these approaches with respect to various parameters e.g., the number of trials required to meet a given performance threshold as a function of different system configurations, share of the redundant infrastructure used under each of the approaches etc. We discuss the results obtained for each of these parameters next.

Effect of system complexity on the number of link-combination trials: In this case, we have evaluated the effect of different piconet configurations (i.e., with respect to varying node and obstacle densities) on the number of iterations required to achieve a certain reliability threshold. To analyse the results, we have used the reliability threshold of $\mu_{Th} = 0.9$ and $\sigma_{Th} = 0.1$ respectively and applied the iterative approach for DLLR. In Fig. 4.6, we calculate the results for over 300 different deployment scenarios and plot the average number of iterations required to arrive at the desired threshold for each of these system configurations.

As expected, Fig. 4.6(a) shows that for smaller system sizes, the desired reliability scores can be achieved with fewer iterations than for larger systems. Similarly, Fig. 4.6(b) shows that as the system size increases, the mean number of trials required to meet the desired performance threshold

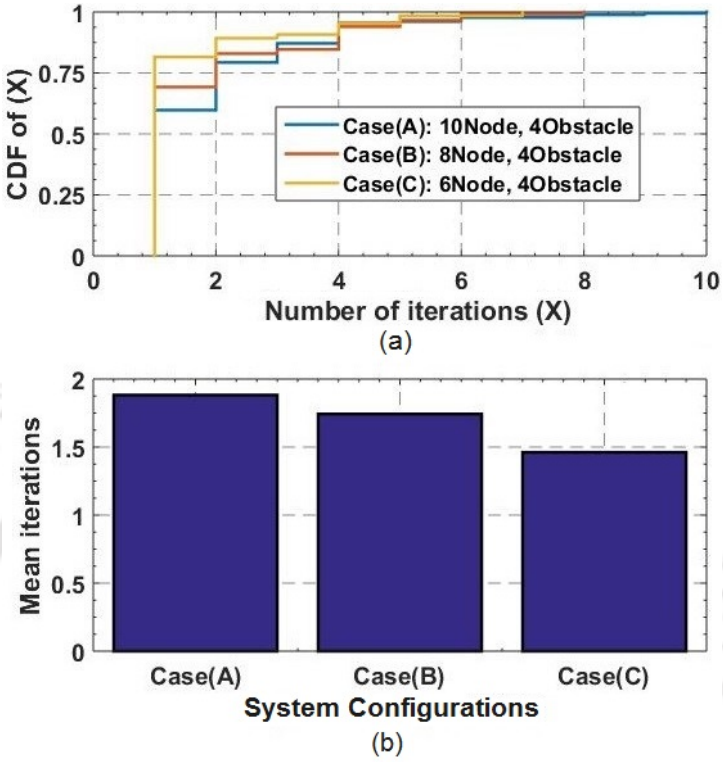

Figure 4.6: Variation in number of iterations required to find desired redundancy as a function of different system configurations; (a) CDF of number of iterations; (b) Mean number of iterations under each configuration

also increases proportionately.

Performance of DC-DLLR algorithms over varying reliability thresholds: Here, we compare the efficacy of the different DC-DLLR algorithms in terms of the probability of their finding an acceptable link combination for a given reliability threshold. Since, different types of DC-DLLR algorithms arrive at a desirable link combination using varying number of trials, this type of characterization can be considered as a measure of the time-complexity for each of the proposed algorithms. Approaches with a higher probability of finding an acceptable redundancy option in a given trial would be more agile in comparison to other approaches. Fig. 4.7 shows that for a given reliability threshold μ_{Th}, the heuristic algorithm has the highest probability of finding an acceptable solution followed by the random approach, the conservative approach and lastly the iterative approach. Moreover, since the number of viable redundancy options goes down with increasing μ_{Th}, it can be observed that the probability of finding an acceptable solution decreases with increasing reliability threshold for all the algorithms.

Distribution of redundancy levels over different approaches: Fig. 4.8 shows the distri-

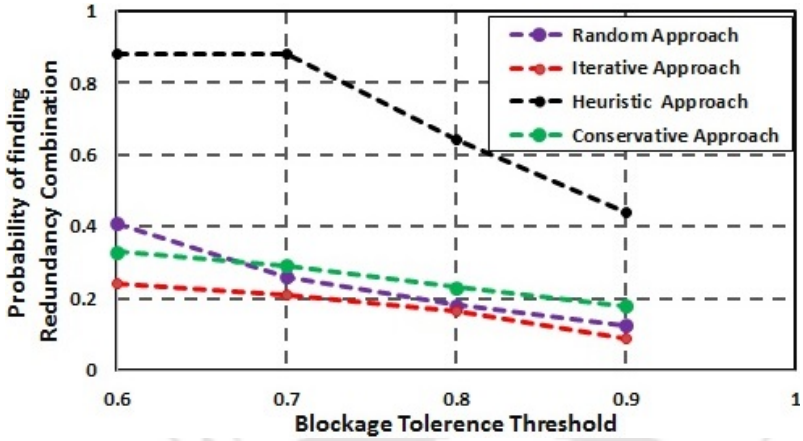

Figure 4.7: Comparison of different DC-DLLR approaches with respect to their μ_{Th} in a given trial probability for achieving different reliability threshold

bution of link redundancies for different types of DC-DLLR approaches. It can be observed that link redundancies with four links have a marginal share in the overall distribution of links for all the approaches except the random approach. This indicates that very high levels of redundancies (4 and above) are rarely required to achieve very high levels of connection reliability. From Figs. 4.8(a),(c) and (d)(i.e., for the iterative, random and the heuristic approaches), we also see that the two-link based redundancy systems have a major share in the total distribution of links. However, for the conservative approach (Fig. 4.8(b)), it can be observed that a majority of the instances have three-link redundancy. This can be attributed to the fact that the conservative approach starts with the highest levels of redundancy and iteratively reduces the redundancy levels while complying with the μ_{Th} requirements.

Distribution of unused links in DC-DLLR in comparison to unregulated MLC solution: As observed earlier in reference to Fig. 4.8, each of the DC-DLLR approaches achieves the desired reliability threshold using a different distribution of link level redundancies. Therefore, in Fig. 4.9, we compare their performances with reference to an un-regulated form of MLC solution which operates using a fixed redundancy of four links. Correspondingly, Fig. 4.9 shows the percentage of unused links for each of these approaches. It can be observed that the iterative and the heuristic approaches achieve the desired redundancy threshold with the maximum number of unused links. Since, the magnitude of unused links is also an indicator of energy efficiency, it can be inferred that the iterative and the heuristic approaches are the most efficient while the conservative approach is the least efficient.

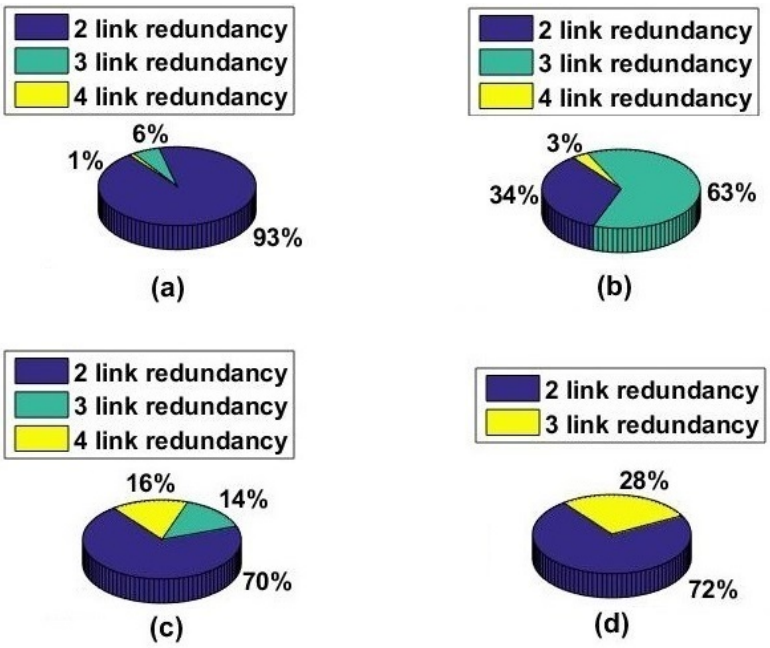

Figure 4.8: Distribution of link-redundancy levels under different types of devices centric DLLR approaches (a) Iterative approach; (b) Conservative approach; (c) Random approach; and (d) Heuristic approach

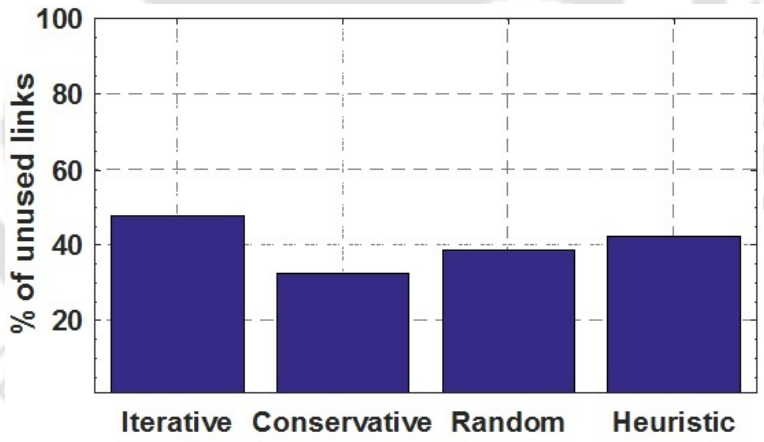

Figure 4.9: Comparison of different algorithms with respect to the percentage of unused links in reference to the unregulated (static) redundancy approach

4.5 Conclusion

In this Chapter, we have discussed various device-centric approaches for regulating link redundancy. It was demonstrated that by employing an MLC framework for link redundancy, the effect of beam blockage in a mmWave system can be mitigated and reliable performance can be achieved with lower utilization of redundant infrastructure. It was also observed that the efficiency of these algorithms

to fulfil a certain reliability criterion is dependent on the size of the system. By introducing different types of DC-DLLR algorithms, it was demonstrated that their ability to arrive at a link combination corresponding to certain reliability measure is dependent on the type of algorithm used. It was also inferred that the DLLR approaches can be used to significantly improve the resource utilization of an MLC network by minimizing its usage of redundant links.

5

Resource Allocation in mmWave Based SOP Architectures

Contents

This chapter presents different techniques to address the issue of blockage-induced resource misallocation in mmWave networks. The proposed techniques are based on the simultaneously operating piconet (SOP) architecture (operating on IEEE 802.15.3c MAC standard [72]) and use two different methodologies to achieve efficient resource allocation. In the first method, a feedback driven mechanism is used to address the issues of over/under allocation of network resources whereas the second method applies a portfolio-theory based risk-sensitive model to achieve optimal resource allocation. The results obtained using extensive simulation trials have validated that these techniques can be used to effectively allocate network resources in a mmWave network operating under blockage-prone conditions.

5.1 Introduction

The mmWave access networks operating on the IEEE 802.15.3c based SOP architecture offer a reliable and effective means to run high data-rate IoT networks while overcoming the shortcomings of beam-blockage and small coverage range which characterizes these systems. The SOP architecture involves a dense network of mmWave piconet controllers (PNCs) which coordinate among themselves to provide redundant coverage. As discussed in Appendix A.1, the resource allocation mechanism in an SOP structure consists of several dependent PNCs connected to a parent PNC in a hierarchical fashion where the dependent PNCs rely on the parent PNC for a share of its channel-time resources. Thus, depending on the requirement of channel-time in each of the dependent piconets, the parent PNC distributes its resources using periodically updated pseudo-static-channel-time allocations (p-CTAs).

However, due to the dynamic nature of the network, the p-CTA demand at the constituent piconets would change over time. For instance, during the addition or removal of one or more piconets from the SOP structure, the corresponding p-CTA allocation would require updation. Similarly, due to changing blockage conditions or due to the mobility of the member nodes the requirement of p-CTA at the constituent piconets may vary with time. Thus, a robust mechanism for the assignment of network resources has to be developed.

Hence, in this chapter, we propose and present two different methods to determine the distribution of p-CTA resources between the member piconets. In the first method, the parent PNC obtains channel-time utilization data from the child PNCs and ranks them based on their efficiency. Subsequently, it uses a weighted algorithm to determine the allotment of p-CTA among the member

piconets. Under the second methodology, the Portfolio Allocation based Channel Time Assignment (PACTA) technique is discussed. It considers the SOP structure as a portfolio of assets and models the p-CTA allocation problem as an optimization problem involving multiple QoS parameters. By using a model based on Markowitz's Portfolio Allocation Theory [81], it dynamically determines the ideal p-CTA allocation such that the risk of return fluctuations over the allocated resources is minimized while still maintaining acceptable returns. The salient features of these approaches are as follows:

(i) They help in improving the efficiency and fairness of resource allocation in mmWave SOPs and contribute towards service reliability and energy efficiency.

(ii) They are especially useful for blockage-prone indoor conditions where the demand for network resources changes abruptly.

(iii) The objective function of the optimization model (in case of PACTA approach) can be suitably adapted to different performance criteria and reconfigured based on the preferences of the network operator.

5.2 Description of the p-CTA Assignment Framework

In this section, we describe the p-CTA allocation framework for a mmWave SOP structure and assume the following: (a) the number of layers in the SOP hierarchy is limited to two i.e., the layer containing the parent PNC and its sub-layer containing the set of all dependent PNCs; (b) the parent and the dependent PNCs are arranged only in the form of a parent-child hierarchy; and (c) there is a one-to-one mapping between a DEV and its serviced PNC. With regard to the first assumption,although the IEEE 802.15.3c standard can accommodate multiple layers of SOP hierarchy, but the inclusion of each new sub-layer causes additional latency. Thus, in view of the problem of blockage-mitigation, only two layered SOP hierarchies are considered. For the second assumption, although the SOP structure supports both the parent-child (p/c) and parent-neighbour (p/n) hierarchies, the (p/c) hierarchy ensures that the complete network capacity is available to meet the transmission requirements of the serviced piconet.

In Fig. 5.1, the depicted network architecture demonstrates the generalized structure of a mmWave access network operating in SOP architecture. It consists of several dependent PNCs connected to a parent PNC using a p/c hierarchy where the member nodes (DEVs) connected to the individual

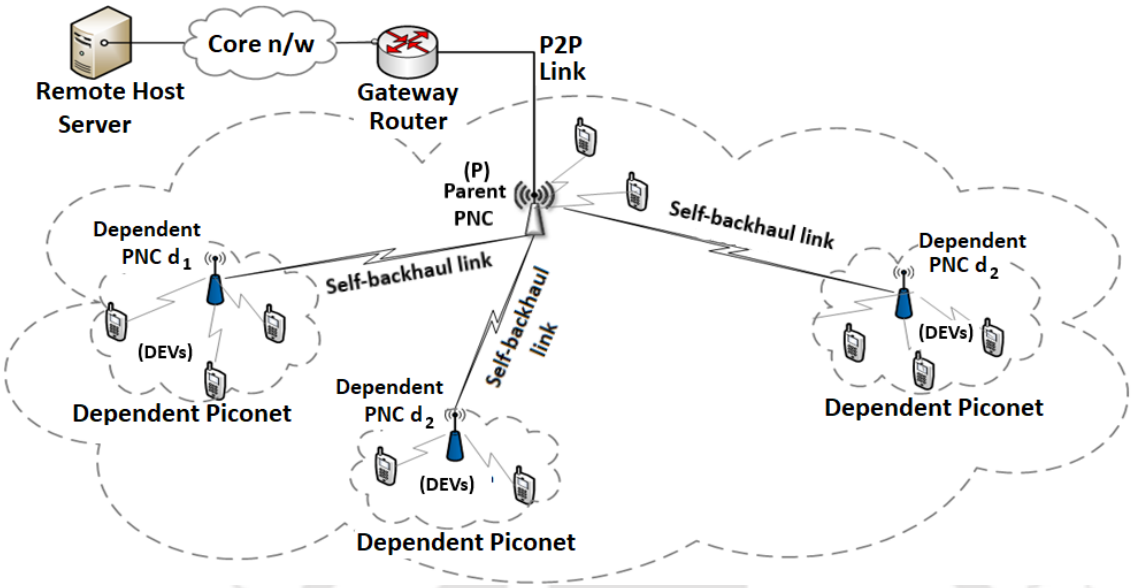

Figure 5.1: Hierarchical structure of a mmWave network connected in SOP architecture

PNCs get serviced. As per the standard, the DEVs in each piconet communicate their transmission requirements to their attached PNC using channel time access (CTA) requests. These requests can either be in the form of an isochronous CTA (i.e., CT^{Iso}) or in the form of an asynchronous CTA (i.e., CT^{Asy}). For the CT^{Iso} requests, a DEV demands a fixed amount of CTA resource with a certain servicing frequency (periodicity) from its associated PNC whereas, in case of the CT^{Asy} requests, the DEV intermittently requests for a random amount of CTA allocation based on its application requirements. At the dependent PNC's level, all the CT^{Asy} and CT^{Iso} requests (as generated by the associated DEVs) are consolidated and the overall channel-time demand is communicated to the parent PNC as a p-CTA request. Unlike the frequent CT^{Asy} and CT^{Iso} requests, the pseudo-static/private CTA (p-CTA) allocation requests are communicated occasionally and generally involve re-allocation of the network resources (channel-time) by the parent PNC. The process followed by the parent PNC to distribute its network resources between multiple dependent PNCs is discussed in Appendix A.1. However, as these adjustments occur much less often in comparison to that of the changes in device level CTA requirements (CT^{Iso} and CT^{Asy}), there is always a mismatch between the requested and the assigned values of p-CTA. As a result, the following may occur:

(i) If the assigned p-CTA is greater than the p-CTA demand, then a part of the allocated channel-time would remain unused and would lead to the wastage of network capacity.

(ii) If the assigned p-CTA is less than the demanded p-CTA, then some of the member nodes would not be able to communicate and would lead to issues of unfair resource allocation and unreliable service.

5.3 Proposed p-CTA Distribution Approaches

In this section, we discuss our proposed resource allocation approaches which aim to address the above discussed issues. Firstly, we describe the feedback driven approach and discuss some of its limitations. Thereafter, we discuss a risk-sensitive approach which is more improved in comparison to the feedback approach and aims to resolve some of its shortcomings.

5.3.1 Feedback Driven Approach

We discuss this approach using the network model of Fig. 5.1, where a set of N member nodes which are serviced by a mmWave SOP structure (operating on the IEEE 802.15.3c MAC standard). The individual member nodes (DEVs) in N are denoted using n and parameters P, $\mathcal{D}$ denote the parent PNC and the set of all PNC capable nodes in the piconet. Since, only the PNC capable DEVs can operate as dependent PNCs, the set of all child PNCs in the SOP is denoted using $\overline{\mathcal{D}}$ where $\overline{\mathcal{D}} \subseteq \mathcal{D}$. As the association status of a dependent PNC with respect to the node P varies with time, we introduce a variable $a_{\bar{d}_i,P}(t)$ to denote the state of association of a dependent PNC $\bar{d}_i \in \overline{\mathcal{D}}$ with respect to the PNC P for the superframe (t). Accordingly, $a_{\bar{d}_i,P}(t)$ is defined as:

$$a_{\bar{d}_i,P}(t) = \begin{cases} 1, & \text{if } \bar{d}_i \text{ is associated to } P \text{ at SF } (t) \\ 0, & \text{otherwise} \end{cases} \tag{5.1}$$

In a similar way, the association status of a member node n with respect to the PNCs in the SOP can be expressed using $a_{n,P}(t)$ or $a_{n,\bar{d}_i}(t)$. Since, we have assumed a one-to-one mapping between a PNC and its serviced DEV, the constraint in (5.2) is applicable:

$$a_{n,P}(t) + \sum_{i=1}^{|\bar{\mathcal{D}}|} a_{n,\bar{d}_i}(t) = 1 \tag{5.2}$$

As per [72], the member nodes in an SOP can request for various asynchronous or isochronous CTA slots from its associated (parent/dependent) PNC using parameters like *Channel Time Request TU* (Transmission Unit) which corresponds to the service duration, *CTA Rate Factor* (corresponding to

the frequency of service) and *CTA Type* (to specify if the requested CTA is pseudo-static or dynamic). In addition, the nature of these service specifications may also vary with time. Thus, for the sake of simplicity, we assume that each DEV requires to be serviced by its associated PNC in every SF and that the distribution of these service durations is known to its attached PNC based on the historical data. Assuming that each node $n \in N$ requires a mean service duration of e_n msec, the overall demand of service time at each of the PNCs due to the set of its associated DEVs is given by:

$$L_P(t) = \sum_n a_{n,P}(t).e_n \tag{5.3a}$$

$$L_{\bar{d}_i}(t) = \sum_n a_{n,\bar{d}_i}(t).e_n \tag{5.3b}$$

In (5.3), the parameters $L_P(t)$ and $L_{\bar{d}_i}(t)$ are indicative of the overall load (CTA demand) at the PNCs P and $\bar{d}_i$ respectively. Therefore, the total load $L(t)$ on the SOP structure can be evaluated using the summation of CTA demands at each of the PNCs i.e.:

$$\begin{aligned} L(t) &= \sum_i L_{\bar{d}_i}(t) + L_P(t) \\ &= \sum_i \left(\sum_n a_{n,\bar{d}_i}(t).e_n \right) + \sum_n a_{n,P}(t).e_n \end{aligned} \tag{5.4}$$

As discussed in Appendix A.1, the CTA demands at each of the child PNCs $\left(L_{\bar{d}_i}(t)\right)$ are communicated to the parent PNC in form of p-CTA requests. The parent PNC upon receiving the requests tries to allocate the necessary resources by reserving a part of its CTA duration for a particular child PNC. In this way, the parent PNC partitions its total CTA duration to facilitate usage by various child PNCs in the SOP. To account for the share of total CTA that is allocated for a particular PNC, we introduce the notion of CTA weightages. Accordingly, we define the parameters $w_P(t)$ and $w_{\bar{d}_i}(t)$ to denote the fraction of CTA duration that is reserved for the parent PNC and each of its child PNCs. The magnitude of these weightages are constrained by the following conditions:

$$0 \leq w_P(t) \leq 1 \tag{5.5a}$$

$$0 \leq w_{\bar{d}_i}(t) \leq 1 \tag{5.5b}$$

$$\sum_i w_{\bar{d}_i}(t) + w_P(t) = 1 \tag{5.5c}$$

By assigning these weightages to the average CTA demands of the PNCs, the total channel time utilization of the SOP structure can be obtained. Accordingly, in (5.6) we introduce the parameter

Algorithm 6: p-CTA Distribution in SOPs during addition/removal of PNC

Input: IEEE 802.15.3c reference superframe (t); Set of PNC capable DEVs $\mathcal{D}$; Total CTA duration in a SF (T_{CTA}); Association status of nodes $d_i \in \mathcal{D}$ w.r.t P i.e. ($a_{d_i,P}(t)$)

Initialize p-CTA weights for the parent and child PNCs i.e. $w_P(t) = 0$ and $w_{\bar{d}_i}(t) = 0$
procedure: DETERMINE TOTAL ACTIVE CHILD PNCs AT (t)
if *new request for p-CTA allocation/deallocation received at* P **then**
    for *each node* $d_i \in \mathcal{D}$ **do**
        if $a_{d_i,P}(t) = 1$ *and p-CTA* $(d_i, t) > 0$ **then**
            add d_i in set $\overline{\mathcal{D}}$
        else
            goto step-4
    else
        set $w_P(t) = w_P(t-1)$; and $\forall \bar{d}_i \in \overline{\mathcal{D}}$, set $w_{\bar{d}_i}(t) = w_{\bar{d}_i}(t-1)$
end procedure
Assign p-CTA weightages $w_P(t) = \frac{1}{(|\overline{\mathcal{D}}|+1)}$; $w_{\bar{d}_i}(t) = \frac{1}{(|\overline{\mathcal{D}}|+1)}$
Channel-time for PNC P: $T_{CTA}.w_P(t)$
Channel-time for PNC $\bar{d}_i$: $T_{CTA}.w_{\bar{d}_i}(t)$

$U_{CTA}(t)$ and use it to define the channel time utilization of an SOP structure.

$$U_{CTA}(t) = \left(\sum_i \left(\sum_n a_{n,\bar{d}_i}(t).e_n\right).w_{\bar{d}_i}(t)\right) + \left(\sum_n a_{n,P}(t).e_n\right) w_P(t) \tag{5.6}$$

In order to fully utilize the capacity of the SOP structure, a judicious assignment of the p-CTA weightages is necessary. In scenarios where the addition or removal of a PNC from the SOP is involved, the prospective p-CTA demand on the new set of PNCs is not known apriori to the parent PNC. Therefore, the feedback driven approach uses Algorithm 6 to determine the p-CTA weightages. Under the approach, the parent PNC first evaluates the association status of each of its child PNCs along with their p-CTA allocation. If an associated PNC-capable neighbour is found to have a non-zero allocation of p-CTA, then it is considered to be a part of the SOP. Thereafter, the parent PNC uniformly partitions its CTA slot (depending on the number of PNCs in the SOP) and assigns them to the child PNCs to accommodate their transmission requirements. It also retains an equally sized slot for itself to facilitate its internal transmissions.

Hence, for a given SOP hierarchy, if one or more PNCs demand for a revision of their existing p-CTA allocation(s), then the parent PNC uses Algorithm 7 to determine their revised channel-time weightage(s). This type of resource re-arrangement is more common in blockage prone scenarios, where beam-blockage induces abrupt changes in node associations and leads to frequent changes in

Algorithm 7: Rearrangement of p-CTA allotment in SOPs for a given set of PNCs

Input: IEEE 802.15.3c reference superframe (t); Set of Dependent (Child) PNCs ($\overline{\mathcal{D}}$); Total CTA duration in a SF (T_{CTA}); Association status for various types of nodes (i.e. $a_{n,P}(t)$,$a_{n,\bar{d}_i}(t)$ and $a_{\bar{d}_i,P}(t)$); Mean CTA demand of each DEV n (e_n)

Initialize total load on child PNCs to zero (i.e. $Sum(L_{\bar{d}_i}(t)) = 0\ \forall \bar{d}_i \in \overline{\mathcal{D}}$)
Calculate $L_P(t)$ using (5.3(a))
for *each node* $\bar{d}_i \in \overline{\mathcal{D}}$ **do**
    Calculate $L_{\bar{d}_i}(t)$ using (5.3(b))
    $Sum(L_{\bar{d}_i}(t)) = Sum(L_{\bar{d}_i}(t)) + L_{\bar{d}_i}(t)$
Calculate $L(t)$ using (5.4)
p-CTA weightage $w_P(t) = \frac{1}{L(t)}.L_P(t)$
p-CTA weightage $w_{\bar{d}_i}(t) = \frac{1}{L(t)}.L_{\bar{d}_i}(t)$
Channel-time for PNC P: $T_{CTA}.w_P(t)$
Channel-time for PNC $\bar{d}_i$: $T_{CTA}.w_{\bar{d}_i}(t)$

p-CTA allocations. Under this approach (Algorithm 7), the parent PNC first evaluates the total CTA requirement of its associated nodes and that in each of its child PNCs. Thereafter, it determines the normalized share of p-CTA demand in each of the PNCs and assigns them a channel-time weightage corresponding to their relative magnitudes.

5.3.2 PACTA Approach

The feedback driven technique adopts a reactive approach for the adjustment of channel-time resources in an SOP structure and operates by updating the p-CTA distribution, whenever there is a change in the channel-time demand at the PNCs. However, under practical conditions, the state of an SOP (and hence the p-CTA requirement at its PNCs) keeps changing dynamically due to the influence of several factors e.g., node mobility, beam-blockage and the inherent changes in transmission requirements of the connected DEVs. Therefore, the distribution of p-CTA weightages would require frequent adjustments. Moreover, the approach ignores the influence of several other factors e.g., the mean rate of increase or decrease in node associations due to node mobility, nature of CTA demands (CT^{Iso}, CT^{Asy}) and beam-blockage which can potentially influence the p-CTA demand of an SOP. Rather, it lumps the effect of all factors as a load re-arrangement event. Hence, to address these issues, we present the PACTA approach.

Unlike the feedback driven approach, this approach adopts a proactive model for p-CTA allocation. It assigns channel-time weightages based on the SOP's behaviour and takes into consideration multiple

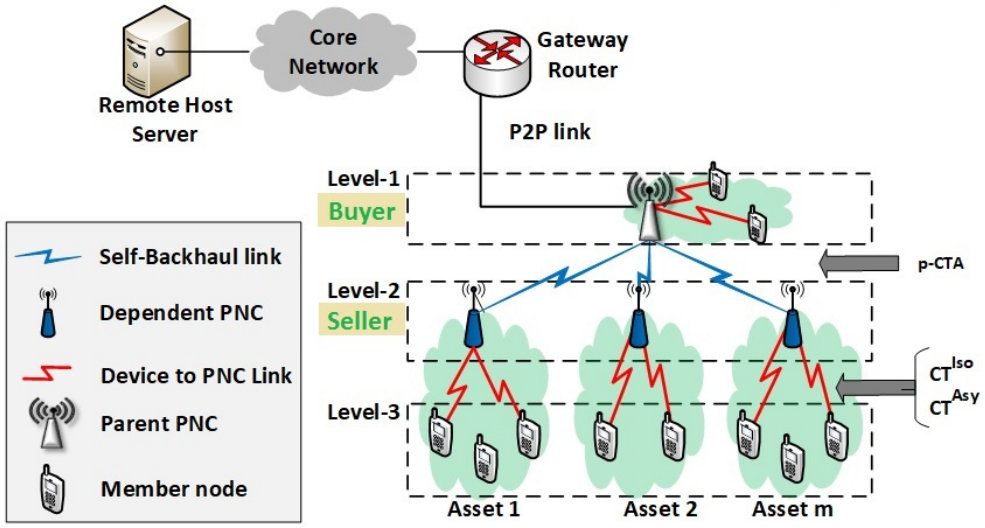

Figure 5.2: Buyer seller paradigm for p-CTA distribution in mmWave SOP architecture

system parameters that influence p-CTA demand. It is more suitable for dynamic network conditions and does not involve frequent p-CTA re-arrangements (as in the case of the feedback driven approach). As shown in Fig. 5.2, the approach formulates the problem of p-CTA distribution as a portfolio allocation problem where all dependent piconets of an SOP are viewed as *assets* in a portfolio. In each of the assets, the dependent PNC is considered as a *seller* as it offers to use a part of the CTA from the parent PNC. The parent PNC is the resource allocator (*buyer*) and is responsible for p-CTA allocation over the assets. The buyer aims to minimize the risk of p-CTA misallocation in the portfolio while maximizing its returns.

In terms of the system model, the PACTA approach follows the network structure as in the case of the feedback driven approach where a group of N member nodes are serviced by a set of child PNCs $\overline{\mathcal{D}} = \{\overline{d}_1, .., \overline{d}_i\}$. The child PNCs are connected to the parent PNC through *self-backhaul* links $l_{\overline{d}_i,p}$ and the parent PNC further connects them to the packet-gateway through a point-to-point (P2P) backhaul link. Under this configuration, the number of assets M in an SOP portfolio is defined as the total number of operated piconets (including the parent and the dependent piconets) i.e., $M = \left(\left|\overline{\mathcal{D}}\right| + 1\right)$ where $\left|\overline{\mathcal{D}}\right|$ denotes cardinality of the set $\overline{\mathcal{D}}$. The individual assets in M are denoted using m_i where $i = \{1, .., M\}$. In each of these assets, the overall CTA demand is a combination of the total channel-time requirements (CT^{Iso}, CT^{Asy}) of the associated nodes. However, the magnitude and distribution of these components are influenced by several qualitative (QoS) factors as considered in TABLE-5.1. Although, the network operator can consider any number of MAC-layer parameters as QoS factors,

in this model, we arbitrarily choose K such factors for each asset m_i and denote the set of all such p-CTA influencing QoS factors using $\Im_{m_i} = \{f_{1,m_i}, .., f_{K,m_i}\}$. Moreover, as parameter values in $\Im_{m_i}$ vary with time, we represent $\Im_{m_i}$ in terms of the reference SF (t_r).

$$\Im_{m_i}(t_r) = \{f_{1,m_i}(t_r), .., f_{K,m_i}(t_r)\} \tag{5.7}$$

Table 5.1: Elements of asset parameter set $(\Im_{m_i})$ under PACTA model

QoS Factor	Description
$f_{1,m_j} = l_{m_j,P}$	State of the self-backhaul link connecting, each PNC in asset m_j to the parent PNC P
$f_{2,m_j} = n_{m_j}$	Number of connected nodes in asset m_j
$f_{3,m_j} = CT^{Asy}_{m_j}$	Total Asynchronous CTA demand in asset m_j
$f_{4,m_j} = CT^{Iso}_{m_j}$	Total Isochronous CTA demand in asset m_j
$f_{5,m_j} = \lambda^{arr}_{m_j}$	Mean rate of increase in connected nodes (mobility or blockage induced) in asset m_j
$f_{6,m_j} = \mu^{dep}_{m_j}$	Mean rate of decrease in connected nodes (mobility or blockage induced) in asset m_j

Assuming (5.7) to be an exhaustive set of p-CTA influencing factors, the overall qualitative score $Q_{m_i}(t_r)$ of each asset m_i is evaluated using the combined effect of factors in (5.7). Therefore, based on the network operator's preferences, a fraction ψ_k (as shown in TABLE-5.2) is assigned to each of the factors $f_{k,m_i} \in \Im_{m_i}(t_r)$ to denote its relative contribution towards the overall QoS score $Q_{m_i}(t_r)$ of the asset (i.e., $\sum_{k=1}^{K} \psi_k = 1$ for $\psi_k \in (0,1)$). Thus, the value of $Q_{m_i}(t_r)$ is expressed as:

$$Q_{m_i}(t_r) = \sum_{k=1}^{K} \psi_k . f_{k,m_i}(t_r) \tag{5.8}$$

On the *buyer's* side (i.e., level-1 from Fig. 5.2), the parent PNC evaluates $Q_{m_i}(t_r)$ values for each of the contending assets and allocates a fraction $w_{m_i}(t_r)$ of its total CTA resource towards each asset (i.e., $\sum_{i=1}^{M} w_{m_i}(t_r) = 1$ for $w_{m_i}(t_r) \in (0,1)$). Hence, depending upon the parameter $Q_{m_i}(t_r)$ and its allocated p-CTA weightage $w_{m_i}(t_r)$, the Qualitative score of the SOP portfolio $Q^P(t_r)$ is denoted by:

$$\begin{aligned} Q^P(t_r) &= \sum_{i=1}^{M} w_{m_i}(t_r) . Q_{m_i}(t_r) \\ &= \sum_{i=1}^{M} w_{m_i}(t_r) . \left(\sum_{k=1}^{K} \psi_k . f_{k,m_i}(t_r) \right) \end{aligned} \tag{5.9}$$

In (5.9), the magnitudes of asset scores $Q_{m_i}(t_r)$ can change randomly with time due to variation in the $f_{k,m_i}(t_r)$ parameters. Therefore, the *buyer* (parent PNC) needs to assign resources ($w_{m_i}(t_r)$ values) such that, the p-CTA requirements of all assets are met while avoiding over or under-allocation

of resources. However, unlike $f_{k,m_i}(t_r)$ values which change with every (t_r), the pseudo-static p-CTA adjustments (weightage re-allocations) are done less frequently (as discussed later in (5.11)). Therefore, the task of the resource allocator involves achieving an acceptable $Q^P(t_r)$ score for the portfolio while minimizing the instances of resource mis-allocations. Hence, we use the Markowitz's model of portfolio allocation as discussed in Appendix A.2. It provides a generalized solution for the determination of an ideal weightage vector (w^*) that can reduce the volatility in a portfolio of random variables. For the PACTA approach, we intend to find an optimal p-CTA distribution which minimizes the extent of mismatch between the assigned and utilized p-CTAs. Hence, we parameterize each of the assets in terms of set $\Im_{m_i}(t_r)$ in TABLE-5.1 and use the corresponding asset QoS scores as input to the earlier discussed model.

Considering the factors from TABLE-5.1, f_{1,m_i} corresponds to the state of the self-backhaul link $l_{m_j,P}$. It is defined in terms of Line of sight (LoS), Non-line of sight (NLoS) and Outage states as discussed in [14].

$$l_{m_j,P} = \begin{cases} 1, & \text{if link from asset } m_j \text{ to PNC } P \text{ is in LoS/NLoS state} \\ 0, & \text{otherwise} \end{cases} \tag{5.10}$$

Since blockage of this link can stop all uplink and downlink traffic for an asset, the outage probability of this link is considered as a vital parameter for p-CTA allocation. For the parameter f_{2,m_j} i.e., the number of connected nodes, assets with a larger number of connected nodes are more likely to experience fluctuations in p-CTA demand. Hence, we consider it to be a p-CTA influencing factor. Similarly, the factors f_{3,m_j} and f_{4,m_j} together constitute the total p-CTA demand of an asset; and hence, they are considered vital for determining p-CTA allocation. Finally, for the factors f_{5,m_j} and f_{6,m_j}, they determine the dynamic rate of increase or decrease in the node-count of an asset due to node mobility. Their ratio is used to determine the trend of increase or decrease in p-CTA demand of an asset. Hence, we consider these as a vital p-CTA influencing factor. The PACTA model uses these factors to achieve optimal p-CTA distribution as follows:

5.3.2.1 p-CTA Distribution for an SOP with Fixed Set of Assets

In this case, the tasks are executed at two different levels as shown in Algorithm 8. At the asset level (seller), each of the dependent PNCs use (5.8) to evaluate their QoS scores $Q_{m_i}(t_r)$ by using the TABLE-5.1 parameters and update this information in the regulator database which is hosted

Algorithm 8: Calculation of optimal CTA weightage $w^*_{m_j}(t_r)$

Input: Reference superframe IEEE 802.15.3c (t_r), Asset parameters ($\Im_{m_j}$), Asset parameter weightages (ψ_k), CTA lower bound (μ_b), p-CTA weightages ($w^*_{m_j}(t)\ \forall t = \{1, .., t_{r-1}\}$);

procedure: UPDATE REGULATOR DATA // At seller side
for *each superframe* t_r **do**
  for *each asset* m_j **do**
    Fetch QoS parameter set $\Im_{m_j}(t_r)$
    Calculate asset scores $Q_{m_j}(t_r)$ using ψ_k in (5.8)
    Upload $Q_{m_j}(t_r)$ data in regulator database
end procedure
procedure: FIND OPTIMAL WEIGHTS // At buyer side
for *each superframe* t_r **do**
  for *each asset* m_j **do**
    Fetch data $Q^{Hist}_{m_j} = \{Q_{m_j}(t_1), .., Q_{m_j}(t_{r-1})\}$
    Evaluate r_{m_j} by using $Q^{Hist}_{m_j}$ (Appendix A.2)
    Generate $\Re$ and evaluate Θ and Σ parameters
  Using $\{\mu_b, \theta, \Sigma\}$, find $w^*_{m_j}(t_r)$ by applying Markowitz's optimization model
end procedure

at the parent PNC. In the parent PNC's level (buyer), these historical QoS scores are accessed to generate a time-series of asset returns r_{m_i} as discussed in Appendix A.2. These values are later used to formulate the $\Re$ matrix and the Θ, Σ parameters and finally used in the Markowitz's optimization model (Appendix A.2) to generate the ${w^*}_{m_j}$ values. To avoid frequent weightage re-allocations, the PACTA approach uses a portfolio threshold Q^P_{Th} and compares it with the optimized qualitative score $Q^P_{Opt}(t_r)$ of the portfolio. Here, $Q^P_{Opt}(t_r)$ is calculated by solving (5.9) while using the total CTA values as per ${w^*}_{m_j}$. Finally, the decision to trigger p-CTA re-allocation is determined by solving (5.11).

$$Q^P_{Opt}(t_r) - Q^P(t_r) = \begin{cases} > Q^P_{Th} & \text{Implement new weights} \\ \leq Q^P_{Th} & \text{Retain existing weights} \end{cases} \tag{5.11}$$

5.3.2.2 p-CTA Distribution During Addition or Removal of Assets

The addition or removal of assets offers another distinctive scenario for p-CTA realignment. As these processes are dual of each other, we discuss p-CTA re-alignment during asset addition in Algorithm 9. Assuming that new assets are created sequentially and considering that previous distribution of p-CTA weightage are available with the buyer, the algorithm first calculates the normalized CTA

demand ($CTA_{m_j}^{Norm}$) of the existing assets.

Algorithm 9: Distribution of p-CTA weightages while adding a new asset

Input: Optimal weightage vector ($w_{m_j}^*(t_{r-1})$), Asset parameter weightages (ψ_k), Number of adjusted assets (A_m), p-CTA release capacity per asset (Δ_m), Total p-CTA demand of each asset ($CTA_{m_j}^{Tot}(t_{r-1})$);

1 **for** *each superframe* t_r **do**
2 **for** *each asset* m_j **do**
3 Calculate the values of normalized CTA demand $CTA_{m_j}^{Norm}(t_{r-1})$ and the ratio $\zeta_{m_j}(t_{r-1})$ using:
4 $$\begin{cases} CTA_{m_j}^{Norm}(t_{r-1}) = \frac{CTA_{m_j}^{Tot}(t_{r-1})}{\sum_{m_j} CTA_{m_j}^{Tot}(t_{r-1})} \\ \zeta_{m_j}(t_{r-1}) = \left(\frac{CTA_{m_j}^{Norm}(t_{r-1})}{w_{m_j}^*(t_{r-1})}\right) \end{cases}$$
5 Rank assets m_j' in ascending order s.t $\zeta_{m_j}(t_{r-1}) < 1$
6 **for** *each asset* $m_j' \in$ *initial* A_m *assets of the list* **do**
7 Update weightage $w_{m_j'}^*(t_r) = w_{m_j'}^*(t_{r-1}) - \Delta_m$
8 Weightage for the new asset $w_{m_{j+1}}^*(t_{r+1}) = A_m\Delta_m$

Thereafter, the ratio ζ_{m_j} of normalized p-CTA demand $CTA_{m_j}^{Norm}$ and optimal p-CTA weightages ${w^*}_{m_j}$ is calculated for each of the assets. As, both ${w^*}_{m_j}$ and $CTA_{m_j}^{Norm} \in (0,1)$, the assets in which $\zeta_{m_j} < 1$ will add volatility to the portfolio on increasing their weightages. Hence, by ranking ζ_{m_j} values in an ascending order and taking a fraction of p-CTA weightage Δ_m from the first A_m assets in the list, we fork out some channel time from the most volatile assets to accommodate p-CTA for the new asset. Thus, on increasing A_m the volatility of the portfolio degrades gracefully.

Table 5.2: Weightages of qualitative asset parameters from TABLE-5.1

ψ_1	ψ_2	ψ_3	ψ_4	ψ_5	ψ_6
0.4	0.05	0.4	0.05	0.05	0.05

Comparison between Feedback-driven and PACTA approaches: On comparing the two approaches, it can be inferred that the feedback-driven approach needs to calibrate its resource allocation strategy with the slightest change in network conditions. However, under the PACTA approach, the frequency of weightage reallocations can be regulated using the parameter Q_{Th}^P. Since each instance of weightage reallocation results in a significant overhead of control signaling, this poses a major drawback for the feedback-driven approach. In terms of their computational complexities, the performance of the PACTA approach hinges on the Markowitz model where the parameter Σ (i.e., the

covariance of matrix $\Re$) plays a major role. Since the size of the matrix Σ increases as the square of the number of assets in the portfolio, SOPs with a large number of dependent piconets can perform sluggishly. Thankfully, standard indoor SOP structures do not operate with a large number of dependent PNCs, so the possibility of this overhead can be neglected. On the other hand, the complexity of the feedback-driven approach increases linearly with the addition of dependent PNCs in the SOP structure and hence can be scaled with relative ease.

5.4 Performance Evaluation and Results

To evaluate the performance of both the approaches, we implement a MATLAB based mmWave indoor SOP environment. The setup consists of a 2-D space (resembling an indoor scenario), in which a number of users (member nodes) and random sized rectangular obstacles are interspersed with each other. Some of the users are mobile (having random-walk mobility model) whereas the rest are static. The nodes communicate with each other using narrow-beams (links) which can be in any of the channel states [14]. In each instant, the member nodes generate either a CT^{Iso} or a CT^{Asy} type demand which are combined to create the total p-CTA demand. For the PACTA approach, the set of qualitative asset-parameters in TABLE- 5.1 are accounted by using the heuristically assigned weightages as shown in TABLE-5.2.

5.4.1 Evaluation of the Feedback Driven Approach

To evaluate the performance of the proposed schemes, we look into the proportionality between channel-time requirement and channel-time allocation at each of the child piconets for three different configurations of system load. In the first configuration, the total applied p-CTA demand is set to be equal to the total duration of the CTA slot whereas in the second and the third configurations, the demanded p-CTA duration is set to be 1.5 and 2 times respectively of the total duration of the CTA slot. Subsequently, using these three load configurations, we gauge the fairness of channel-time allocation among child piconets. To evaluate and compare the degree of fairness, we calculate the Jain's Fairness Index (JFI) scores over the distribution of p-CTA allocations among child piconets.

Proportionality between channel time requirement and channel time allocation: Assuming that all piconets have equal priority for channel-time allocation, a child piconet with higher CTA requirement should get a relatively larger share of channel time. In this regard, Fig. 5.3(a) depicts the ratio of p-CTA assigned to child piconets and their overall channel time requirements at

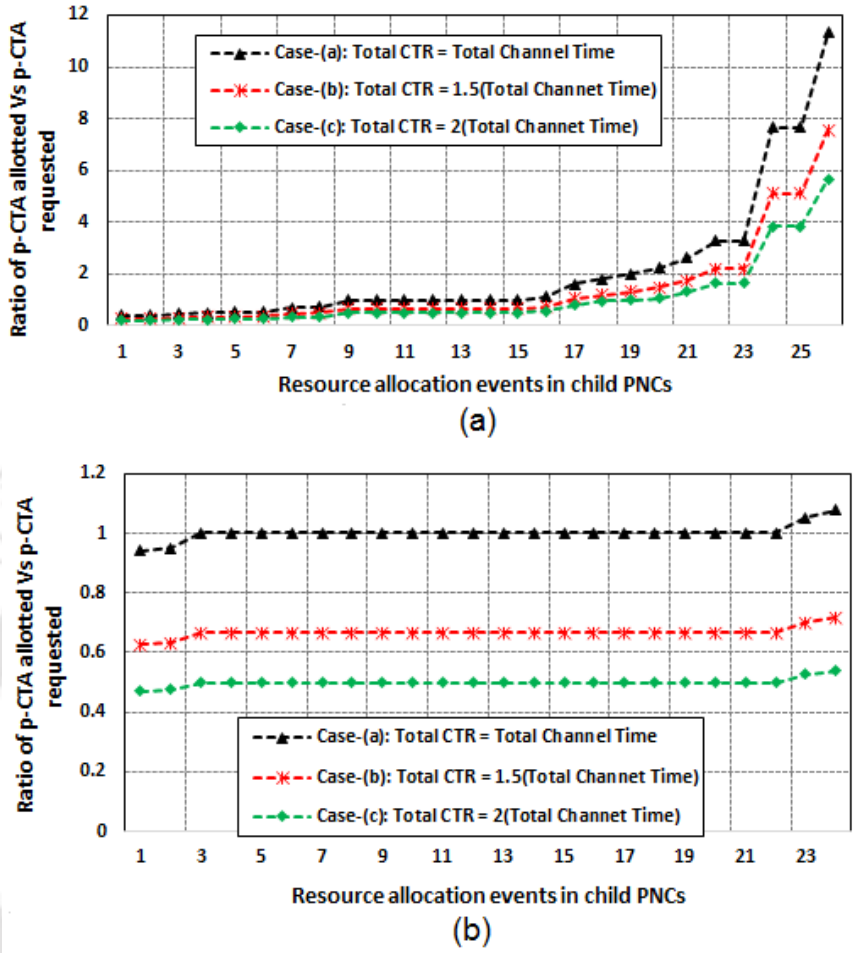

Figure 5.3: Ratio of p-CTA approved and p-CTA requested for different load configurations and resource allocation events (a) scenarios involving addition or removal of PNCs from an SOP; (b) scenarios involving adjustment of p-CTA

the time of initialization of an updated SOP structure. In all the three load configurations (Case-(a), (b) and (c)), the feedback driven approach uses Algorithm 6 to uniformly divide the available channel time between the newly formed piconets. However, as the prospective distribution of channel-time requirements in the updated SOP structure is not known in advance, there is often a discrepancy between the assigned and the required CTAs. Similarly, for the higher load configuration scenarios (Case-(b) and (c)), a comparable trend but with a proportionate reduction in the magnitude of these ratios can be observed.

In case of re-arrangement of p-CTA between PNCs in an existing SOP structure, the feedback driven approach uses Algorithm 7 to proportionately allocate channel-time based on the values of average CTA requirements at the PNCs. Hence, in Fig. 5.3(b) Case-(a), it can be seen that the ratios

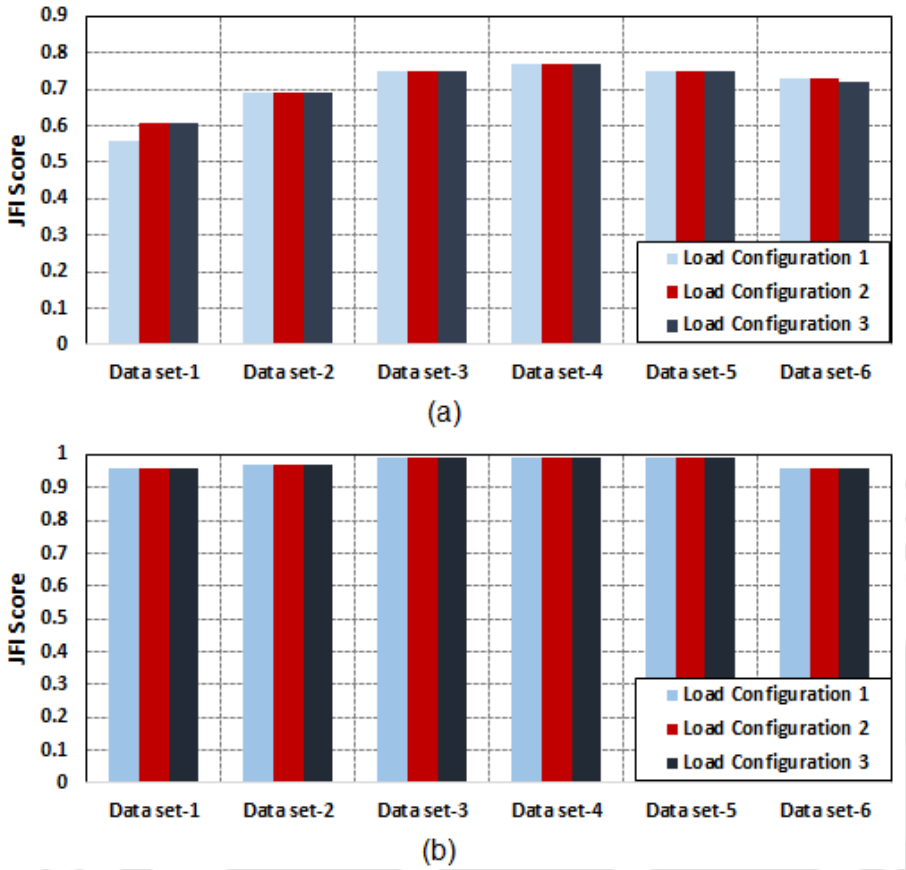

Figure 5.4: JFI scores for p-CTA distribution over different load configurations (a) scenarios involving addition or removal of PNCs from an SOP; (b) scenarios involving adjustment of p-CTA

of the assigned and the requested p-CTAs are close to one. This indicates that the values of average channel time demanded and the share of total channel time allocated to the piconets are almost the same. Moreover, as these ratios are distributed over a small range of values (around unity), it indicates a parity of resource allocation. The same trend can also be seen in case of higher load configurations (Case-(b) and (c)) where the magnitudes of these ratios degrade linearly with an increase in p-CTA demand.

Fairness of p-CTA distribution among child piconets: To compare the fairness of p-CTA distribution among the child PNCs, it is assumed that each DEV in the network has a fixed amount of channel-time requirement. Thus, based on the node associations within the PNCs, the total p-CTA demand at each of the piconets are calculated along with their corresponding Jain's Fairness Index

(JFI) scores as shown in (5.12)

$$JFI\,(x_1, .., x_m) = \frac{\left(\sum_{i=1}^{M} X_{i,m}\right)^2}{M.\sum_{i=1}^{M} X_{i,m}^2} \tag{5.12}$$

In (5.12), the parameter $X_{i,m}$ denotes the ratio of the cumulative p-CTA assigned and demanded at each child piconet. As shown in Fig. 5.4(a) and (b), the values of these JFI scores are plotted with respect to the two distinctive scenarios for resource allocation viz. restructuring of an SOP hierarchy and adjustment of p-CTA in a given SOP. In each of these scenarios, the results are further classified with respect to the three load configurations (i.e., Case-(a), (b) and (c) of Fig. 5.3). On comparing the results in Fig. 5.4(a) and (b), it can be seen that the fairness of p-CTA allocation is higher in case of the p-CTA restructuring scenario (Fig. 5.4(b)) than in case of the SOP restructuring scenario (Fig. 5.4(a)). However, under both the scenarios, these scores are unaffected by changes in the load-profile.

5.4.2 Evaluation of the PACTA Approach

To evaluate the effectiveness of the PACTA approach, we compute its performance in relation to the Feedback driven approach (default) and compare the two approaches in terms of different asset return parameters e.g., the mean and standard deviation of asset returns. As the PACTA approach also focusses on the reduction of return volatility, we evaluate the performance of Algorithm 8 in accommodating new assets (restructuring SOP hierarchy) with minimal return volatility. Apart from these, we also investigate the influence of some other factors e.g., the parameter Q_{Th}^{P} on the number of weightage re-allocation instances and the correlation between the share of CTA components CT^{Iso} and CT^{Asy} on the extent of unused CTA in an asset.

Evaluation of Asset Returns: The results in Fig. 5.5(a) and (b) show the temporal variation in asset returns for different piconets in the SOP portfolio while using the default (feedback) and the PACTA schemes. Here, the magnitude of asset scores and their returns are calculated by using (5.8) over the Markowitz's model. It can be seen that the volatility of asset returns is visibly less under the PACTA approach than under the default (feedback approach) approach. Also, the number of instances with negative returns and their corresponding magnitudes are much lesser in the PACTA approach than under default approach. Since, negative asset returns are caused due to mis-allocation of p-CTA resources, it can be inferred that the default approach performs poorly due to the lack of

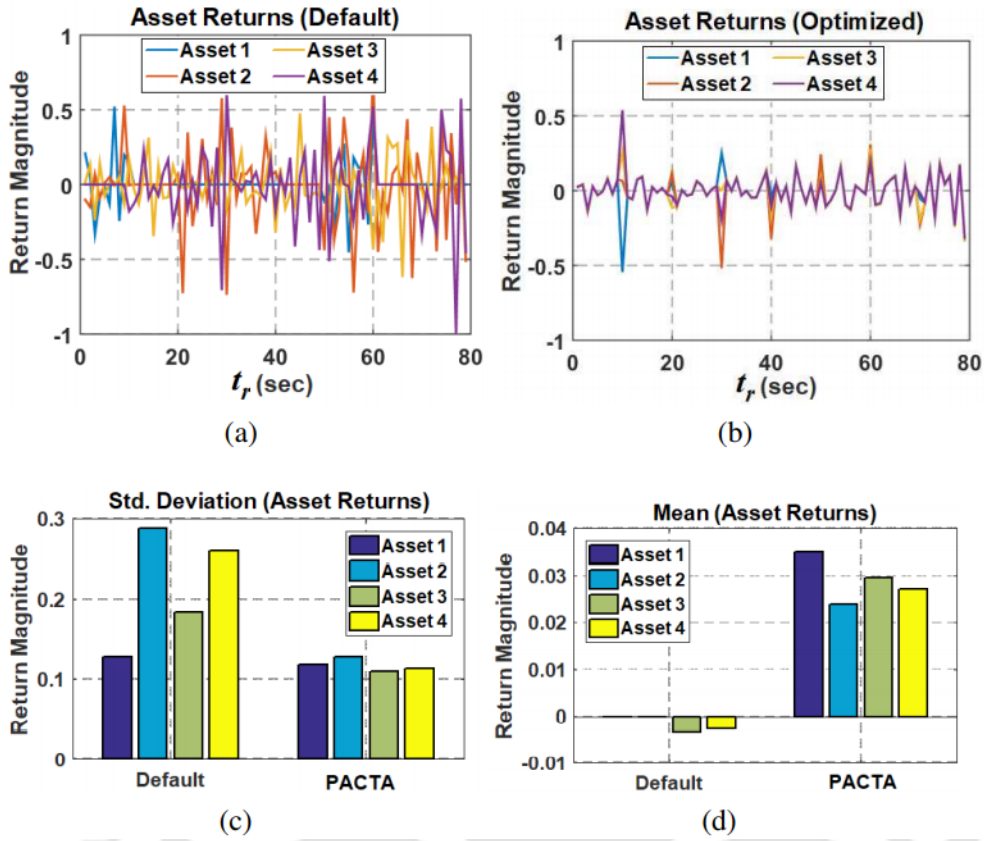

Figure 5.5: Comparison of the p-CTA allocation metrics: (a), (b) Temporal variation of asset returns under default and PACTA approach; (c) Comparison of standard deviation in asset returns; (d) Comparison of mean of asset returns

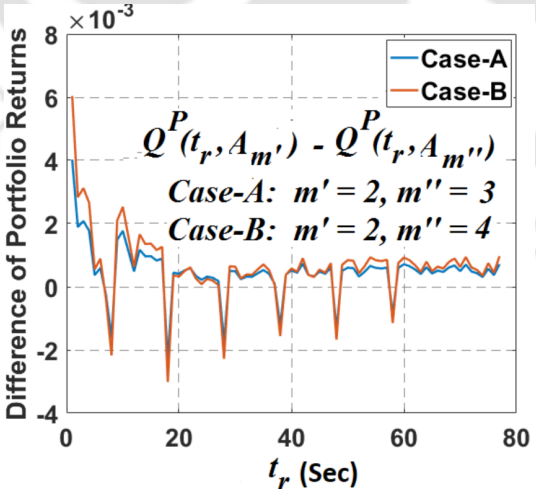

Figure 5.6: Difference between portfolio returns for different values of A_m

an effective p-CTA allocation mechanism. To validate our inferences, we plot the standard-deviation of asset returns along with their mean in Fig. 5.5(c) and (d). It can be observed that the all assets

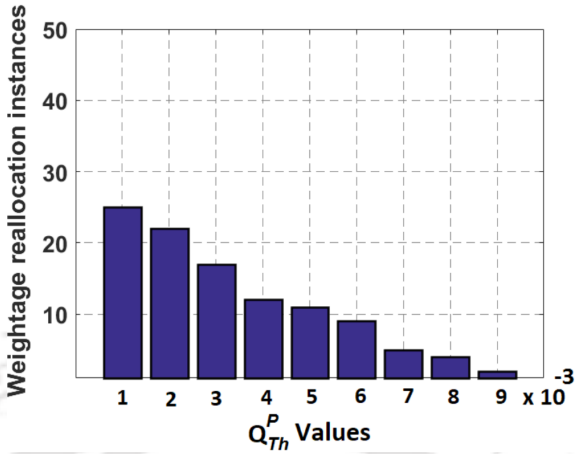

Figure 5.7: Variation in the number of weightage re-allocation instances for different values of Q^P_{Th}

give significantly higher returns and low return volatility while operating under the PACTA scheme.

Influence of A_m in Restructuring of SOP Hierarchy with Low Return Volatility: To evaluate the effectiveness of Algorithm 8 in accommodating new assets, we plot the difference between portfolio returns $Q^P(t_r, A_m)$ for different values of adjusted assets A_m in Fig. 5.6. It can be observed that with an increase in the number of affected assets $A_{m''}$ (in Case-B), the portfolio returns get diminished. This result is seen when we plot the time-series of difference between portfolio returns with respect to a reference scenario of $A_m = 2$ in Case-A and B respectively.

Influence of Q^P_{Th} in Regulation of Weightage Reallocation Instances: To illustrate the effect of Q^P_{Th} in influencing the weightage re-allocations, we plot the number of weightage reallocation instances as a function of Q^P_{Th} in Fig. 5.7. It can be observed that the number of weightage reallocations instances are inversely proportional to the magnitude of Q^P_{Th}. In addition, by increasing the value of Q^P_{Th} threshold, the weightage reallocation instances tend to decrease almost linearly.

Correlation between CTA Components and the Extent of Unused Channel-Time in Assets: Here we evaluate the correlation between the magnitude of channel time parameters $CT^{Asy}_{m_i}$ and $CT^{Iso}_{m_i}$ with respect to that of the unused CTA allocations ($CT^{Unused}_{m_i}$) in each of the child-piconets. The values of $CT^{Unused}_{m_i}$ for any asset m_i is evaluated using:

$$CT^{\text{Unused}}_{m_i}(t_r) = \text{p} - \text{CTA}_{m_i}(t_r) - \left(CT^{Asy}_{m_i}(t_r) + CT^{Iso}_{m_i}(t_r)\right) \tag{5.13}$$

From Fig. 5.8, it can be observed that the $CT^{Iso}_{m_i}$ component of the assets are positively correlated with respect to $CT^{Unused}_{m_i}$. Therefore, assets with higher $CT^{Iso}_{m_i}$ component are also likely to have a

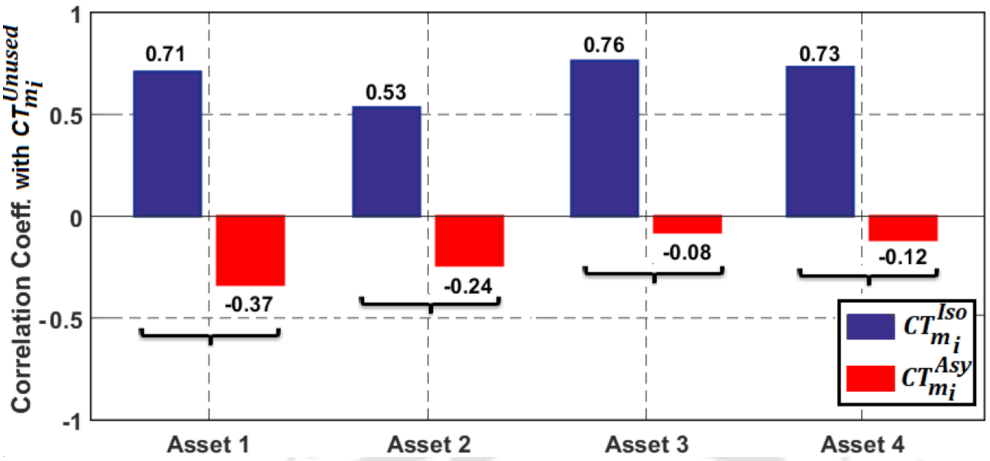

Figure 5.8: Correlation between parameters $CT_{m_i}^{Asy}$ $CT_{m_i}^{Iso}$ and $CT_{m_i}^{Unused}$ of an asset m_i in an SOP hierarchy.

higher share of $CT_{m_i}^{Unused}$. On the contrary, due to negative correlation between $CT_{m_i}^{Asy}$ and $CT_{m_i}^{Unused}$, assets with high $CT_{m_i}^{Asy}$ component can have lower share of $CT_{m_i}^{Unused}$. Therefore, as $CT_{m_i}^{Unused}$ is related to inefficient p-CTA allocation and higher volatility, we infer that the assets with higher $CT_{m_i}^{Iso}$ values will aggravate the volatility scenario of the portfolio.

5.5 Conclusions

In this Chapter, we have discussed the feedback driven and the PACTA approaches for resource allocation (p-CTA distribution) in mmWave SOP structures. Since mmWave SOPs suffer from resource misallocation issues due to beam blockage, it becomes essential to adopt efficient resource allocation mechanisms especially while operating under indoor conditions. Based on the results obtained from the feedback driven approach, it can be inferred that the parent PNC can effectively improve the overall performance of the network by avoiding disproportionate CTA allocations. In addition, the proposed schemes can also be used to achieve fair allocation of channel-time among the child PNCs.

With regard to the PACTA approach, the obtained results have shown that the proposed p-CTA allocation approach can consistently reduce the volatility of multiple QoS parameters in a portfolio and improve the portfolio returns. Thus, achieving an efficient mechanism for channel-time distribution and allowing better utilization of the network resources. Additionally, the system parameters like Q_{Th}^{P} and A_m can be used to regulate the frequency of weightage reallocation instances and to allow restructuring of SOP hierarchy with minimal impact on return volatility. Thus, addressing some of the shortcomings in the feedback driven approach.

6

Conclusion and Future Work

Contents

The work carried out in this thesis aims to investigate and develop various solutions to mitigate beam-blockage in mmWave access networks and to address and resolve, to the extent possible, the various issues which lead to their inefficient and unreliable operation. In this chapter, a summary of the thesis' contributions is presented along with a discussion on some of the possible directions in which this work can be further extended. The main contributions of the thesis are summarised in Section 6.1 and possible future work are outlined in Section 6.2.

6.1 Summary of Contributions

In Chapter 3, we propose different types of blockage-mitigation approaches based on the MAC-layer technique of dynamic control delegation (DCD). The technique enables the PNC node of a mmWave WPAN to dynamically relinquish its controls to other PNC capable member nodes and regulate the piconet operations from different vantage points. Since, control delegation can be implemented within a few milliseconds duration, we use this technique to dynamically reposition the PNC (based on the blockage scenario of the piconet) to provide maximum visibility over the WPAN and improve its blockage scenario. By following this approach, we first propose and discuss two static-rule based DCD approaches (viz. the maximally connected and the maximally stable neighbour approach) and evaluate their performances. However, as the network conditions vary dynamically with time and over the deployment conditions, the static-rule based approaches would ultimately render sub-optimal performance. Hence, we have proposed a DT-MDP based dynamic decision model for taking optimal control delegation decisions. It models the changes in PNC load caused due to an evolving beam-blockage scenario and uses a multi-objective optimization model to derive the ideal delegation policy. Using simulation studies over a variety of indoor scenarios we have demonstrated that the proposed solution can significantly reduce beam blockage in a piconet while still fulfilling a variety of other performance objectives.

In addition, as these approaches do not require any changes in the network architecture or any dedicated network entities to achieve blockage tolerance, they can be readily deployed in various blockage prone scenarios with minimal cost overheads. Also, as the underlying technique of DCD is supported by all the major IEEE MAC-layer standards (e.g., IEEE 802.15.3c [72] and IEEE 802.11ad [74]), these solutions can be implemented over a wide range of devices.

In Chapter 4, we propose various DC- DLLR approaches that can be used in conjunction with

different blockage-mitigation solutions (operating on MLC-architecture) to efficiently maintain connection reliability. Since, the MLC-architecture based blockage-mitigation solutions use a fixed amount of redundant infrastructure (e.g., in terms of the standby network or backup links) to achieve blockage tolerance, they cannot adapt with respect to changing blockage conditions. Hence, most of the time, a large part of the network capacity and other vital network resources remain unused and hence wasted. Thus, incorporating the ability to adjust redundancy levels (using DLLR) can make these solutions operate more efficiently. Additionally, as these device-centric approaches are easier to implement and modify (through device-level driver updates), they are cost-effective and hence more preferrable. To validate the effectiveness of our proposed approaches, we have implemented a form of MLC architecture using the IEEE 802.15.3c based SOP configuration and used this setup to conduct extensive simulation trials over a variety of indoor blockage-prone scenarios. Based on the obtained results, it has been shown that the proposed DC-DLLR approaches can significantly minimise the usage of redundant network resources and hardware in MLC-architecture based blockage-mitigation solutions and can enable them to operate using much lesser CAPEX and OPEX.

In Chapter 5, we proposed the feedback-driven and PACTA approaches to determine the allocation of p-CTA resources in (IEEE 802.15.3c based) mmWave SOP hierarchies. Since beam-blockage causes anomalous utilization of channel-time in the serviced member nodes, it also impacts the utilization of p-CTA in the child PNCs. As a result, different child PNCs within the SOP receive a disproportionate share of network resources. It leads to unreliable operation, inefficient utilization of the network's capacity, and fairness issues. To deal with these problems, the feedback-driven approach allows the default PNC to obtain channel-time utilization data from the child PNCs and use this information to distribute the p-CTA slots based on their relative weights. However, it fails to consider the influence of several other factors which may influence p-CTA allocation (e.g., the share of asynchronous and isochronous CTA demand at each PNC, the mean rate of increase/decrease in node visibility with respect to a PNC, etc.). In addition, under dynamic network conditions, the approach also requires frequent p-CTA reallocations. Therefore, under the PACTA approach, a portfolio theoretic model is used to dynamically determine the ideal p-CTA allocation. The model ensures that the risk of return fluctuations over the allocated resources is minimized while maintaining an acceptable level of return. Thus, an efficient mechanism for channel-time distribution is achieved that allows better utilization of the network resources.

6.2 Further Scope of Work

In this thesis we have addressed some of the issues related to the development of next generation broadband wireless networks. We focus on the mmWave access networks and discuss different MAC-layer based solutions and network architectures to make them blockage tolerant, efficient and more reliable. The work reported in this thesis can be extended in the following directions:

In Chapter 3, the DT-MDP model for DCD approach requires the default PNC to identify one ideal delegable node to relinquish its controls. However, the same approach can also be used to identify a set of child PNCs in an SOP structure. This would enable the default PNC to dynamically determine an SOP hierarchy and operate more effectively.

In Chapter 4, the discussed DC-DLLR approaches have demonstrated a significant improvement in utilization of network resources in comparison to that of the default (static-redundancy) approach. However, new approaches for device-centric DLLR can be explored to achieve even better results. In addition, the possibility of implementing network-centric DLLR approaches can also be explored to achieve a given grade of connection reliability while using minimal redundant infrastructure. Further, in conjunction with the DCD approaches proposed in Chapter 3, the possibility of developing a comprehensive framework where DCD-based approaches operate on top of the MLC architecture can also be explored.

Finally, with respect to Chapter 5, the discussed PACTA approach uses Markowitz's portfolio allocation model to derive the optimal distribution of p-CTA weightages. However, the ability of this model to correctly determine the optimal weightage-vector is largely dependent on sufficiency of data samples (in the training cycle) and their correctness. Therefore, more improved models for resource allocation can be used to achieve better results.

A

Appendix

A.1 IEEE 802.15.3c Based p-CTA Distribution Methodology in SOP Architecture

The IEEE 802.15.3c MAC standard for mmWave systems supports both the parent-child (p/c) and the parent-neighbour (p/n) form of SOP hierarchies. In the case of (p/c) hierarchy (Fig. A.1(a)), a child PNC complements the operations of the parent PNC by providing coverage to a subset of the member nodes and together they serve a common set of DEVs.

In the (p/n) hierarchy (Fig. A.1(b)), the parent piconet and its neighbour serve two different sets of DEVs, but the neighbour PNC depends on the parent PNC to connect with the packet gateway. However, in both these structures, a common approach is followed by the parent PNC for distributing its channel-time resources.

As the IEEE 802.15.3c standard supports multiple levels of SOP hierarchy, the extent of channel-time rearrangement due to the addition/removal of a dependent piconet depends on the level in which the SOP structure has been changed. Thus, in consideration with Fig. A.2(a), Cases-(b) and (c) represent the two different scenarios for the addition of a new piconet (C3) in different levels of the SOP hierarchy. In the Case-(b), the piconet C3 is a child piconet of the parent piconet (P). Therefore, it gets a share of p-CTA from the main SF. However, in the Case-(c), the piconet C3 is a child piconet of another child piconet C1, so the amount of p-CTA that can be allocated to C3 is dependent on

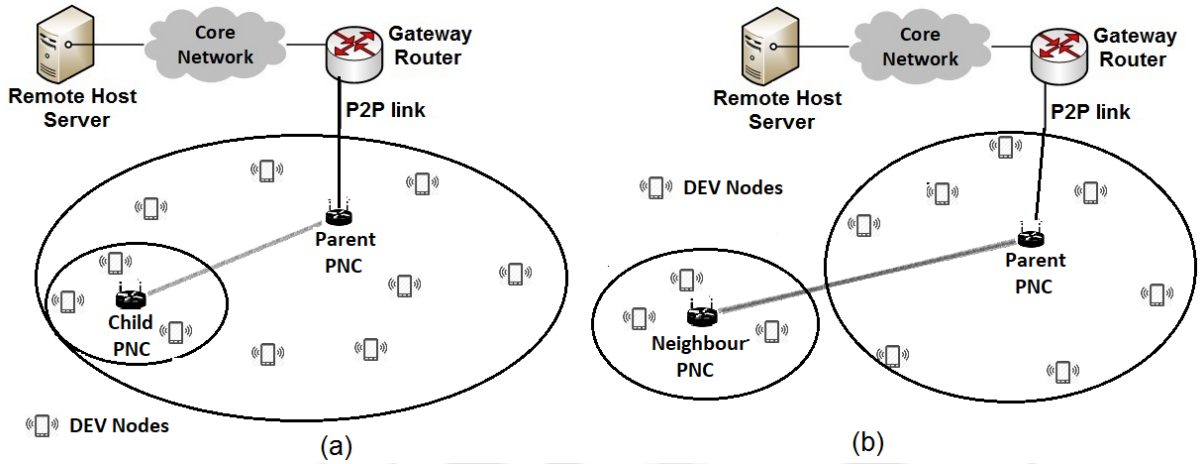

Figure A.1: Types of SOP hierarchies supported by IEEE 802.15.3c MAC standard (a) parent-child (p/c) hierarchy; (b) parent-neighbour (p/n) hierarchy;

the p-CTA allocation at C1. Each of the child piconets perform their MAC layer operations in their designated p-CTA slot as shown in Fig. A.2(b), where all the tasks in an SF are replicated. Each of the slots are also TDMA separated to avoid interference from other piconets.

A.2 Markowitz's Portfolio Allocation Model

In a portfolio of M assets, the time-series of the individual asset-values (v_i) is denoted using $\{v_1(t), .., v_i(t), .., v_M(t)\}$. Since each of these values varies randomly with (t), they are modelled as a discrete-time random process. The *rate-of-return* for each of these processes is defined using a parameter $(r_{v_i}(t))$ where:

$$r_{v_i}(t) = \frac{v_i(t) - v_i(t-1)}{v_i(t-1)} \tag{A.1}$$

Representing the set of all $r_{v_i}(t)$ values using $\Re = (r_{m_1}, .., r_{m_M})^T$, its statistical attributes can be represented using parameters μ, Θ and Σ where $\mu_{v_i} = \mathrm{E}[r_{v_i}]$ denotes the mean rate of return of each asset, $\Theta = (\mu_{v_1}, .., \mu_{v_M})^T$ a random vector corresponding to the set of all μ_{v_i} and $\Sigma = \mathrm{cov}(\Re)$, the covariance matrix of $\Re$.

For a given value of t, if a vector $w \in \mathbb{R}^M$ assigns a set of weights $(w_{v_1}, .., w_{v_M})^T$ to the elements in set $\Re$, then the corresponding rate-of-return over the portfolio is denoted using:

$$r_P = \sum_{i=1}^{M} r_{v_i}.w_{v_i} \tag{A.2}$$

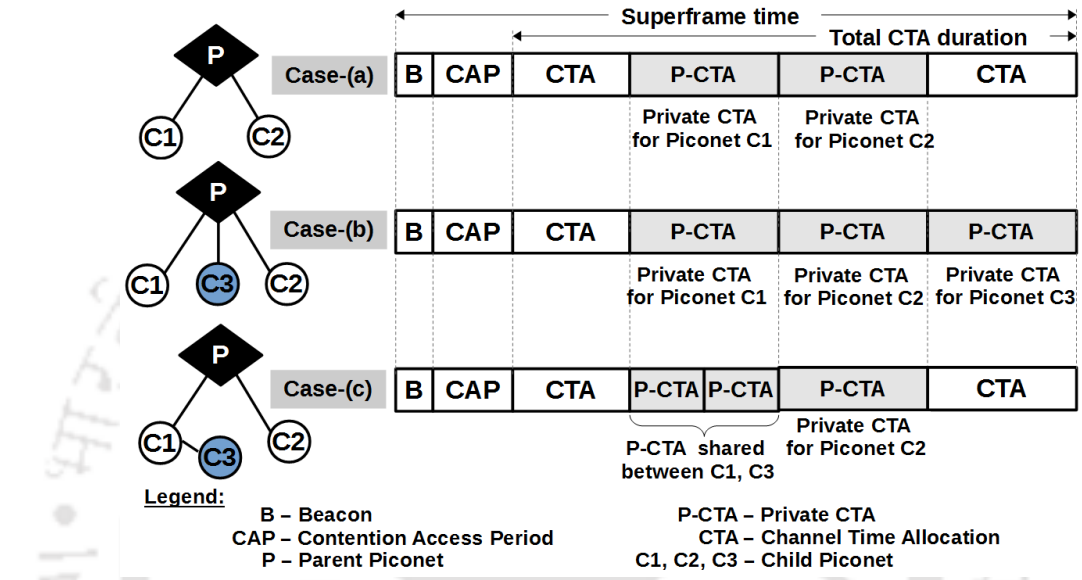

(a)

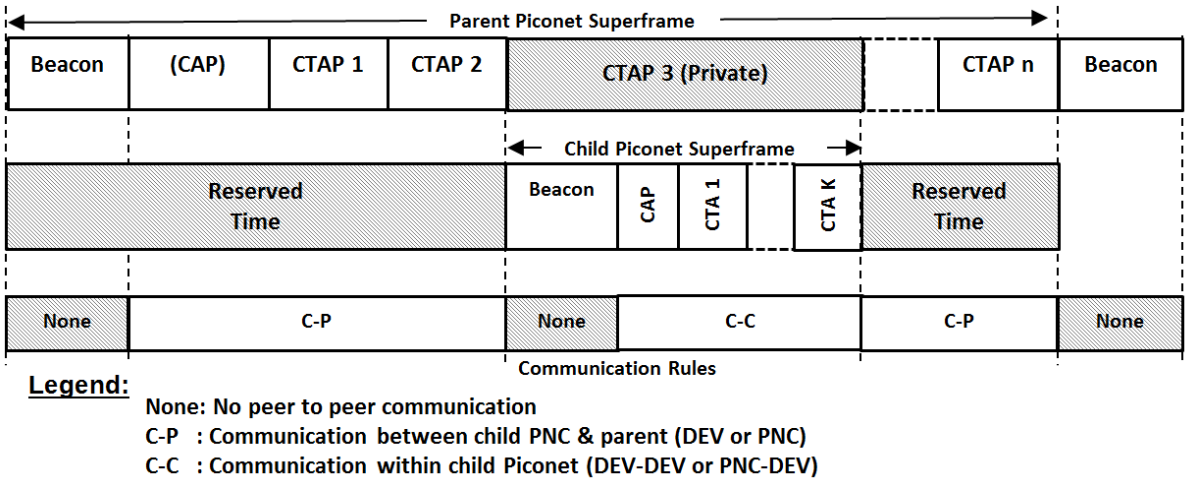

(b)

Figure A.2: Distribution of channel-time between child piconets: (a) p-CTA provisioning for different (p/c) SOP structures; (b) breakup of various SF operations in SOP;

With regard to (A.2), the values of mean rate-of-return over r_P and its variance are represented using the expressions $(\Theta^T w)$ and $\left(w^T \Sigma w\right)$ respectively, and the values of optimal weights w^* corresponding to the ideal portfolio allocation is given by:

$$\underset{w}{\text{minimise}} \quad \left\{\tfrac{1}{2}.\left(w^T \Sigma w\right)\right\} \tag{A.3a}$$

$$\text{subjectto} : \begin{cases} \Theta^{\mathrm{T}} \mathrm{w} \geq \mu_{\mathrm{b}} \\ w^{\mathrm{T}} \mathbb{1} = 1 \end{cases} \tag{A.3b}$$

In (A.3(b)), μ_b denotes the baseline for an asset's expected rate-of-return and $\mathbb{1}$, a vector of all ones. By using this model, the resource allocator considers the variance of portfolio return $\left(w^T \Sigma w\right)$ as a measure of return volatility and tries to minimize it while trying to achieve an acceptable value (μ_b) corresponding to the mean of portfolio return i.e., $(\Theta^T w)$.

Bibliography

[1] White Paper: "Cisco Annual Internet Report (2018–2023)" [Online]. URL: https://www.cisco.com/c/en/us/solutions/collateral/executive-perspectives/annual-internet-report/white-paper-c11-741490.html

[2] Qualcomm Whitepaper: "Making 5G NR a reality" [Online]. URL: https://www.qualcomm.com/media/documents/files/whitepaper-making-5g-nr-a-reality.pdf

[3] F. Boccardi, R. W. Heath, A. Lozano, T. L. Marzetta and P. Popovski, "Five disruptive technology directions for 5G," *IEEE Communications Magazine*, vol. 52, no. 2, pp. 74 – 80, Feb. 2014

[4] Y. Niu, Y. Li, D. Jin, L. Su and A. V. Vasilakos, "A Survey of Millimeter Wave (mmWave) Communications for 5G: Opportunities and Challenges," *Springer Wireless Networks Journal*, vol. 21, no. 8, pp. 2657-2676, Apr. 2015

[5] Z. Bojkovic, B. Bakmaz and M. Bakmaz, "Recent Trends in Emerging Technologies toward 5G Networks," in proc. Of *Advances in Circuits and Systems, Signal Processing and Telecommunications (CSST)*, pp. 137–143, Dubai, 2015

[6] Y. Zhuang, J. Cappos, T. S. Rappaport and R. McGeer, "Future Internet bandwidth trends: An investigation on current and future disruptive technologies," Polytechnic Institute of NYU, Technical Report: TR-CSE-2013-04-1

[7] L.B. Le, V. Lau, E. Jorswieck et al., "Enabling 5G mobile wireless technologies," *Journal on Wireless Com Network,* no. 218 (2015), Sep. 2015

[8] V. Muthukumar, A. Daruna, V. Kamble, K. Harrison and A. Sahai, "Whitespaces after the USA's TV incentive auction: A spectrum reallocation case study," in proc. Of *IEEE International Conference on Communications (ICC)*, London, 2015

[9] Q. C. Li, H. Niu, A. T. Papathanassiou and G. Wu, "5G Network Capacity: Key Elements and Technologies," *IEEE Vehicular Technology Magazine,* vol. 9, no. 1, pp. 71-78, Mar. 2014

[10] L. Zhang, M. Xiao, G. Wu, M. Alam, Y. Liang and S. Li, "A Survey of Advanced Techniques for Spectrum Sharing in 5G Networks," in *IEEE Wireless Communications,* vol. 24, no. 5, pp. 44-51, Oct. 2017

[11] H. Zhou, W. Xu, Y. Bi, J. Chen, Q. Yu and X. S. Shen, "Toward 5G Spectrum Sharing for Immersive-Experience-Driven Vehicular Communications," *IEEE Wireless Communications,* vol. 24, no. 6, pp. 30-37, Dec. 2017

[12] L. Zhang, Y. Liang and M. Xiao, "Spectrum Sharing for Internet of Things: A Survey," *IEEE Wireless Commun. Mag.,* vol. 26, no. 3, pp. 132-139, Jun. 2019

[13] A. Afuah, Innovation Management: Strategies, Implementation and Profits, Oxford Univ. Press, 2003

[14] M. R. Akdeniz, Y. Liu, M. K. Samimi, S. Sun, S. Rangan, T. S. Rappaport, E. Erkip, "Millimeter Wave Channel Modeling and Cellular Capacity Evaluation," *IEEE Journal on Selected Areas in Communications*, vol. 32, no. 6, pp. 1164–1179, Jun. 2014

[15] Huawei Technologies: "5G: Huawei and Vodafone Achieve 20 Gbps for Single-User Outdoor at E-Band," July 2016. [Online]. URL: http://www.huawei.com/en/news/2016/7/huawei-vodafone-5g-test

[16] T. S. Rappaport, Y. Xing, G. R. MacCartney, A. F. Molisch, E. Mellios and J. Zhang, "Overview of Millimeter Wave Communications for Fifth-Generation (5G) Wireless Networks with a Focus on Propagation Models," *IEEE Transactions on Antennas and Propagation*, vol. 65, no. 12, pp. 6213-6230, Dec. 2017

[17] G. R. MacCartney and T. S. Rappaport, "Study on 3GPP rural macrocell path loss models for millimeter wave wireless communications," in proc. of *The IEEE International Conference on Communications (ICC),* May 2017

[18] G. R. MacCartney and T. S. Rappaport, "Rural Macrocell Path Loss Models for Millimeter Wave Wireless Communications," *IEEE Journal on Selected Areas in Communications,* vol. 35, no. 7, pp. 1663-1677, Jul. 2017

[19] G. R. MacCartney et al., "Millimeter Wave Wireless Communications: New Results for Rural Connectivity," in proc. of *All Things Cellular'16: 5th Workshop on All Things Cellular (in conjunction with ACM MobiCom)*, Oct. 2016

[20] "Technical specification group radio access network; channel model for frequency spectrum above 6 GHz (Release 14)," *3rd Generation Partnership Project (3GPP) TR 38.900 V14.2.0,* Dec. 2016, [online] Available: http://www.3gpp.org/DynaReport/38900.html

[21] G. R. MacCartney, M. K. Samimi and T. S. Rappaport, "Omnidirectional path loss models in New York City at 28 GHz and 73 GHz," in proc. of *The IEEE 25th Annual International Symposium on Personal, Indoor, and Mobile Radio Communication (PIMRC),* pp. 227-231, Sep. 2014

[22] Y. Azar, G. N. Wong, K. Wang, R. Mayzus, J. K. Schulz, H. Zhao, F. Gutierrez, D. Hwang, and T. S. Rappaport, "28 GHz propagation measurements for outdoor cellular communications using steerable beam antennas in New York City," in proc. of *IEEE International Conference in Communication (ICC)*, pp. 1–6, Jun. 2013

[23] M. Samimi, K. Wang, Y. Azar, G. N. Wong, R. Mayzus, H. Zhao, J. K. Schulz, S. Sun, F. Gutierrez and T. S. Rappaport, "28 GHz angle of arrival and angle of departure analysis for outdoor cellular communications using steerable beam antennas in New York City," in proc. of *IEEE Vehicular Technology Conference (VTC)*, pp. 1–6, Jun. 2013

[24] G. R. MacCartney and T. S. Rappaport, "73 GHz millimeter wave propagation measurements for outdoor urban mobile and backhaul communications in New York City," in proc. of *The IEEE International Conf. on Commun.(ICC),*, pp. 4862-4867, Jun. 2014

[25] M. K. Samimi and T. S. Rappaport, "Characterization of the 28 GHz Millimeter-Wave Dense Urban Channel for Future 5G Mobile Cellular," Tech. Rep. 2014-001, NYU WIRELESS: Department of Electrical Engineering and Computer Engineering, NYU Tandon School of Engineering, Brooklyn, New York, June 2014

[26] T. S. Rappaport, S. Sun, R. Mayzus, H. Zhao, Y. Azar, K. Wang, G. N. Wong, J. K. Schulz, M. Samimi and F. Gutierrez, "Millimeter wave mobile communications for 5G cellular: It will work!," *IEEE Access*, vol. 1, pp. 335–349, May 2013

[27] T. S. Rappaport, G. R. MacCartney, M. K. Samimi and S. Sun, "Wideband Millimeter-Wave Propagation Measurements and Channel Models for Future Wireless Communication System Design," *IEEE Transactions on Communications*, vol. 63, no. 9, pp. 3029-3056, May 2015

[28] S. Sun, T. A. Thomas, T. S. Rappaport, H. Nguyen, I. Z. Kovacs and I. Rodriguez, "Path Loss, Shadow Fading, and Line-of-Sight Probability Models for 5G Urban Macro-Cellular Scenarios," in proc. of *IEEE Globecom Workshops (GC Wkshps),* pp. 1-7, Dec. 2015

[29] S. Sun, H. Yan, G. R. MacCartney and T. S. Rappaport, "Millimeter wave small-scale spatial statistics in an urban microcell scenario," in proc. of *The IEEE International Conference on Communications (ICC),* pp. 1-7, May 2017

[30] S. Sun et al., "Propagation Path Loss Models for 5G Urban-Micro and Macro-Cellular Scenarios," in proc. of *The IEEE 83rd Vehicular Technology Conference (VTC Spring),* pp. 1-6, May 2016

[31] M. K. Samimi and T. S. Rappaport, "Ultra-wideband statistical channel model for non-line of sight millimeter-wave urban channels," in proc. of *IEEE Global Communications Conference (GLOBECOM),* pp. 3483-3489, Dec. 2014

[32] Y. Xing, O. Kanhere, S. Ju and T. S. Rappaport, "Indoor Wireless Channel Properties at Millimeter Wave and Sub-Terahertz Frequencies," in proc. of *IEEE Global Communications Conference (GLOBECOM),* pp. 1-6, Dec. 2019

[33] J. Ryan, G. R. MacCartney and T. S. Rappaport, "Indoor office wideband penetration loss measurements at 73 GHz," in proc. of *IEEE International Conference on Communications Workshops (ICC Workshops),* pp. 228-233, May 2017

[34] H. Zhao, R. Mayzus, S. Sun, M. Samimi, J. K. Schulz, Y. Azar, K. Wang, G. N. Wong, F. Gutierrez and T. S. Rappaport, "28 GHz millimeter wave cellular communication measurements for reflection and penetration loss in and around buildings in New York City," in proc. of *IEEE International Conference in Communication (ICC)*, pp. 5163–167, Jun. 2013

[35] K. Haneda et al., "Indoor 5G 3GPP-like channel models for office and shopping mall environments," in proc. of *IEEE International Conference on Communications Workshops (ICC),* pp. 694-699, May 2016

[36] H. Xu, V. Kukshya and G. E. Rappaport, "Spatial and temporal characteristics of 60 GHz indoor channels," *IEEE Journal on Selected Areas in Communications*, vol. 20, no. 3, pp. 620 - 630, Apr. 2002

[37] G. R. MacCartney, S. Deng and T. S. Rappaport, "Indoor Office Plan Environment and Layout-Based mmWave Path Loss Models for 28 GHz and 73 GHz," in proc. of *IEEE 83rd Vehicular Tech. Conf. (VTC Spring),* pp. 1-6, May 2016

[38] G. R. Maccartney, T. S. Rappaport, S. Sun and S. Deng, "Indoor Office Wideband Millimeter-Wave Propagation Measurements and Channel Models at 28 and 73 GHz for Ultra-Dense 5G Wireless Networks," *IEEE Access,* vol. 3, pp. 2388-2424, Oct. 2015

[39] P. A. Tenerelli and C. W. Bostian, "Measurements of 28 GHz diffraction loss by building corners," in proc. of *9th IEEE International Symposium on Personal, Indoor and Mobile Radio Commun. (Cat. No.98TH8361),*, Sep. 1998

[40] N. Tervo et al., "Diffraction measurements around a building corner at 10 GHz," in proc. of *1st International Conference on 5G for Ubiquitous Connectivity (5GU),* pp. 187-191, Nov. 2014

[41] J. Lu, P. Cabrol, D. Steinbach and R. Pragada, "Measurement and characterization of various outdoor 60 GHz diffracted and scattered paths," in proc. of *IEEE Military Communications Conference (MILCOM),* pp. 1238-1243, Nov. 2013

[42] S. Deng, G. R. MacCartney Jr., T. S. Rappaport, "Indoor and Outdoor 5G Diffraction Measurements and Models at 10, 20, and 26 GHz," *IEEE Global Communications Conference (GLOBECOM),* pp. 1-7, Feb. 2016

[43] A. Goldsmith, "Wireless Communications," Cambridge University Press, 2005

[44] M. Jacob et al., "Diffraction in mm and sub-mm wave indoor propagation channels," *IEEE Transactions on Microwave Theory and Techniques,* vol. 60, no. 3, pp. 833-844, Mar. 2012

[45] G. R. MacCartney Jr., S. Deng, S. Sun, T. S. Rappaport, "Millimeter-Wave Human Blockage at 73 GHz with a Simple Double Knife-Edge Diffraction Model and Extension for Directional Antennas," in proc. of *IEEE 84th Vehicular Tech. Conf. Fall (VTC 2016-Fall),* Sept. 2016

[46] S. Collonge, G. Zaharia and G. E. Zein, "Influence of human activity on wide-band characteristics of the 60 GHz indoor radio channel," *IEEE Transaction on Wireless Communication*, vol. 3, no. 6, pp. 2396-2406, Nov. 2004

[47] G. R. MacCartney, Jr., T. S. Rappaport, and Sundeep Rangan, "Rapid Fading Due to Human Blockage in Pedestrian Crowds at 5G Millimeter-Wave Frequencies," in proc. of *IEEE Global Communications Conference (GLOBECOM),* Singapore, Dec. 2017

[48] C. Slezak, V. Semkin, S. Andreev, Y. Koucheryavy and S. Rangan, "Empirical Effects of Dynamic Human-Body Blockage in 60 GHz Communications," in *IEEE Communications Magazine,* vol. 56, no. 12, pp. 60-66, Dec. 2018

[49] K. Sato and T. Manabe, "Estimation of propagation-path visibility for indoor wireless LAN systems under shadowing condition by human bodies," in proc. of *IEEE Vehicular Technology Conference (VTC '98)*, vol. 3, pp. 2109-2113, May 1998

[50] FEDERAL COMMUNICATIONS COMMISSION, "Millimeter Wave Propagation: Spectrum Management Implications," Bulletin Number 70, Jul. 1997

[51] FCC rules for unlicensed wireless equipment operating in the ISM bands. [Online]. URL: https://www.fcc.gov/wireless/bureau-divisions/technologies-systems-and-innovation-division/rules-regulations-title-47

[52] T. S. Rappaport, Y. Qiao, J. I. Tamir, J. N. Murdock and E. Ben-Dor, "Cellular broadband millimeter wave propagation and angle of arrival for adaptive beam steering systems (invited paper)," in proc. of *IEEE Radio and Wireless Symposium,* pp. 151-154, Jan. 2012

[53] T. S. Rappaport, F. Gutierrez, E. Ben-Dor, J. N. Murdock, Y. Qiao and J. I. Tamir, "Broadband Millimeter-Wave Propagation Measurements and Models Using Adaptive-Beam Antennas for Outdoor Urban Cellular Communications," *IEEE Transactions on Antennas and Propagation,* vol. 61, no. 4, pp. 1850-1859, Apr. 2013

[54] Z. Khan, J. J. Lehtomäki, V. Selis, H. Ahmadi and A. Marshall, "Intelligent Autonomous User Discovery and Link Maintenance for mmWave and TeraHertz Devices with Directional Antennas," *IEEE Transactions on Cognitive Commun. and Networking,*, Apr. 2021, (Early Access)

[55] F. A. Sunny, Z. I. Chowdhury and M. S. Kaiser, "Counter propagation ANN based massive adaptive array antenna beamforming for mmWave communication system," in proc. of *IEEE International Conference on Telecommunications and Photonics (ICTP),* pp. 1-5, Dec. 2015

[56] Y. Ghasempour, C. R. C. M. da Silva, C. Cordeiro and E. W. Knightly, "IEEE 802.11ay: Next-Generation 60 GHz Communication for 100 Gb/s Wi-Fi," *IEEE Communications Magazine,* vol. 55, no. 12, pp. 186-192, Dec. 2017

[57] Z. Genc, U. H. Rizvi, E. Onur and I. Niemegeers, "Robust 60 GHz indoor connectivity: Is it possible with reflection?," in proc. of *IEEE* 71^{st} *Vehicular Technology Conference (VTC)*, pp. 1-5, May 2010

[58] L. Zhang, X. Chen, Y. Fang, X. Huang and X. Fang, "Learning-Based mmWave V2I Environment Augmentation through Tunable Reflectors," in proc. of *IEEE Global Communications Conference (GLOBECOM)*, pp. 1-6, Dec. 2019

[59] C. Yiu and S. Singh, "Empirical Capacity of mmWave WLANs," *IEEE Journal on Selected Areas in Communications*, vol. 27, no. 8, Oct. 2009

[60] A. Patra, L. Simic and M. Petrova, "Experimental evaluation of a novel fast beam steering algorithm for link re-establishment in mm-wave indoor WLANs," in proc. of *IEEE Personal Indoor and Mobile Radio Communications Conference (PIMRC)*, pp. 1-7, Sep. 2016

[61] X. An, C. Sum, R. V. Prasad, J. Wang, Z. Lan, J. Wang, R. Hekmat, H. Harada and I. Niemegeers, "Beam switching support to resolve link-blockage problem in 60 GHz WPANs," in proc. of *IEEE* 20^{th} *International Symposium on Personal, Indoor and Mobile Radio Communications (PIMRC)*, pp. 390–394, Sep. 2009

[62] M. Park and H. K. Pan, "A Spatial Diversity Technique for IEEE 802.11ad WLAN in 60 GHz Band," *IEEE Communication Letters*, vol. 16, no. 8, Aug. 2012

[63] Z. Xiao, "Suboptimal Spatial Diversity Scheme for 60 GHz Millimeter-Wave WLAN," *IEEE Communication Letters*, vol. 17, no. 9, Sep. 2013

[64] S. Doğan, M. Karabacak and H. Arslan, "Optimization of Antenna Beamwidth under Blockage Impact in Millimeter-Wave Bands," in proc. of *IEEE 29th Annual International Symposium on Personal, Indoor and Mobile Radio Communications (PIMRC),* pp. 1-5, Sep. 2018

[65] M. Polese, M. Giordani, M. Mezzavilla, S. Rangan and M. Zorzi, "Improved Handover Through Dual Connectivity in 5G mmWave Mobile Networks," *IEEE Journal on Selected Areas in Communications*, vol. 35, no. 9, pp. 2069-2084, Jun. 2017

[66] M. Gerasimenko, D. Moltchanov, M. Gapeyenko, S. Andreev and Y. Koucheryavy, "Capacity of Multi-connectivity mmWave Systems With Dynamic Blockage and Directional Antennas," *IEEE Transactions on Vehicular Technology*, vol. 68, no. 4, pp. 3534-3549, Apr. 2019.

[67] H. Yang, W. Zhong, C. Chen, A. Alphones and P. Du, "QoS-Driven Optimized Design based Integrated Visible Light Communication and Positioning for Indoor IoT Networks," *IEEE Internet of Things Journal*, vol. 7, no. 1, pp. 269-283, Jan. 2020.

[68] M. Mezzavilla, S. Goyal, S. Panwar, S. Rangan and M. Zorzi, "An MDP model for optimal handover decisions in mmWave cellular networks," in proc. of *European Conference on Networks and Communications (EuCNC)*, pp. 100-105, Jun. 2016.

[69] Y. Niu, W. Ding, H. Wu, Y. Li, X. Chen, B. Ai and Z. Zhong, "Relay-Assisted and QoS Aware Scheduling to Overcome Blockage in mmWave Backhaul Networks," *IEEE Transactions on Vehicular Technology*, vol. 68, no. 2, pp. 1733-1744, Jan. 2019.

[70] Y. Niu *et al.*, "Exploiting multi-hop relaying to overcome blockage in directional mmWave small cells," *Journal of Communication and Networks,* vol. 18, no. 3, pp. 364–374, Jun. 2016.

[71] S. Singh, F. Ziliotto, U. Madhow, E. M. Belding and M. J. W. Rodwell, "Millimeter Wave WPAN: Cross-Layer Modeling and MultiHop Architecture," in proc. of *the* 26^{th} *IEEE International Conference on Computer Communications (INFOCOM)*, pp. 2336-2340, May 2007.

[72] "Wireless Medium Access Control (MAC) and Physical Layer (PHY) Specifications for High Rate Wireless Personal Area Networks (Amendment 2:) Millimeterwave-based Alternative Physical Layer Extension," *IEEE Std. 802.15.3c-2009*, Oct. 2009

[73] White Paper: "Introduction to the NI mmWave Transceiver System Hardware," [Online]. URL: https://www.ni.com/en-in/innovations/white-papers/16/introduction-to-the-ni-mmwave-transceiver-system-hardware.html

[74] "Wireless LAN Medium Access Control (MAC) and Physical Layer (PHY) Specifications (Amendment 3:) Enhancements for Very High Throughput in the 60 GHz Band," *IEEE Std. P802.11ad*, Jul. 2011

[75] S. Sindian, A. E. Samhat, A. Khalil, M. Crussire and J. Hlar, "Dynamic Superframe Size based Admission Control in Parent / Child HR WPANs," in proc. of *The* 3^{rd} *International Conference on Communications and Information Technology (ICCIT)*, Aug. 2013

[76] I. Jamil, S. Sindian, A. Khalil, M. Crussire and J. Hlar, "A New Distributed Decision Making Scheme for the IEEE 802.15.3 Parent / Child Model," in proc. of *The* 3^{rd} *International Conference on Communications and Information Technology (ICCIT)*, Beirut, Aug. 2013

[77] P. Xue, P. Gong, and D. Kyung Kim, "Enhanced IEEE 802.15.3 MAC Protocol for Efficient Support of Multiple Simultaneously Operating Piconets," *IEEE Transactions on Vehicular Technology*, vol. 57, no. 4, Jul. 2008

[78] B. Shrestha, K. W. Choi and E. Hossain, "A Dynamic Time Slot Allocation Scheme for Hybrid CSMA/TDMA MAC Protocol," *IEEE Wireless Communications Letters*, vol. 2, no. 5, pp. 535-538, Oct. 2013

[79] Shao-cheng Huang, Lin-hua Ma, Le Ru, Zhao Cai, Song Zhang and Xing Hu, "Traffic prediction-based dynamic time slot allocation TDMA protocol," in proc. of *IEEE International Conference on Computer and Communications (ICCC)*, pp. 275-279, Oct. 2015

[80] Huawei Technologies: "Indoor 5G Scenario Oriented White Paper," Version 3.0, October 2019. [Online]. URL: https://carrier.huawei.com/∼/media/ CNBGV2/download/products/servies/Indoor-5G-Scenario-Oriented-White-Paper-en.pdf

[81] H. Markowitz, "The optimization of a quadratic function subject to linear constraints," *Naval Research Logistics Quarterly*, vol. 3, pp. 111-133, 1956

[82] C. W. Pyo et al., "MAC Enhancement for High Speed Communications in the 802.15.3c mmWave WPAN", *Springer Wireless Personal Communication Journal*, vol. 51, pp. 825-841, Jul. 2009

[83] M. Puterman, "Markov Decision Process: Discrete Stochastic Dynamic Programming", Hoboken NJ, USA: Wiley, 1994

[84] A. Ksentini, T. Taleb and K. B. Letaif, "QoE-Based Flow Admission Control in Small Cell Networks," *IEEE Transactions in Wireless Communication*, vol. 14, no. 4, pp. 2474-2483, Apr. 2016

[85] P. Tseng, "Solving H-horizon, stationary Markov decision problems in time proportional to log(H)", *Operation Research Letters*, vol. 9, no. 5, pp. 287-297, 1990.

[86] NYUSIM mmWave channel model simulation tool. [Online] URL: https://wireless.engineering.nyu.edu/download-nyusim-version-3-0/ (Accessed May 2021)

List of Publications

Journal Publications

1. Arijit Bhattacharjee, Ratnajit Bhattacharjee and Sanjay Kumar Bose, "PACTA: A Portfolio Theory Based Approach for QoS Aware Resource Allocation in mmWave Networks," *IEEE Communication Letters*, vol. 24, no. 8, pp. 1794-1798, Aug. 2020.
   (Chapter 5)

2. Arijit Bhattacharjee, Ratnajit Bhattacharjee and Sanjay Kumar Bose, "An Approach for Mitigation of Beam Blockage in mmWave Based Indoor Networks," *IEEE Internet of Things Journal*, (Early Access), Apr. 2021, (DOI- 10.1109/JIOT.2021.3070309).
   (Chapter 3)

Conference Publications

1. Arijit Bhattacharjee, Ratnajit Bhattacharjee and Sanjay Kumar Bose, "Mitigation of beam blocking in mmWave indoor WPAN using dynamic control delegation based approach," in proceedings of *IEEE International Conference on Advanced Networks and Telecommunications Systems (ANTS)*, pp. 1-6, Nov. 2016.
   (Chapter 3)

2. Arijit Bhattacharjee, Ratnajit Bhattacharjee and Sanjay Kumar Bose, "A dynamic approach for channel time allocation in IEEE 802.15.3 based parent-child piconet model," in proceedings of *IEEE Region 10 Conference (TENCON)*, pp.851-856, Jun. 2017.
   (Chapter 5)

3. Arijit Bhattacharjee, Ratnajit Bhattacharjee and Sanjay Kumar Bose, "DC-DLLR: A MAC Layer Approach for Reliable and Blockage Tolerant mmWave Indoor Networks," in proceedings of *13th International Conference on Communication Systems & Networks Conference (COMSNET)*, pp. 509-515, Jan. 2021.
   (Chapter 4)